Cold molecular ion - neutral collisions in a dynamic ion - atom hybrid trap

Inauguraldissertation

zur
Erlangung der Würde eines Doktors der Philosophie
vorgelegt der
Philosophisch-Naturwissenschaftlichen Fakultät
der Universität Basel
von

Alexander Dietmar Dörfler

aus Österreich

Basel, 2020

Genehmigt von der Philosophisch - Naturwissenschaftlichen Fakultät auf Antrag von

Prof. Dr. Stefan Willitsch und Prof. Dr. Olivier Dulieu (Universitè Paris Sud, LAC)

Basel, den 15.10.2019

Prof. Dr. Martin Spiess

Dekan der Philosophisch - Naturwissenschaftlichen Fakultät

to my children O_2K, P_2K and M_2K,
Thank you for your inspirational curiosity.

Abstract

This thesis explores the fundamental physical and chemical processes between molecular ions and neutral atoms in the gas phase at very low energies. At temperatures in the mK regime, these are dominated by long - range interactions and only a few partial waves. This study contributes to the understanding of the details of intermolecular interactions and provides valuable data for benchmarking theoretical models and quantum - chemical calculations. Although there is a wide range of previous atomic collision system studies, the investigations of cold collisions with molecular ions are limited [1–7]. The experimental setup used in this work enabled the measurement of rate coefficients for molecular ion - neutral collisions [4, 8]. The development of a dynamic ion - neutral hybrid trap with improved control over collision energy [9] led to new insights into charge - transfer rate coefficients for molecular ion - neutral atom collisions involving $N_2^+ + Rb$, $O_2^+ + Rb$ and $N_2H^+ + Rb$. Two different experimental settings enable state - and collision - energy dependent measurements of rate coefficients for all systems revealing an intriguing interplay between long - and short - range effects for the homonuclear diatomics by comparison to theoretical calculations and surprising experimental results for the polyatomic study. A fit of a constant function to the measured CT rate coefficients in the state - dependent experiment of $N_2H^+ + Rb$ yielded the similar result as for $N_2^+ + Rb$ $(5s)$ $(^2S_{1/2})$. In the collision - energy dependent experiment the CT rate coefficient for $N_2H^+ + Rb$ $(5s)$ $(^2S_{1/2})$ and $N_2H^+ + Rb$ $(5p)$ $(^2P_{3/2})$ are both similar to the results for $N_2^+ + Rb$ $(5s)$ $(^2S_{1/2})$, and also the rate coefficients increase as the collision - energy increases.

Acknowledgments

I would like to thank my supervisors, Professor Stefan Willitsch and Professor Olivier Dulieu, for the opportunity to join the Marie Skłodowska Curie Initial training network: **COMIQ** (**CO**ld **M**olecular **I**ons at the **Q**uantum limit) and their guidance and extraordinary mentorship. Professor Francesco Gianturco for his mentorship and guidance in the theoretical computations. Pascal Eberle for his patience with all my ideas for the experiment. The past and present members of the Willitsch group for an extraordinary work environment and a wonderful time outside of the university. Kaveh Najafian as COMIQ and travel buddy as well as the nice evenings at the Rhein and the wonderful music in the lab. Mudit Sinhal for the nice evenings and companionship. Especially, I want to thank the staff of the mechanical and electronics workshops - Grischa Martin, Philipp Knöpfel, Simon Ruefner, Martin Pohl, Dieter Wild and Georg Holderied Salvisberg - for their amazing and precise work and the construction of incredible experimental parts. Dr. Anantoly Johnson for his help and work on the laser - setups and the many visits to the classic concerts. The staff members who keep everything running, Daniela Tischhauser, Maya Greuter and Mariella Schneiter and Markus Ast.
Thank you Ian for proofreading my thesis before the final print.
The amazing time in the COMIQ Network will not be forgotten. Thank you Steffen, Kaveh, Johannes, Lorenzo, Ivan, Ibrokhim, Amir, Leonardo, Ashwin, Johannes, Milán, Ilia, Humberto and Karin. Humberto Da Silva jr. thank you for my time in Paris.
Funding from the European Union FP7-PEOPLE-2013-ITN is acknowledged greatfully, as is funding from the Swiss National Science Foundation, grant nr. 200020_175533, the NCCR MUST and the University of Basel.
Thank you Maria Sophia, my beloved wife, without your selfless support, dedication and patience, it would not have been possible. I owe you a lot. Thank you Oliver Otto, Philipp Peter and Maria Mathilda, my beloved children to whom I dedicate this work. Watching you learning to walk, taught me persistence. Some things are not mastered in a day. Thanks to my mother Gabriela Radatz and my mother in law Doris Kittler for your amazing help raising my children during the last 5 years and all your support. Thanks to my father Peter Dörfler. Thank you Otto Plattner for your encouragement to apply and go to Switzerland. As you said, you have to grasp the opportunity, because fortune favours the brave. Last but not least thanks to all my friends.

List of Figures

2.1 Impact parameter and effective potential 6
2.2 Doppler cooling levels of Ca^+ ions and Rb atoms 11
2.3 Doppler cooling schematic 12
2.4 Schematic of a magneto optical trap 14
2.5 Schematic of an ion trap 18
2.6 Bi-component crystal 19

3.1 Experimental setup 22
3.2 Schematic hybrid trap and technical drawing of the ion trap 23
3.3 $^{40}Ca^+$ laser setup 26
3.4 ^{87}Rb laser setup 27
3.5 Atom cloud temperature 28
3.6 Shuttling Operation Principle of the Shuttling Atom Trap 31
3.7 Laser timing sequence for the pulse generator 32
3.8 Imaging setup for the atoms 34
3.9 Time of flight profile, Experimental and simulated kinetic energies 35
3.10 Ionisation laser setup 36

4.1 Atom cloud simulation process 40
4.2 Solutions of the pendulum problem 44
4.3 Numerical solutions of the Kepler problem 44
4.4 Illustration for the Störmer–Verlet method 45
4.5 Variation of the cooling-laser detuning 48
4.6 Variation of the $1/e^2$ radii of the laser beams 50
4.7 Variation of the cooling-laser intensity 51
4.8 Variation of the magnetic-field gradient 53
4.9 Atom cloud expansion during simulation 54

5.1 Initial PES from MOLPRO calculated by Yurtsever 60
5.2 $N_2^+ + Rb$ / $N_2 + Rb^+$ Potential energy surface and V_λ 62
5.3 $N_2^+ + Rb$ elastic integrated cross sections: singlet to doublet comparison 65

5.4 $N_2^+ + Rb$ inelastic integrated cross sections 66
5.5 $N_2^+ + Rb$ calculation at 0 mK to 70 mK 67

6.1 Molecular orbital energy diagram for N_2 and O_2 72
6.2 Old N_2^+ measurements of Ref. [10] 73
6.3 Asymptotic energies of the entrance and possible product channels for $N_2^+ + Rb$ 76
6.4 CT rate coefficient of $N_2^+ + Rb$ 78
6.5 Electronic states for N_2 and N_2^+ as a function of the bond length r (a.u.) . . . 80
6.6 Angle dependent reaction path of $N_2^+ + Rb$ 80
6.7 Direct and indirect CT trajectories 81
6.8 Detailed dynamics of indirect CT trajectories 83
6.9 Asymptotic energies of the entrance and possible product channels of $O_2^+ + Rb$ 84
6.10 CT rate coefficient of $O_2^+ + Rb$ 86
6.11 Electronic states for O_2 and O_2^+ as a function of R (a.u.) 87
6.12 Rate coefficient of $N_2H^+ + Rb$ 90

A.4.1 Comparison of measurement uncertainty to the N_2^+ measurement 108
A.4.2 Comparison of measurement uncertainty to the O_2^+ measurement 109
A.4.3 Comparison of measurement uncertainty to the N_2H^+ measurement 110
A.5.1 Overlap calculation schematic 111

B.1.1 Polariser internal setup 114
B.1.2 Potentiometers 1 and 2 115
B.1.3 L293B motor - driver, NSA12 stepper - motor 116
B.1.4 In - house rotational mount for $\lambda/2$ wave - plate 116
B.1.5 Pin layout 117
B.1.6 Laser beam setup for the photodiodes 119

List of Tables

5.1 Parameters for the analytic description of the interactions 63

A.1 Uncertainty estimation 108

B.1 Wiring table for Nokia 5110 Display 117
B.2 Wiring table for LEDs, Potentiometer, Buttons, Motor 118

Contents

1 Introduction *1*

1.1 Outline of the thesis . . . 3

2 Theoretical concepts *5*

2.1 Cold ion - neutral collisions and reactions . . . 5
2.1.1 Capture - model and effective potentials . . . 5
2.1.2 Langevin rate coefficients and cross sections . . . 7
2.1.3 Extended interaction potential . . . 7
2.2 Hybrid Trapping . . . 8
2.2.1 A brief history on hybrid traps . . . 8
2.2.2 Interaction of light with matter . . . 9
2.2.3 Atom trapping and cooling . . . 14
2.2.4 Ion trapping and cooling . . . 16

3 Experiment *21*

3.1 Setup . . . 21
3.1.1 Vacuum chamber . . . 24
3.1.2 Facts about the hybrid trap . . . 24
3.1.3 Lasers and optics (ions,atoms) . . . 25
3.2 Stationary atom cloud . . . 27
3.2.1 Temperature measurement . . . 28
3.2.2 Average Density n_{avg} . . . 29
3.3 Shuttling atom cloud . . . 30
3.3.1 Optics, optical elements and pulse sequence generation . . . 30
3.3.2 Velocity determination . . . 33
3.3.3 Inferring the kinetic energy, the velocity, the kinetic energy spread and the velocity spread of the shuttling Rb atoms from simulations . . . 33
3.4 Atomic and molecular ions . . . 35
3.4.1 Loading and trapping of Ca^+ . . . 36

3.4.2 Loading, trapping of molecular ions . . . 37

4 Simulation of shuttling atom clouds *39*

4.1 Description of the approach . . . 39
4.1.1 Equilibration . . . 40
4.1.2 Shuttling . . . 41
4.1.3 Integration algorithm . . . 42
4.2 Influence of different parameters on the atom cloud . . . 45
4.2.1 Introduction . . . 45
4.2.2 Initial conditions . . . 46
4.2.3 Bright - and dark - atom shuttling simulations . . . 47
4.3 Summary and conclusion . . . 52

5 Rotational state - changing collisions and radiative association of $N_2^+ + Rb$ *57*

5.1 The statistical product - state distributions for ultracold reactions in external fields . . . 58
5.2 ASPIN: Methods, Results and Discussion . . . 59
5.2.1 Computational Methods . . . 59
5.2.2 Analysis and results of the ASPIN calculations . . . 64
5.3 Modeling ion losses from radiative association paths . . . 67

6 Charge - transfer (CT) collision experiments with molecular ions *71*

6.1 Previous molecular - ion experiments . . . 71
6.2 Theoretical methods for N_2^+ and O_2^+ . . . 73
6.2.1 Electronic structure calculations . . . 73
6.2.2 Quantum scattering calculations . . . 74
6.2.3 Quasiclassical - dynamics calculations for N_2^+ . . . 74
6.3 The $N_2^+ + Rb$ system . . . 75
6.3.1 Methods . . . 75
6.3.2 Charge - transfer (CT) rate coefficients: Results and discussion . . . 77
6.3.3 Conclusions . . . 82
6.4 The $O_2^+ + Rb$ system . . . 84
6.4.1 Methods . . . 85
6.4.2 Charge - transfer (CT) rate coefficients: Results and discussion . . . 85

6.4.3 Conclusions . . . 88
6.5 The $N_2H^+ + Rb$ system . . . 88
6.5.1 Methods . . . 89
6.5.2 Charge-transfer (CT) rate coefficients: Results and discussion . . . 89
6.5.3 Conclusion . . . 91

7 Conclusion and outlook *93*

A Appendix Programming *97*

A.1 Time of flight . . . 97
A.2 Simulation analysis . . . 98
A.2.1 Atom cloud simulation . . . 98
A.2.2 Collision simulation . . . 99
A.3 Extended interaction potential fitting routine . . . 100
A.4 Data analysis and uncertainty calculation . . . 103
A.4.1 Data analysis for the rate coefficient measurements . . . 103
A.4.2 Uncertainties . . . 106
A.4.3 Results for the uncertainty estimation . . . 107
A.5 Overlap factor . . . 110
A.6 Population of Rb in the $(5s)^2P_{3/2}$ state . . . 111
A.7 Laser shutter and Oven controller . . . 111
A.8 Polarisation stabilisation . . . 112

B Appendix Electronics *113*

B.1 Polarisation stabilisation . . . 113
B.1.1 How polarization fluctuations are introduced in the experiment . . . 113
B.1.2 Construction . . . 114
B.1.3 Photodiodes . . . 115
B.1.4 Setup . . . 117
B.1.5 Adjusting . . . 118
B.1.6 Troubleshooting . . . 120
B.2 Oven controller, laser shutters . . . 120

Bibliography *121*

1 Introduction

Among laymen, the general idea of chemistry is spun around laboratories full of glassware filled with liquids, tubes, Bunsen burners, powdery substances and fume hoods. In this image, the work of a chemist is centred around mixing liquids, preparing compounds and dissolving crystals in solvents. While this is partly true, it only describes a small fraction of the work of a chemist. However, this work inherits a fundamental hurdle to overcome. When large amounts of atoms, molecules or ions interacting in an ensemble, the interactions of single particles are essentially impossible to investigate. They must be inferred from the properties of the entire ensemble. To investigate and understand single-particle interactions, an interdisciplinary exchange between atomic, molecular and optical (AMO) physics and chemistry presents two fundamental methods to circumnavigate this bottleneck. First, the cooling of particles from room-temperature velocity distributions to the so-called cold regime with temperatures below 1 K, opening doors to the world of cold chemistry. Second, the trapping of such particles, resulting in a localised positioning of the target within a narrow region of space and hindering them to thermalise with the environment in which the experiment is taking place.

Cooling of particles. A well-known method for cooling particles is supersonic expansions. Particles in the gas phase are expanded from a high pressure zone into a low pressure zone and undergo many collisions, while accelerating away from the high pressure zone. Local speeds rapidly exceed the local speed of sound and as the expansion continues, the distribution of speeds decrease as well as the collisional rate. This results in a narrow spread of velocities around the mean and a transversal velocity distribution of a temperature within a few K. Particles entrained in the packets will have their rotational degrees of freedom effectively cooled. Skimmers are used to select the coldest and densest central part of the expansion. Henson *et al.* presented a wonderful example of the benefits of supersonic expansion in the field of cold chemistry with their "Observation of quantum effects in sub-kelvin cold reactions" [11]. Their experimental setup merges two supersonic expanded beams to achieve collision energies below 1 K. A drawback in this and other supersonic expansion experiments is that samples only stay cold for a short time period, thus limiting the interaction time of the particles involved and the interrogation time of their resulting products. Fundamental achievements within the field of laser-cooled charged and neutral atoms (Nobel prizes 1989, 1997 , 2001 and 2012) paved

the way to an alternate route of cooling particles. Particles to be cooled need a compatible internal energy level structure which can be addressed by laser light [12–14]. The momentum transfer of the absorption and re-emission of photons will eventually slow the particles down. To maximise the effect of laser cooling, a large number of photons needs to be scattered, thus the particle must return to its initial state after re-emission with a probability close to unity, i.e. it has a closed optical cycle. If not, it will become trapped in a metastable state and will be lost from the cooling cycle. This is prevented by an additional laser addressing this metastable state and returning it into the cooling cycle. A more detailed description of light matter interaction, laser cooling and the relevant energy level structure for this works particles is found in section 2.2.2. The great benefits of this method are cooling to temperatures in the mK regime and below, as well as the fact that particles can be cooled indefinitely (unless they are lost to collisions with background gas).

Trapping of particles. Laser cooling produces a velocity dependent force and thus is not capable of confining particles in a narrow region. Trapping occurs when position-dependent forces act on neutral or charged particles. To efficiently trap these particles, different methodologies were developed. Neutral particles can be trapped in three different ways: purely magnetic [15], in a tightly focused laser beam detuned from resonance of a transition generating a potential to confine the particle through optical dipole force [12, 16] or, the most important for this work, the combination of cooling laser beams and an inhomogeneous magnetic field known as the magneto-optical trap [17]. For charged particles, the trap is realised either with a tightly focused laser beam (traps only a small number of particles, see Ref. [18]) or using electric fields to apply strong forces on the particle.
Earnshaw's theorem states that charged particles can not be held in a stable equilibrium by a static electric field. Therefore, the two trapping methods widely used are Penning traps [19], using an electrostatic potential with a magnetic field, and, the method of choice for this work, Paul [20] traps based on a fast oscillating electric field at frequencies on the order of megahertz. The combination of the magneto-optical trap and a radiofrequency ion trap forms a so-called hybrid trap which is discussed in section 2.2.

Cold ion chemistry. Reaction dynamics of atomic and molecular ions with neutral atoms at temperatures below 1 K is known as cold ion chemistry. The progress in recent years as a result of the development of techniques for the combined ("hybrid") trapping of cold atoms and ions [21–26] is most important for this work. Achievable temperatures in the mK regime in these experiments establish new capabilities for the comprehensive study of collisional and chemical dynamics at the quantum level. Investigations into the interactions between cold atomic ions and neutral atoms contributed tremendously to the understanding of cold reactive processes [27–31], the sympathetic and internal cooling of ions by ultracold atoms [5, 32, 33], cold three-body recombination dynamics [34], spin-exchange and -relaxation processes [35]

and the statistical mechanics of trapped ions in a cold buffer gas [36, 37].
Although a considerable amount of studies cover a wide range of atomic collisions systems, investigations into cold collisions with molecular ions are a few and scattered. In 2008, combinations of cold molecular beams or cryogenic gases with trapped ions [1, 2] were introduced. Allmendinger *et al.* examined the merging of molecular beams containing Rydberg molecules [3]. However, the most important studies for this work are investigations with sympathetic cooling of molecular ions in hybrid trapping experiments [4–7], uncovering unusually fast kinetics [4], the formation of exotic molecular species [6] and reaction blockading of short-lived excited species [7] in cold molecular ion-neutral atom systems.
Radiative coupling of the entrance channel to energetically lower-lying CT channels [38] or non-adiabatic coupling between channels [39] are the two avenues promoting charge-transfer (CT), which was found to be a dominating reactive process so far in hybrid trapping experimental studies. In the work of Hall *et al.* on reactions between N_2^+ molecular ions and Rb atoms [4] at collision energies around 20 mK, the CT rate coefficient was found to be extremely fast in collisions with excited Rb $(5p)\ ^2P_{3/2}$ atoms, contrary to reactions with ground-state Rb $(5s)\ ^2S_{1/2}$ atoms. Their resulting CT rate coefficients were observed to be considerably slower than the Langevin limit which frequently serves as a benchmark for ion-molecule reactions [40]. In the Langevin picture, the rate coefficient is limited by capture of the collision partners by long-range ion-induced dipole interactions whereas the short-range reaction probability is assumed to be unity [41].
These results hinted at the importance of the interplay between short- and long-range effects in cold CT reactions. Here, a comparative study of the CT between molecular oxygen ($^{32}O_2^+$), nitrogen ($^{28}N_2^+$) and dinitrogen monohydride ($^{28}N_2\ ^1H^+$) ions with ^{87}Rb atoms, using experiments in the cold regime, is the main goal of this thesis. This work builds on the experimental work by Hall [10] and Eberle [8].

1.1 Outline of the thesis

This thesis consists of three complementary parts, two theoretical and one experimental: 1) The theoretical investigation of of the properties of a shuttling atom cloud used in the collision experiments. 2) The study of the role of inelastic collisions under the present experimental conditions as well as the loss of molecular ions through radiative association and in the experimental exploration of the CT between molecular O_2^+, N_2^+ and N_2H^+ ions with Rb atoms. The first part enables the identification of stable experimental conditions for the shuttling atom cloud by theoretically exploring the achievable kinetic-energy spreads and kinetic energies. The second assessed the importance of inelastic collisions under the present experimental conditions and investigated if these processes play a major role compared to the reaction dynamics as well as if there is ion loss from the trap due to radiative association as seen in the atomic-ion studies with Ca^+ [27] and Ba^+ [25, 30]. 3) The discussion of the

experimental and theoretical results of CT dynamics and presents the main part of this work. Chapter 2 introduces the theoretical concepts of cold ion - neutral collisions and reactions and the necessary background for hybrid trapping. Chapter 3 introduces the experimental setup and the two different experimental modes used in the present hybrid - trapping studies: stationary atom cloud and shuttling atom cloud. Chapter 4 is the in - depth explanation of the simulation for the shuttling atom cloud with the computational code discussed in Appendix A. Chapter 5 discusses rotational state - changing collisions and radiative association of $N_2^+ + Rb$. The experimental and theoretical results of the CT collision experiments with molecular ions are discussed in Chapter 6. Chapter 7 presents the concluding remarks of this thesis and briefly discusses an outlook on the future of these experiments. The Appendix includes all necessary computational code (A), electronics (B) applied in the experiment and the data analysis, the CV (C).

2 Theoretical concepts

2.1 Cold ion - neutral collisions and reactions

Cold collisions in this work refers to collisions where the collision energy is in the range $1\,\mathrm{mK} \leq E_{\mathrm{coll}}/k_{\mathrm{B}} \leq 1\,\mathrm{K}$, where the collision energy is given in units of Kelvin. For investigations of cold ion - neutral collisions at these low energies, the boundaries between the classical and quantum realm become indistinct. To compare experiments with predictions of theoretical models, both have to be taken into account. The classical model [42] was formulated in 1905. Together with quantum models [43, 44], they are commonly used to quantify collisional and reactive processes. The following subsections will discuss the theoretical background needed to understand the reaction dynamics described in this work and will focus on the Langevin theory and an extended interaction potential, which will be needed to discuss the experimental results in Chapter 6.

2.1.1 Capture - model and effective potentials

Given two structureless particles in free space and unperturbed by their environment, the classical capture model, presented in Figure 2.1a, predicts both particles react with each other with unit probability for all trajectories with enough energy to overcome the barrier $V_{\mathrm{eff}}(R_{\mathrm{max}})$ [45]. The three parameters of the particles needed to calculate the total energy are their relative velocity v, their distance R and their impact parameter b [45]. The impact parameter b is the closest distance of the particles in the absence of an interaction potential. The total energy of the unperturbed system is then given by (2.1), linking the pre - collision energy ($R = \infty$) to energies at finite R values. The dominant term of the equation is the initial kinetic energy of the collision. However, the closer the two particles approach each other, the more influence will be coming from the R^{-2} - term, which represents the centrifugal energy.

$$E_{\mathrm{T}} = \frac{\mu}{2}\left(\frac{\mathrm{d}\,R}{\mathrm{d}\,t}\right)^2 + \frac{E_{\mathrm{T}}\,b^2}{R^2} \tag{2.1}$$

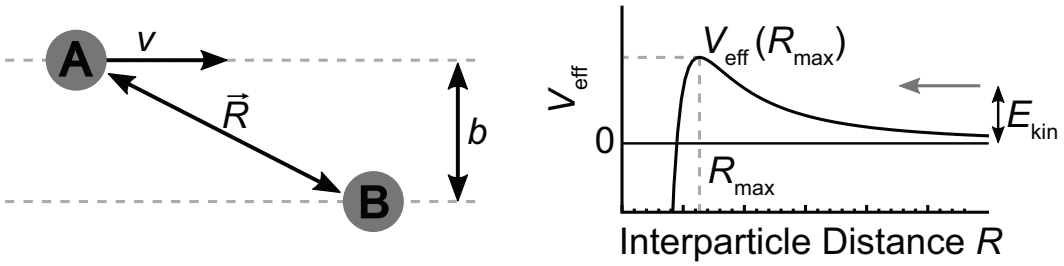

(a) (b)

Figure 2.1: (a) Two structureless particles 'A' and 'B' approaching each other at a velocity v and a distance $\vec{R}$ with an impact parameter b. (b) Effective potential $V_{\text{eff}}(R_{\text{max}})$ energy dependence as a function of interparticle distance R at a kinetic energy E_{kin}. The peak of the effective potential at R_{max} describes the centrifugal barrier. (These figures are adapted with permission from Ref. [8]).

Each new interaction potential, representing a new force, can be added to the basic model Equation (2.1), as presented in Equation (2.2)

$$E_{\text{T}} = \frac{\mu}{2}\left(\frac{\mathrm{d}R}{\mathrm{d}t}\right)^2 + \frac{E_{\text{T}}b^2}{R^2} + V(R). \tag{2.2}$$

A new effective potential, following

$$V_{\text{eff}} = \frac{E_{\text{T}}b^2}{R^2} + V(R), \tag{2.3}$$

can be formulated. The effective potential exhibits a maximum at R_{max} (see Figure 2.1b), if the interaction potential is purely attractive which is directly linked to the impact parameter b. In the case where the long-range part of the potential $V(R)$ is of the form of R^{-s} where $s > 2$, the critical impact parameter b_{max} for a collision is found by requiring that the collision energy is equal to $V_{\text{eff}}(R_{\text{max}})$. b_{max} can be thought of the maximum distance between the two particles at which collisions still occur. Collisions at the critical impact parameter b_{max} result in the particles being in a stable orbit of one another. For the particles to reach short internuclear distances, the impact parameter must be $b \leq b_{\text{max}}$. The collisional cross section can hence be calculated by $\sigma = \pi b_{\text{max}}^2$. The rate coefficient of the collisions can subsequently be defined by multiplying the collisional cross section σ with the impact velocity v, $k = \sigma v$. The effective potential is dependent on the nature of the collision partners. The long-range part of the interaction potential $V(R)$ may be described by

$$V(R) = \sum_{n=1}^{\infty} \frac{C_n}{R^n}, \tag{2.4}$$

where C_n are long-range coefficients which can be derived from a multipole expansion of the interspecies interaction operators [46, 47].

2.1.2 Langevin rate coefficients and cross sections

The simplest approach to understand collisions between charged and neutral particles is the Langevin theory. For collisions in an electronic state with $l = 0$ the only relevant long - range coefficient is the charge - induced dipole

$$C_4 = -\frac{1}{2}\left(\alpha_0 + \frac{3\Lambda^2 - 6}{6}\alpha_2\right), \tag{2.5}$$

where α_0 is the isotropic polarisability and α_2 the tensor polarisability. l is the angular momentum associated with the electronic state of the neutral reaction partner. For the case of $l = 0$, the tensor polarisability α_2 is imperceptibly small. The charge - permanent quadrupole moment and any other interaction potential with $n > 4$ can be ignored, hence the resulting interaction potential of the combination of Equation (2.4) and $E_T b^2/R^2$ is

$$V(R) = -\frac{\alpha_0}{2R^4}. \tag{2.6}$$

Using this as the effective potential and solving (2.2) for the critical impact parameter b_{max}, results in the Langevin cross - section σ_L in the form of

$$\sigma_L = \pi\left(\frac{2\alpha_0}{E_T}\right)^{1/2}. \tag{2.7}$$

From this, the Langevin rate coefficient can be written as

$$k_L = 2\pi\left(\frac{\alpha_0}{\mu}\right)^{1/2}. \tag{2.8}$$

The Langevin rate coefficient is not collision energy dependent. In this work, this is applicable for experiments with Rb in the $(5s)\ ^2S_{1/2}$ ground state. However, for the experiments with Rb in the electronically excited state $(5p)\ ^2P_{3/2}$, which has an orbital angular momentum of $l = 1$, the Langevin model is not applicable. In this case, the charge - induced dipole (C_4) and the charge - permanent quadrupole (C_3) play a role in the long - range interaction.

2.1.3 Extended interaction potential

Potential and dispersion coefficients

According to Krych *et al.* [47] the potential can be adopted as follows:

$$V(R) = \frac{C_3}{R^3} - \frac{C_4}{R^4}, \tag{2.9}$$

with (2.5) and

$$C_3 = (-1)^{l+\Lambda}\begin{pmatrix} l & 2 & l \\ -\Lambda & 0 & \Lambda \end{pmatrix}\langle l||Q_2||l\rangle, \tag{2.10}$$

where l,Λ denote the orbital angular momentum associated with the neutral reaction partner ($l = 1$,Λ=0,$\pm$1) and Q_2 the quadrupole moment. The charge - permanent quadrupole interaction is presented in (2.10) and is comparable with [48] and (2.5) denotes the charge - induced dipole interaction.

Calculations of $\langle l||\mathbf{Q}_2||l\rangle$

The reduced matrix element for a single electron atom (based on Appendix B, D and page 13 ff. in Ref. [49]), neglecting spin - orbit interaction, can be reformulated using the modified spherical harmonics $C_{lm}(\theta,\phi) = \sqrt{\frac{4\pi}{2l+1}}Y_{lm}$, where Y_{lm} are the spherical harmonics, to give after application of the Wigner - Eckart theorem [50]

$$\langle l||Q_2||l\rangle = -\frac{e}{2}\langle r^2\rangle\,\langle l||C_2||l\rangle = -\frac{e}{2}\langle r^2\rangle(-1)^l(2l+1)\begin{pmatrix} l & 2 & l \\ 0 & 0 & 0\end{pmatrix}, \tag{2.11}$$

where e is the elementary charge and $\langle r^2\rangle$ is the square of the mean radius of the valence electron. Inserting Equation (2.11) into the expression for C_3 (2.10) then

$$C_3 = -\frac{e}{2}\langle r^2\rangle\left\{(-1)^\Lambda\begin{pmatrix} l & 2 & l \\ -\Lambda & 0 & \Lambda\end{pmatrix}(2l+1)\begin{pmatrix} l & 2 & l \\ 0 & 0 & 0\end{pmatrix}\right\}\frac{e}{4\pi\epsilon_0}. \tag{2.12}$$

For the Rb (5p) $^2P_{3/2}$ level, $l = 1$ and hence $\Lambda = 0, 1$ relating to two possible symmetries with which a p orbital can approach an ion. Evaluation of the $3j$ symbols of Equation (2.12) for the two symmetries Σ and Π gives

$$l = 1, \Lambda = 0 : C_3 = -\frac{e}{2} < r^2 > \left(+\frac{2}{5}\right)\frac{e}{4\pi\epsilon_0} \tag{2.13}$$

$$l = 1, \Lambda = 1 : C_3 = -\frac{e}{2} < r^2 > \left(-\frac{1}{5}\right)\frac{e}{4\pi\epsilon_0}. \tag{2.14}$$

2.2 Hybrid Trapping

The definition of a hybrid trap is the combination of a trap for neutral particles and a trap for charged particles in close vicinity such that the two species to interact. In the following subsections, the setup of such a system and the theoretical background knowledge will be discussed in more detail.

2.2.1 A brief history on hybrid traps

Hybrid traps started with theoretical calculations of R. Coté [43] and subsequently the first proposal for implementation of a hybrid trap system by W. Smith [51]. Their work paved the

way to cold and ultra cold ion - neutral collisions and was followed by many new implementations, like the first surface - electrode ion trap combined with a magneto - optical trap [52], linear Paul traps with a magneto - optical traps (MOT) [28, 53–56] and even colder neutrals in Bose Einstein condensates (BEC) [29, 32, 57]. In our group, the hybrid trap system was introduced by Hall [27] with his work on atomic ion - neutral collisions and molecular ion - neutral collisions in a linear Paul trap superimposed with a magneto - optical trap. The main focus of all the experiments mentioned above was to elucidate the dynamics collisions and of chemical reactions with high precision and at very low temperature and to uncover the quantum dynamically driven complexity of single particle, and in the case of BECs, multiparticle reaction dynamics. All of these experiments have one thing in common: they all use stationary ions and stationary neutrals. With our new approach [9], the door to dynamically controllable collision energies was open and followed by Puri *et al.* [58] with a slight different approach by shuttling the ions instead of the neutrals. One of the most interesting systems is the idea followed in the thesis of Rouse [59]. He designed an ion - atom hybrid trap based on a surface - electrode ion trap combined with a BEC, with the ability to move the BEC to control collision energies. To accomplish all these experiments, one first has to understand the basic theoretical concepts of the traps involved.

2.2.2 Interaction of light with matter

To understand how it is possible for light to act forces on charged and neutral particles and helping to cool them, as well as prevent them from escaping a trap, one should start with a simple two level system. Foot [60] starts his discussion with a semi - classical theory of light - matter interaction. In his book the atom is treated quantum mechanically and the light as a classical electromagnetic wave. This semi - classical description is limited to the case where a large number of photons are scattered. With the Schrödinger equation for the semi - classical theory approximated for a two level system, the Rabi equations can be solved analytically. The resulting populations P_g and P_e of the ground and excited state, respectively, oscillate with a characteristic frequency according to

$$P_g(t) = \frac{|\Omega_R|^2}{\Omega} \cos^2\left(\frac{\Omega t}{2}\right) + \frac{\delta}{\Omega^2}, \tag{2.15}$$

$$P_e(t) = \frac{|\Omega_R|^2}{\Omega} \sin^2\left(\frac{\Omega t}{2}\right), \tag{2.16}$$

where $\delta = \omega_{eg} - \omega$ is the shift of the laser frequency ω to the frequency of the transition ω_{eg} (detuning), Ω_R is the Rabi frequency and $\Omega = \sqrt{|\Omega_R|^2 + \delta^2}$ the effective Rabi frequency. Further, one has to include the spontaneous emission, because the coupling of the atomic dipole to the electromagnetic vacuum modes is not negligibly weak. The resulting optical Bloch equations are then solved. This incorporates the lifetime of the excited state and hence the decay rate of the excited state populations Γ, equivalent to the natural line width at full

width at half maximum (FWHM) [61] of the corresponding spectral line. From the optical Bloch equations, the steady state populations (populations of the states in equilibrium) can be derived, thus the excited state population is deduced

$$\rho_{ee} = \frac{\Omega_R^2}{\Gamma^2 + 4\delta^2 + 2\Omega_R^2}. \tag{2.17}$$

A more intuitive form of Equation (2.17) is possible by introducing the intensity of the laser I, the saturation intensity of the transition I_S and the saturation parameter S_0

$$I_S = \frac{\hbar\Gamma\omega_{eg}^3}{12\pi c^2}, \tag{2.18}$$

$$S_0 = \frac{I}{I_S} = \frac{2\Omega_R^2}{\Gamma^2}. \tag{2.19}$$

The theoretical saturation intensity for the $|F = 2, m_F = \pm 2\rangle \rightarrow |F' = 3, m_F' = \pm 3\rangle$ cycling transition ($\sigma^{\pm}$ - polarised light) according to [61] is $I_S = 1.669(2)\,\mathrm{mW\,cm^{-2}}$. In an experimental study by Shah *et al.* [62] of the excited state fraction of a magneto - optical trap, the calculated saturation intensity, which matched the experimental results, was determined to be $I_S = 9.2(17)\,\mathrm{mW\,cm^{-2}}$. This is also the saturation intensity used in this work. The steady state population now reads

$$\rho_{ee} = \frac{S_0/2}{1 + S_0 + \left(\frac{2\delta}{\Gamma}\right)^2}. \tag{2.20}$$

To maximise the excited state population the saturation parameter has to approach infinity, thus the laser intensity I becomes infinitely large and the population approaches 1/2 (saturation of the transition). Multiplying the excited state population by the natural linewidth of the transition results in the photon scattering rate

$$\Gamma_{Ph} = \rho_{ee}\Gamma. \tag{2.21}$$

Another effect which is directly linked to the laser intensity is power broadening. The lineshape has the from of a Lorentzian and the linewidth is $\Gamma_L = \Gamma(1 + S_0)$ at FWHM. It can be seen that the larger the laser intensity the broader the line will be.

Light forces

Dating back to James Clerk Maxwell is the idea that radiation has momentum (and energy) [63]. Therefore when an object absorbs radiation its momentum changes, while the force equals the rate at which the light delivers momentum. Thus the radiation of intensity I exerts a force on area A given by $F_{rad} = IA/c$ with c being the speed of light. For a counter - propagating laser beam the force exerted on an atom can be described by $F = -\sigma_{abs} I/c$, where the minus sign indicates a force in the opposite direction to the motion. As Foot [60]

notes the radiation forces have a dramatic effect on atoms, since the peak absorption cross section $\sigma_{abs}(\omega_0)$ is often much greater than the physical size of an atom. In alkali atom vapours, a large fraction of their absorption strength is concentrated in a narrow range centred at the frequency of the resonance line [60]. For convenience, the process can be described in terms of photons. De Broglie proposed the concept of the behavioural equality of matter and waves, thus matter waves are called de Broglie waves and their respective de Broglie wavelength is known to be $\lambda = h/p$ (momentum p). Relating $k = 2\pi/\lambda$ and $\hbar = h/2\pi$, this can be rewritten as $p = \hbar k$. The magnitude of the scattering force can now be formulated in terms of the rate at which the absorbed photons transmit momentum to the atom. Since the photon scattering rate Γ_{Ph} saturates at $\Gamma/2$, the maximum of the force is

$$F = \hbar k \Gamma_{Ph} = \frac{\hbar k \Gamma}{2}. \tag{2.22}$$

Rearranging Equation (2.22), the maximum possible acceleration is

$$a_{max} = \frac{F_{max}}{m} = \frac{\hbar k \Gamma}{2m} = v_r \frac{\Gamma}{2}, \tag{2.23}$$

where v_r is the recoil velocity

$$v_r = \frac{\hbar k}{m}. \tag{2.24}$$

Nowadays, a most frequently used and well known application in the physics community is exploiting the light forces to decelerate or accelerate particles.

Dopper laser cooling

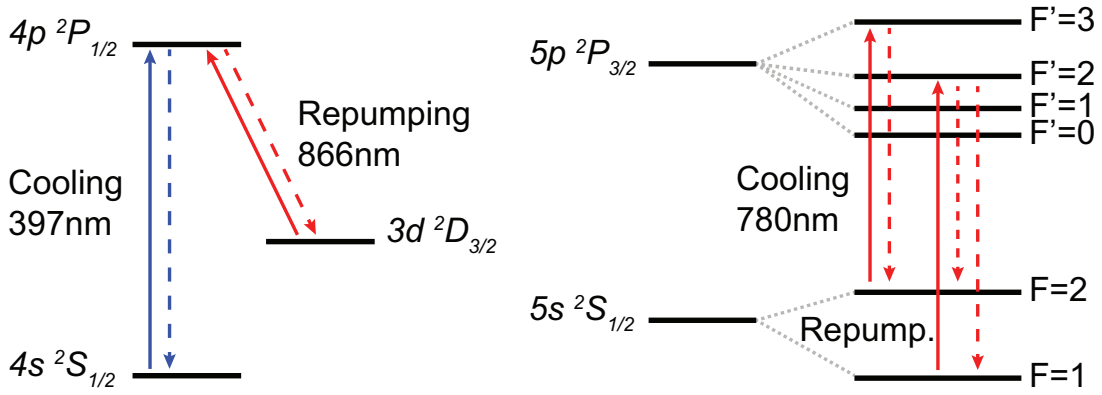

(a) (b)

Figure 2.2: Schematic of the energy level structure of Ca^+ (a) and Rb (b) utilised for laser cooling.(These Figures are adapted with permission from Ref. [8]).

Scattering tens of thousands of photons on a target particle will change its momentum and, applied correctly, it will reduce the particles average momentum, hence the particle will be

cooled. To scatter as many photons as possible it is necessary that the particle has a closed cycle of absorption, requiring a simple a energy level structure. Atoms are the preferred species, although there are some molecules with similar properties, such as SrF [64, 65], YO [66], CaF [67, 68] and SrOH [14]. In this work, however, the well-established cooling of single calcium ion and neutral rubidium atoms was chosen. Their energy level structure relevant for the cooling cycle is depicted in 2.2a for Ca^+ ions and 2.2b for Rb atoms. For Ca^+ the main cooling transition is driven by a 397 nm laser between the $(4s)\ ^2S_{1/2}$ and the $(4p)\ ^2P_{1/2}$ levels and for Rb atoms it is driven by a 780 nm between $(5s)\ ^2S_{1/2}$ F=2 and $(5p)\ ^2P_{3/2}$ F'=3 levels. In the event of leaving the main cooling transition a second light source is needed to reallocate them. In case of Ca^+ ions this is the metastable $(3d)\ ^2D_{3/2}$, which can be addressed by a 866 nm laser. As for the Rb atoms, it is an off-resonant excitation into the $(5p)\ ^2P_{3/2}$ F'=2, which decays into the $(5s)\ ^2S_{1/2}$ F=1 level. This can then be addressed by an electro-optical modulator (EOM) inserted into the cooling laser beam generating side-bands at a frequency of 6.8 GHz, which is the hyperfine splitting between $(5s)\ ^2S_{1/2}$ F=1 and $(5s)\ ^2S_{1/2}$ F=2. With a closed cooling cycle to achieve cooling, the light forces must be dissipative and dependent on the velocity of the species. Dehmelt *et al.* [69] and Hänsch *et al.* [70] proposed in two independent papers in 1975 a simple and effective way based on the physics of the Doppler effect and thus called Doppler laser cooling. Figure 2.3 depicts the three steps in Doppler cooling. An atom with a velocity v interacts with an opposing laser field, assumed to be a running wave with a wave vector k and a frequency ω. The detuning of the laser frequency from the atomic transition at zero velocity is $\delta_0 = \omega - \omega_{eg}$, so including the Doppler effect, the total detuning is $\delta = \delta_0 - kv$. The scattering force now becomes

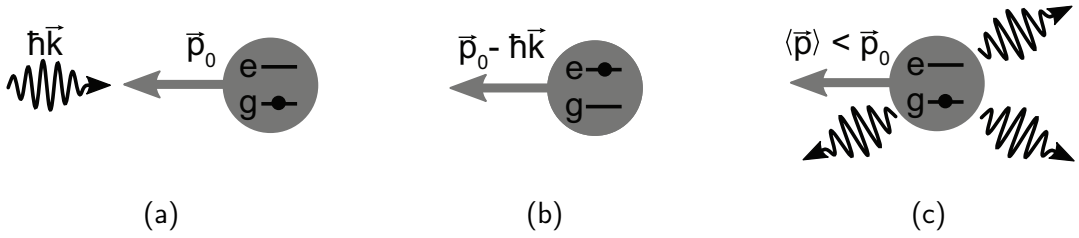

Figure 2.3: Illustrated are the three steps in Doppler laser cooling to reduce the translational energy of a particle. (a) shows an electro-magnetic wave interacting with a particle at velocity v in opposite direction. The particles is in its electronic ground state. (b) The particle has absorbed the momentum from the electro-magnetic wave and its electronic state is now excited. (c) The particle radiatively de-excites from the electronic state and releases a photon in a random direction.(This Figure is adapted with permission from Ref. [8]).

$$F = \hbar k \Gamma_{\mathrm{Ph}} = \frac{\hbar k \Gamma}{2} \cdot \frac{S_0}{1 + S_0 + 2\left(\frac{\delta_0 - kv}{\Gamma}\right)^2}. \tag{2.25}$$

A Taylor expansion to the first order for small v can be made around $v = 0$

$$F \approx F_0 - \beta v, \tag{2.26}$$

introducing a damping coefficient β for a single beam

$$\beta = -\hbar k^2 \frac{4S_0 \left(\frac{\delta_0}{\Gamma}\right)}{\left[1 + S_0 + 4\left(\frac{\delta_0}{\Gamma}\right)^2\right]^2}. \tag{2.27}$$

So for a $\delta_0 < 0$ (red detuning), $\beta > 0$, velocity v is damped, hence the species is cooled. The lower the velocity, the weaker the force on the atom. A maximum efficiency for the damping coefficient is achieved for $\delta_0 = -\Gamma/2$ and $S_0 = 2$ resulting in $\beta_{\max} = \hbar k^2/4$. Although this works until the atom is slowed to a stop, the atom will start accelerating again in the opposite direction afterwards, hence a single laser beam configuration is not suitable for cooling. Two counter - propagating laser beams are required. Each laser beam now has a damping force with opposite signs

$$F_{\pm} = \hbar k \Gamma_{\mathrm{Ph}} = \frac{\hbar k \Gamma}{2} \cdot \frac{S_0}{1 + S_0 + 2\left(\frac{\delta_0 \pm k v}{\Gamma}\right)^2}, \tag{2.28}$$

which simply can be added together for small saturation parameters. This results in the following damping force

$$F \approx -\beta v. \tag{2.29}$$

The F_0 terms in the Taylor Series expansion to lowest order in v of the sum cancel and the resulting damping coefficient is given by

$$\beta = 8\hbar k^2 \frac{S_0 \delta_0}{\left[1 + S_0 + 4\left(\frac{\delta_0}{\Gamma}\right)^2\right]^2}. \tag{2.30}$$

Extended to 3d, this configuration is known as the 'optical molasses configuration'. Since it is a velocity dependent force and no position dependent force, no trapping of the atoms occurs. Atoms with velocities larger than a critical velocity v_c will not be trapped. For Doppler cooling $v_c \approx \Gamma/k$. The corresponding experiment with three orthogonal pairs of counter - propagating laser beams was demonstrated in 1985 by S. Chu *et al.* [71]. The recoil of scattering a single photon in a random direction by spontaneous emission is limiting the minimum temperature an atom or ionic species can be cooled to with this method. The Doppler limit temperature T_D [12] is calculated by equating the rate momentum taken away by laser cooling and the rate of the random walk due to the recoil scattering. The actually achieved temperature might be even lower, since an atom is a multilevel system and thus additional cooling mechanisms are available [72].

$$k_{\mathrm{B}} T_{\mathrm{D}} = \frac{\hbar \Gamma}{2} \tag{2.31}$$

2.2.3 Atom trapping and cooling

Until now the discussion only investigated the damping force exerted on the atoms. With the optical molasses technique, densities in the interaction region can be increased from an atomic source above the background levels. However the atoms are free to drift out of this region or even get accelerated, since there is no potential which will hold the atoms in place. Recent years have shown many desired applications which depend on neutral atom trapping and have led to discoveries like Bose - Einstein condensation [73]. The advantages of trapped and cooled neutral atoms for this work are the controllable high local density and temperature to ensure enough reactions on a reasonable time scale. In the next paragraphs, the theory necessary to understand the trapping and cooling of neutral atoms is presented.

Discussion of a magneto optical trap

A workhorse technique to trap neutral atoms is the magneto - optical trap (MOT). It was first demonstrated by Raab *et al.* [17] in 1987. This trap combines the optical molasses technique of three pairs of orthogonal σ^+ and σ^- polarised laser beams of the same frequency with a quadrupolar magnetic field, whose magnitude is zero in the center, generated by anti - Helmholtz coils. This is depicted in Figure 2.4a.

From an optical molasses to a magneto - optical trap

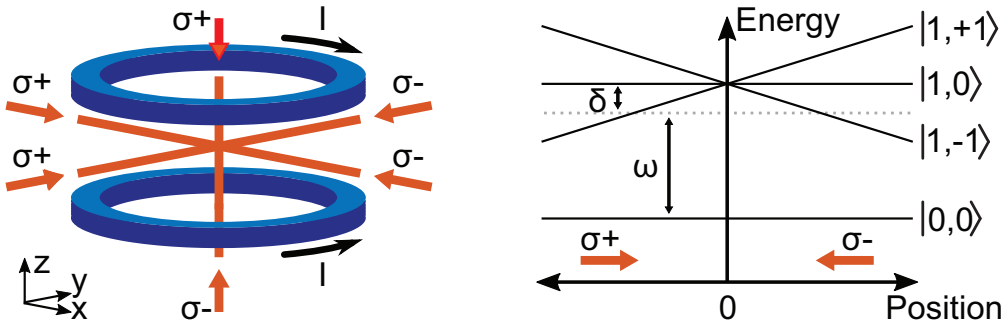

(a) (b)

Figure 2.4: (a) Schematic of a magneto - optical trap. The six counter - propagating laser beams are depicted in red labelled by their respective circular polarisation. The solenoids in anti - Helmholtz configuration are illustrated in blue labelled by their respective current flow direction. (b) Schematic quadrupolar of magnetic sublevels of an atom with a $J = 0$ ground and $J = 1$ excited state in dependence of the position in a quadrupolar magnetic field. The dotted line depicts the detuning of the cooling laser from the zero field atomic transition by δ. ω denotes the laser frequency of the cooling laser. (These figures are adapted with permission from Ref. [8])

The operation principle of the MOT is best described by reference to Figure 2.4b for a prototypical atom with a $J = 0$ ground and $J = 1$ excited state. The Zeeman formula $E_{\text{Zeeman}} = g_J \mu_B B m_J$ gives the linear energy shift of the magnetic sublevels with the magnetic field strength, thus shifting linear with distance from $z = 0$. The ground state of the discussed atomic species has only one magnetic sublevel $m_g = 0$. In the case of the excited state there are three magnetic sublevels $m_e = +1,0,-1$. Consider an atom moving away from the trap center, hence increasing the strength of the magnetic field. If this atom is moving in $+z$ direction, the magnetic sublevel $|J, m\rangle = |1, -1\rangle$ is brought closer to resonance with the σ^- polarised cooling laser, while the magnetic sublevel $|1, 1\rangle$ is shifted out of resonance. The $|1, 0\rangle$ level is unaffected by the magnetic field. The selection rules state that $m_e = -1$ can only be addressed by σ^- and $m_e = +1$ only by σ^+ polarised light from $m_g = 0$. The σ^- beam is propagating along $-z$ direction, meaning the net momentum after scattering of these photons results in the same direction, hence forcing the atoms to move towards $z = 0$. The situation is reversed when the atom starts moving in $-z$, when the σ^+ photons get scattered and the atom gets restored towards $z = 0$. Equation (2.32) is the mathematical expression for the force on an atom in the field of two counter-propagating laser beams modified by Equation (2.33)

$$F_\pm = \frac{\hbar k \Gamma}{2} \cdot \frac{S_0}{1 + S_0 + (\frac{2\delta_\pm}{\Gamma})^2} \tag{2.32}$$

$$\delta_\pm = \delta_0 \mp k v \pm \frac{\mu' B}{\hbar} \tag{2.33}$$

where

$$\mu' = (g_e m_e - g_g m_g)\mu_B \quad \text{and} \quad B = A \cdot z. \tag{2.34}$$

The subscripts e and g refer to excited and ground state, respectively. Given the displacements and the velocities are small close to the magnetic field zero, Equation (2.32) can be reformulated to

$$F \approx -\beta v - \kappa z, \tag{2.35}$$

where β is the same as in Equation (2.30) and κ is

$$\kappa = \frac{\mu' A}{\hbar k} \beta. \tag{2.36}$$

Here, κ is the spring constant of the approximately harmonic potential of the MOT, thus the trap frequency can be calculated as $\omega_{\text{MOT}} = \sqrt{\kappa/m}$. The magnetic field gradient along the z-axis has half the magnitude of the magnetic field gradient along either the x-axis or the y-axis. This leads to two degenerate trap frequencies along x and y and a third along z. It is noteworthy that collective effects (interparticle interaction, light shadowing effects,...) of uncharged particles only occur at higher phase-space densities than in the present experiment. This concludes the first part of the hybrid trap. A more detailed discussion on magneto-optical trapping can be found in Ref. [60].

2.2.4 Ion trapping and cooling

Ions are trappable with light alone. Recent experiments have proven so [18]. Although this work showed the trapping of a string of ions in a dipole trap, the life time of the ions in the optical trap and the number of ions trappable is limited. In the present work, however, the number of ions is much larger and hence a linear Paul trap is used. This trap exploits the ions' sensitivity to electric fields. It creates a dynamic electric field, which allows strong confinement of the ions. The electric fields have to be dynamic to trap an ion, as according to Earnshwa's theorem [60] electrostatic interaction is not able to keep charged particles in a stable stationary equilibrium. For a full 3d confinement of the ions, additional electrostatic fields are used. A brief example of the many different trap types in existence can be found in Ref. [19]. This works' trap is illustrated in Figure 2.5 and follows the design in Ref. [74]. The main working principle of a such an radio - frequency (rf) ion trap and theoretical background to characterise the important quantities such as trap frequencies, trap depth for different ions and kinetic ion energy within the trap will be described below.

Equations of motion (EOM) for charged particles in a linear Paul trap

Previous works on focusing of molecular beams by W. Paul *et al.* [75, 76] and the following work concerning particle optics [77] led to the development of the design and function of the well known linear Paul trap which is outlined in the book 'Ein Ionenkäfig' by Paul *et al.* [20]. The Linear Paul trap was developed only very much later by Prestage *et al.* [78]. Four rods with oscillating rf voltages are used. The frequency and the amplitude is chosen according to the mass to charge ratio of the ions which ought to be trapped. To calculate the 3d properties of this dynamic trapping of the ions, a 3d potential of the form of $\Phi = \alpha x^2 + \beta y^2 + \gamma z^2$ is assumed. For the Laplace equation

$$\nabla^2\Phi = \frac{\partial^2\Phi}{\partial x^2} + \frac{\partial^2\Phi}{\partial y^2} + \frac{\partial^2\Phi}{\partial z^2} = 0, \tag{2.37}$$

to be satisfied, it requires the coefficients to follow $\alpha + \beta + \gamma = 0$. A common way to comply is to chose the coefficients as follows: $\alpha = \beta = -2\gamma$, leading to a radially symmetric 3d trap [79]. The radial confinement of the ions is generated with a time varying electric potential of the form of

$$V(x, y, t) = V_{0\mathrm{p}} \left(\frac{x^2 - y^2}{r_0^2} \right) \cos(\Omega_{\mathrm{rf}} t), \tag{2.38}$$

where $V_{0\mathrm{p}}$ is the zero to peak rf voltage, Ω_{rf} the angular frequency of the rf voltage and r_0 is the inscribed radius of the rods. Axial confinement is achieved with a static electric potential in axial direction

$$U(x, y, z) = \frac{\kappa V_{\mathrm{end}}}{z_0^2} \left[z^2 - \tfrac{1}{2}(x^2 + y^2) \right], \tag{2.39}$$

where κ is a geometrical factor determined from calculations in the multiphysics modeling software COMSOL [80], based on the geometrical design of the trap. V_{end} is the applied endcap voltage. z_0 is half the distance between the endcap electrodes. The harmonic potential above applied to an experimentally 'ideal' ion trap with the most favourable conditions dictates that the radius r of the rods themselves is approximately equal to r_0 [81].
Acceleration a of an object is dependent on the force F acting on an object with a mass m (Newton's second law). In case of a particle with charge Q in an electric field $\mathbf{E}$, the force is $F = Q\mathbf{E}$ and the acceleration is the second derivative of the displacement vector $\mathbf{r}$. This rewrites Newton's second law to

$$Q\mathbf{E} = m\ddot{\mathbf{r}}. \tag{2.40}$$

The electric field is the gradient of the electric potential and inserting the dynamic potential Equation (2.38) and the static potential Equation (2.39), the Mathieu equation describing the motion of an ion can be written in the general form

$$\frac{d^2}{d\tau^2} i + (a_i + 2q_i \cos(\Omega_{\text{RF}} t)) i = 0, \tag{2.41}$$

where $i = x,y,z$ with the Mathieu stability parameters given as

$$a_x \approx a_y \approx -\frac{1}{2} a_z = \frac{-4\kappa Q V_{\text{end}}}{m\Omega_{\text{RF}}^2 z_0^2} \tag{2.42}$$

$$q_x \approx -q_y \approx \frac{4QV_{0,\text{RF}}}{m\Omega_{\text{RF}}^2 r_0^2}, \quad q_z = 0 \tag{2.43}$$

An analytical solution for the Mathieu equation can be given in the limit $|a_i| << 1$ and $|q_i| << 1$

$$r_i(t) = r_{1i} \cos(\omega_i t + \phi) \left[1 + \tfrac{q_i}{2} \cos(\Omega_{\text{RF}} t)\right], \tag{2.44}$$

with

$$\omega_i = \tfrac{1}{2}\Omega_{\text{RF}} \sqrt{a_i + \tfrac{1}{2} q_i^2}. \tag{2.45}$$

r_{1i} is the amplitude of motion in direction i and ϕ is a phase determined by the conditions of the initial position and velocity of the ion. The mass dependent harmonic (secular) frequencies are given by ω_i. Two different motions of the ion are described by (2.44). The first term quantifies a slow secular motion with a large amplitude and the second a fast oscillatory motion of the ion with a much smaller amplitude, due to the dynamic nature of the rf-fields. The radial directed secular motion of the ion is often approximated with a time-independent pseudo potential U_{Pseudo}. It corresponds to the average kinetic energy stored in the micromotion is given by

$$U_{\text{Pseudo}}(r, z) = \frac{1}{2}\omega_r^2 r^2 + \frac{1}{2}\omega_z^2 z^2, \tag{2.46}$$

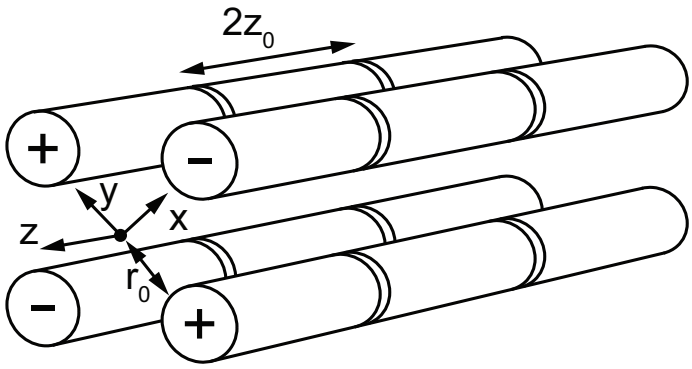

Figure 2.5: A schematic illustration of a 12 segment linear Paul trap with four rods. Three segments in z direction combine to a rod. The two rods labeled with a '+' carry the same rf and the two labeled with a '−' carry a 180° phase shifted rf. In addition all 12 electrodes can be addressed with static electric fields. (This figure is adapted with permission from Ref. [8]).

with the radial frequency ω_r and the axial frequency ω_z

$$\omega_r = \Omega_{\mathrm{RF}}\sqrt{a + \frac{1}{2}q^2}, \quad \omega_z = \Omega_{\mathrm{RF}}\sqrt{-2a} \quad \text{and} \quad r^2 = x^2 + y^2. \tag{2.47}$$

Since the secular frequencies are mass - dependent, a method to determine the mass - to - charge ratio of the ion inside the trap is possible. The method relies on resonantly exciting the secular motion of the ionic mass in question by applying an additional rf field at low amplitudes to specific electrodes of the trap, hence the name is resonant - mass excitation spectroscopy [82].

Ion kinetic energy, excess micromotion

$$E_{\mathrm{kin,ion}} = \frac{1}{2}m\langle \dot{r}_{1i}\rangle \cong \frac{1}{4}mr_{1i}^2\omega_i^2 \cdot \left(\underbrace{1}_{\text{secular motion}} + \overbrace{\frac{q_i^2}{q_i^2 + 2a_i}}^{\text{micromotion}} \right) \tag{2.48}$$

is the kinetic energy of an ion, where r_{1i} equals to the outermost point of the ions trajectory. Given $q_z = 0$, the purely secular energy is for the axial motion along z is obtained obtained, which is thermal and can be expressed as

$$E_{\mathrm{kin,ion,z}} = \frac{1}{2}k_B T_z \cong \frac{1}{4}mr_{1z}^2\omega_z^2. \tag{2.49}$$

T_z is a characteristic temperature of a laser cooled ion. The radial components on the other hand are strongly influenced by the micromotion, typically $|a_i| << q_i^2$ for $i = x, y$

$$E_{\mathrm{kin,ion,i}} = k_B T_i \cong \frac{1}{2}mr_{1i}^2\omega_i^2. \tag{2.50}$$

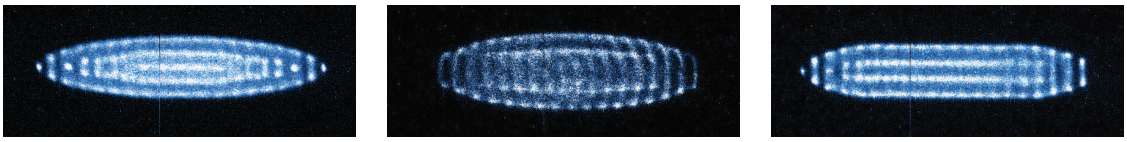

(a) (b) (c)

Figure 2.6: Illustrated are the three types of Coulomb crystals, which can be found in this work. (a) represents the pure Ca^+ Coulomb crystal, (b) a bi-component Coulomb crystal with ions lighter than Ca^+ and (c) a bi-component Coulomb crystal with ions heavier than Ca^+

Approximation of the trap depth for the radial and axial component is given by:

$$\text{for radial: } D_i = \frac{1}{2} m\omega_i r_0^2 \ (i = x,y) \tag{2.51}$$

$$\text{for axial: } D_z = \frac{1}{2} m\omega_z z_0^2 \tag{2.52}$$

The potential extends from trap center to r_0 for the radial and to z_0 for the axial dimension. Excess micromotion is a driven motion, caused by displacement of the ion from the rf axis by a static offset field $\mathbf{E}_{\mathrm{DC}}$. This results in an altered Mathieu equation with a solution of the lowest order in a_i and $q_i$given by [83]

$$r_i(t) \cong [r_{0i} + r_{1i}\cos(\omega_i t + \phi)]\left[1 + \frac{q_i}{2}\cos(\Omega t)\right] \tag{2.53}$$

where

$$r_{0i} \cong \frac{Q\mathbf{E_{DC}} \cdot \hat{r}_i}{m\omega_i^2} \tag{2.54}$$

Although it can not be reduced by laser cooling, excess micromotion fortunately can be reduced by the application of compensation static fields. Estimation of the kinetic energy by $\frac{1}{2} q_i r_{0i}$ reveal a significant influence even for small stray fields (i.e., patch potentials) [83].

Bi-component Coulomb crystals

The principle of Doppler laser cooling was covered in 2.2.2 and the experimental implementation is discussed in 3.1.3. In the case of ions, however, the trapping force is an electric potential. The benefit of this 3d trap is the damping of the motion of the ion by the application of a single cooling and repumper laser beam. This is possible due to the fact that all translational degrees of freedom are coupled together by the anharmonicities in the trapping potential and by the Coulomb interaction. Thus it is sufficient to remove momentum only from one direction. If the removed kinetic energy is sufficiently below the potential energy originating form their interaction, the ions form a ordered structure known as Coulomb crystals [84–86]. The phase transition to the crystalline structure occurs, when the plasma coupling parameter excceds $\Gamma \approx 150$ [87, 88].

$$\Gamma = \frac{E_{pot}}{E_{kin}} = \frac{Q^2}{4\pi\epsilon_0 r_\omega k_B T}, \tag{2.55}$$

where r_ω is the Wigner - Seitz radius giving the average distance between ions and ρ is the density of ions. A Ca^+ Coulomb crystal (see Figure 2.6a) can be used to sympathetically cool [89, 90] other non - laser coolable ion species, such as molecular ions (in this work specifically: N_2^+, O_2^+ and N_2H^+). The ion trap is adjusted to hold Ca^+ ions well, which results in a stronger confinement for lighter ions, thus aligning them more towards the center (see Figure 2.6b). Heavier ions will position themselves on outer shells around the Ca^+ ions (see Figure 2.6c).

3 Experiment

During the lifetime of this experiment, the experimental apparatus went through two major iterations. First, there was the work with the stationary atom cloud of Hall on atomic ion - neutral reactions [27, 30, 91] and on molecular ion - neutral reactions [4]. Second, there was the implementation of the dynamic hybrid trap by Ravi, Eberle *et al* [9, 92] with a more detailed description in Ref. [8]. After the experiment was built by Hall during his PhD (2009 - 2013), upgrades were done during 2014 - 2018 and are mostly summarised in [8]. Fundamental changes include a new ion trap, new atom sources (Ca, Rb), more stable mirror mounts and posts, mirrors with higher reflectivity, a new AOM (acousto optic modulator) setup and a new pulse sequencer for complex switching of the laser beams involved and an atom imaging setup with a fluorescence counter for velocity measurements. This chapter will discuss the experimental apparatus and the two main experimental modes, namely the stationary atom clouds and the shuttling atom clouds. It will briefly discuss the vacuum chamber and sum up the features of the hybrid trap. The laser system for cooling the atoms and the ions will be explained. The two experimental operations, stationary and shuttling, will then be introduced in more detail. For the stationary operation, the key parameters (atom cloud temperature, atom number estimation) will be described in section 3.2. The shuttling atom cloud will be discussed in section 3.3, whereas the optical setup and the pulse sequences will be outlined in 3.3.1 and the velocity determination of the atom cloud in 3.3.2. In section 3.4, the loading of atomic ions and molecular ions as well as the previous works of the reaction dynamics between molecular ions and a stationary atom cloud by Hall [4] and Eberle [8] will be reviewed.

3.1 Setup

The complete experimental setup spans over three different sections shown in Figure 3.1a. The laser table housing the two lasers for cooling ions and a more complex laser system for cooling and pushing the atom cloud (see Figure 3.3, 3.4a and 3.4b). The ionisation laser table with the setups of the 355 nm (third harmonic generator THG, Nd:YAG, Innolas, Spitlight 1500) Ca ionisation laser, which also pumps the dye laser systems for the ionisation of N_2 at 202 nm and for O_2 at 236 nm (see Figure 3.10) and the experiment chamber housing the hybrid trap setup.

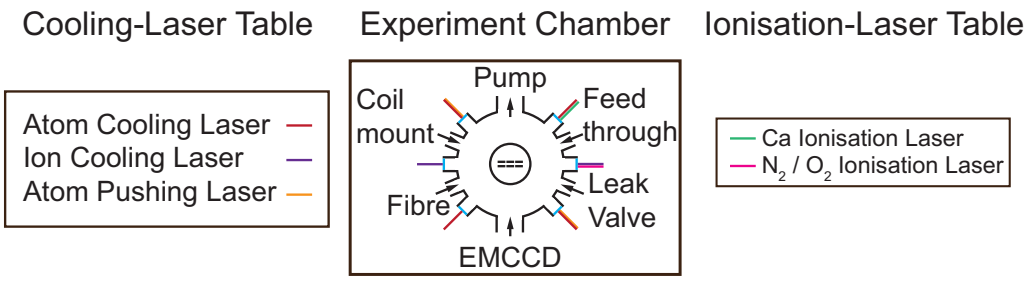

(a)

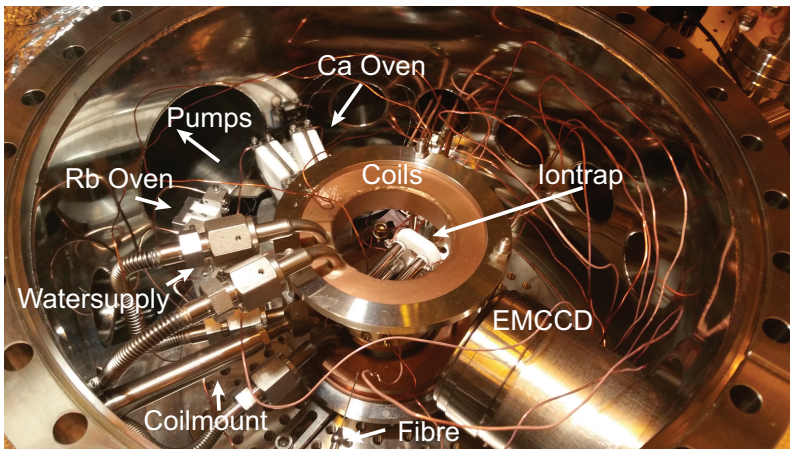

(b)

Figure 3.1: (a) A schematic setup of the hybrid trap. (b) A photograph of the open experiment chamber.

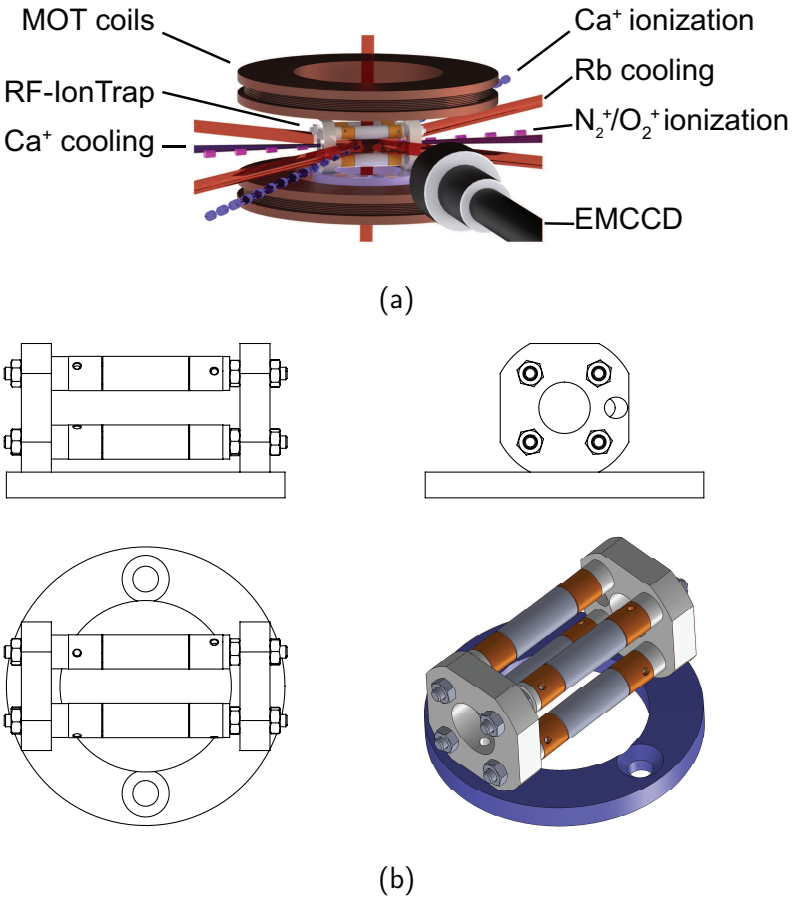

Figure 3.2: (a) A schematic setup of the hybrid trap. (b) A technical drawing of the ion trap designed by P. Knöpfel and built by the mechanical workshop of the University of Basel.

3.1.1 Vacuum chamber

The experiment chamber consists of a 350 mm stainless steel vessel housing a round breadboard at the bottom. It has five extended CF40 flanges at the bottom. Two for the electrical connections of the ovens (Ca,Rb) and the ion trap (one connector with 12 pins for the radiofrequency (rf) and the static voltage (DC)). One flange is for the residual gas analyser (Kurt J. Lesker AccuQuad RGA), one flange for the mechanical Ca oven shutter and a center one for the optical access of the $Z-$ axis MOT laser beam. Around the circumference are ten CF40 flanges and two CF150 flanges. Four of the CF40 flanges are for optical access of the X and Y axis laser beams for the atom cooling and two are for the optical access of the laser cooling of the ions along the trap axis of the ion trap. One is for the 3d translation stage of the fibre (see Figure 3.1b: 'Fibre') to indicate the ion position for laser alignment, one is for the 3d translation stage of the in vacuo anti - Helmholtz coils (see Figure 3.1b: 'Coilmount'), one for the leak valve to introduce various gases for molecular - ion generation and one for electrical connection of the anti - Helmholtz coils and temperature measurements of the ovens. On one of the CF150 flanges (see Figure 3.1b: 'Pumps'), a T shape extension is connected for a magnetically levitated turbo molecular pump (Oerlikon MAG W 600) and the titanium sublimation pump (Agilent Varian Tisub) and the other one has an insert with a glass window very close to the hybrid trap for the EMCCD camera setup (see Figure 3.1b: 'EMCCD'). The ion trap and the ovens are mounted inside the chamber on a round breadboard. The top lid of the chamber has a smaller CF150 window flange to allow access for the vertical MOT laser ($Z+$ axis) and the atom imaging system (see Figure 3.8). All flanges are sealed with copper gaskets. Under experimental conditions, the experiment chamber is at ultra high vacuum at around 7×10^{-11} mbar and with the ovens running at around 3×10^{-10} mbar. As discussed by Hall (Ref. [10], section 2.1), the background reaction with Ca^+ are orders of magnitude slower than the process of interest if the chamber pressure is kept below 5×10^{-10} mbar. To achieve this vacuum, the chamber is initially pump to roughly 5×10^{-8} mbar and then 'baked' (heated to 200 °C) for 10 days to reach 8×10^{-11} mbar. During the baking process, all seals on the ovens are opened and the ovens are degassed, to ensure a clean vacuum.

3.1.2 Facts about the hybrid trap

The hybrid trap consists of an ion trap with a superimposed magneto - optical trap (MOT). The ion trap is a standard linear Paul trap (see Figure 3.2b) with 12 segments made from stainless steel. Three segments in line are forming one rod (a more detailed description can be found in Ref. [8], appendix A.2). The radius of each rod is $r = 4$ mm and the distance from the trap center is $r_0 = 7.3$ mm to ensure optical access for the MOT laser beams. Each segment carries a mix of rf voltages with a frequency of $\Omega_{RF} = 3.2$ MHz and DC voltages. The rf and DC voltages are combined before the feedthrough by a mixing box (description in Ref. [10] in 2.2.2.). The DC signals are generated by a DAC card, which allows each segment

to be individually addressed. The eight endcap segments confine the ions in the axial direction, usually at 12 V and are half the length of the center segments. The four center segments adjust the position of the ions in the radial direction. The rf voltage is generated by a sinusoidal tube amplifier driven by a computer controlled DC power supply (FuG MCP650) with an adjustable voltage V_{0p} ranging from 0 V to 650 V. Two diagonally opposite located rods are in phase and the two other ones are 180° out of phase generating the rf confinement of the ions (see Figure 2.5). Standard operation voltages are: 145 V to remove heavy ions from the Coulomb crystal, 210 V during loading of Ca ions and 400 V during measurement. The magneto optical trap consists of a pair of anti - Helmholtz coils driven by a computer controlled DC power supply (Rhode and Schwarz HMP4040) at a fixed current of 3 A and six independent circular polarized laser beams. The coils are water - cooled in vacuo on a 3d translation stage for micrometer positioning precision and applying high magnetic field gradients of 18 G cm^{-1} (see a more detailed description in Ref. [10]). Both ovens are also computer controlled. The Rb oven runs at 4 A and the Ca oven at 8 A. The ovens themselves are fully described in Ref. [8] in appendix A.1. Lasers and optics for ion / atom trapping and cooling are discussed in the following subsection.

3.1.3 Lasers and optics (ions,atoms)

The theoretical aspects of the key concepts on ion / atom trapping and cooling were discussed in 2.2.4 and 2.2.3 respectively. The following subsections will discuss the optical setup necessary, starting at the external cavity diode laser up to the view port of the experiment chamber.

Ion laser cooling

To drive the cooling transitions discussed in Figure 2.2a two external cavity diode laser (Toptica DL100pro) at the wavelengths 397 nm and 866 nm are used. The 397 nm - laser setup is depicted in Figure 3.3 (left). The beam is partially split up with roughly 15 % used for locking to a wavemeter and the remaining 85 % for cooling of the ions. This cooling beam is passed through a double pass cat - eye AOM setup to switch the laser on and off according to the timing sequence presented in Figure 3.7. The AOM is driven by a VCO (voltage controlled oscillator) and an rf amplifier. The VCO is addressed by a pulse generator. After passing through a single - mode fibre to the experiment table, it is guided through a lens on a translation stage to be focused into the trap center. The measured power at the entry view port of the chamber is between 20 µW to 450 µW depending on the setting of the neutral density filter. The 866 nm laser is also locked to a wavemeter and shared between several experiments. It passes through a single mode fibre to the experiment table. On the table itself it is guided through a $\lambda/2$ waveplate and spatially overlap on a dichroic mirror with the 397 nm beampath. The measured power before the entry view port is < 1 mW and it is adjusted with a neutral density filter such that the intensity of this beam is double that of of the 397 nm laser. After passing through

the ion trap in axial direction, both lasers are retro-reflected. With the wavemeter lock, the usual stability of the laser lies in the femtometer region.

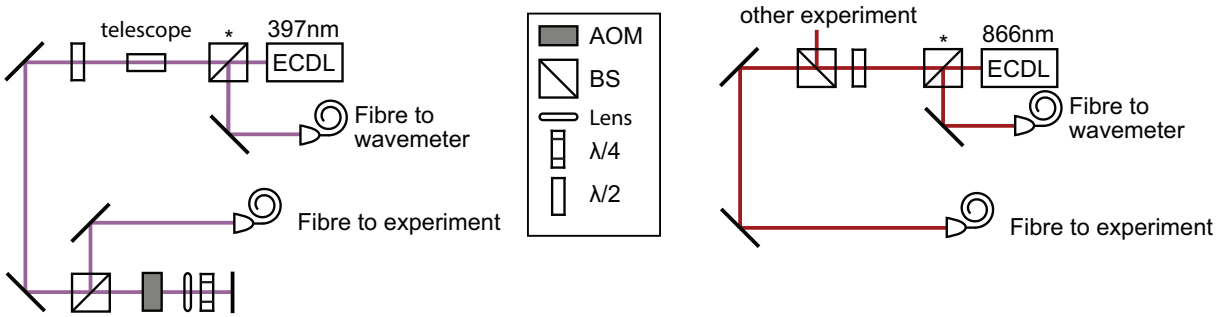

Figure 3.3: A schematic of the ion laser setup for cooling of the Ca ions based on an external cavity diode laser (ECDL). Left depicts the 397 nm cooling laser with a double pass cat-eye AOM (acousto optic modulator) configuration. The AOM is controlled by a pulse generator. Right illustrates the 866 nm repumper laser setup. Both lasers are locked to a Highfinesse WSU wavemeter with a feedback loop (see Appendix of Ref. [8]). Beamsplitter (BS) marked with * are non polarizing.

Atom cooling laser

The laser cooling of atoms in a magneto-optical trap is discussed in 2.2.3 and the necessary laser frequencies to achieve this are presented in Figure 2.2b. The first part of the laser setup is depicted in Figure 3.4a. It consists of a external-cavity diode laser (Toptica DL100), which is locked to a rubidium vapor cell. The locking is provided by the error signal generated from a Doppler-free saturation absorption spectroscopy fed into a lock-in regulator (Toptica LIR110), which then regulates the piezo controller (SC110) with a feed forward influence on the laser current. This keeps the laser narrow and stable, locked to a specific transition line for ^{87}Rb. It is the $^2S_{1/2}$ F=2 to $^2P_{3/2}$ F'=(2,3) crossover line and 212 MHz red detuned from cooling transition, locking the laser to 780.246 447 nm or 384.227 903 THz. About 35 mW of the laser power is amplified in a tapered amplifier (Toptica BoosTA) to 1.2 W to be coupled into a polarisation maintaining single mode fibre (PM-fibre). The fibre is for mode cleaning and transport of the light to the AOM setup, which will be discussed in more detail in 3.3.1. All laser beams are polarisation cleaned after the fibre out-coupler on the experiment table to ensure a correct circular polarisation as depicted in Figure 2.4a. The cooling detuning can be chosen by changing the VCO frequencies driving the AOMs. Power is adjusted by changing the VCO driver voltage, hence changing rf-amplitude for the AOMs. Usual experimental conditions measure a power of 4.5 mW for cooling along the X-axis ($XC+/-$) and 5.5 mW for cooling along the Y/Z-axis at the entry view ports of the experiment. $XP+/-$ are the atom pushing lasers along the X-axis and their maximum power to push the atoms is around 3.4 mW. (Remark: X and Y define the horizontal plane of the experiment. Z is the

orthogonal vertical axis).

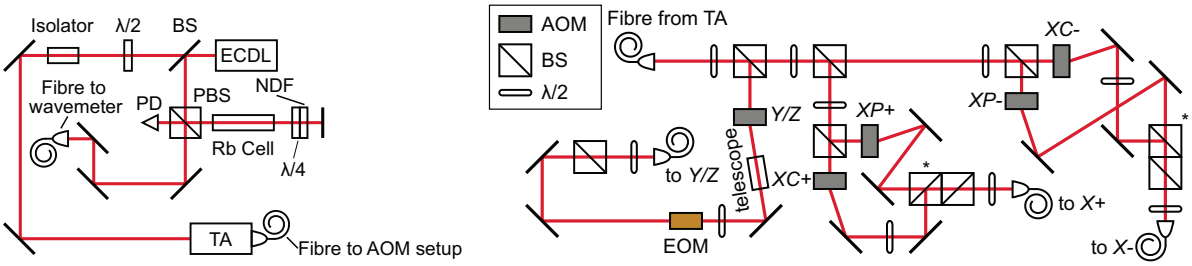

(a) (b)

Figure 3.4: (a) A schematic of the 780 nm - laser setup. For ^{87}Rb cooling and shuttling an external cavity diode laser (ECDL) generates light around 780.24 nm. Shortly after the ECDL, a small percentage of the light is split off and guided through a Doppler - free saturated absorption spectroscopy cell filled with a rubidium vapor to generate a locking signal for the lock - in regulator unit of the laser system, thus locking the laser to an absorption line of ^{87}Rb. The majority of the laser light is guided into a tapered amplifier, which generates roughly 1.2 W and is aligned into a fibre for mode cleaning and connecting to the AOM setup. (b) An overview of the laser setup of the shuttling atom cloud, which is used to split the single high power laser beam into the different laser beams for cooling and pushing the atoms. The AOMs are used to switch the laser beams on and off and shift the detuning of the cooling ($XC+/-$, Y, Z) and pushing ($XP+/-$) lasers accordingly. An EOM generates the repumper sidebands for the Y/Z - axis laser beams. The beam splitters (BS) are all polarising except for the ones marked with an asterisk (*). Half - wave plates balance the power distribution of the single laser beams. Before each fibre incoupler are the polarisation cleaner to ensure matched coupling into the polarisation maintaining fibres. The beampath is marked with a red line. (These figures were adapted with permission from Ref. [8])

3.2 Stationary atom cloud

One of the operational schemes of the experiment is the stationary atom cloud. The atoms are loaded into the trap and all cooling lasers are set to the same intensity for a central MOT. The off - center positions can be populated by unbalancing the intensity of the cooling lasers along the preferred axis (in this work by lowering the intensity of either $XC+$ or $XC-$). In the stationary mode, the atom cloud is overlapped with the Coulomb crystal and the off - center positions are checked to ensure flawless atom movement during the shuttling operation. The overlap with the Coulomb crystal is achieved by optimising the ion position, then loading an atom cloud, shining the 397 nm laser into the loaded atom cloud and optimising the atom position so the drop in the fluorescence of the atoms is maximised. The temperature of the atom cloud and the average density can be measured as explained in the following subsections.

3.2.1 Temperature measurement

Measuring the temperature of the atom cloud is essential. The initial temperature has a large influence on the kinetic-energy resolution during the collision experiments in this work. A theoretical discussion on the influence is presented in chapter 4. Hall [10] discussed measuring of the temperature of the ^{87}Rb ensemble in the MOT in section 2.3.5 of his thesis. He used the techniques following Ref. [93], which showed it is sufficient to turn off only one pair of the trap laser beams (i.e. X-axis trapping lasers), instead of the complete trap, to observe the ballistic expansion in this dimension. The expansion can be observed easily, since the atoms being constantly illuminated by the four remaining beams. The expansion follows Equation (3.1) at a rate which is characteristic of their initial temperature.

$$\omega_x^2(t) = \omega_x^2(0) + \left(\frac{k_b T}{m}\right) t^2, \tag{3.1}$$

$$\omega_r^2(t) = \left(\omega_x^2(t) + \omega_y^2(t)\right)/t. \tag{3.2}$$

Here, ω_x is the 1/e radius of the atom cloud in X direction. The EMCCD camera is aligned at a

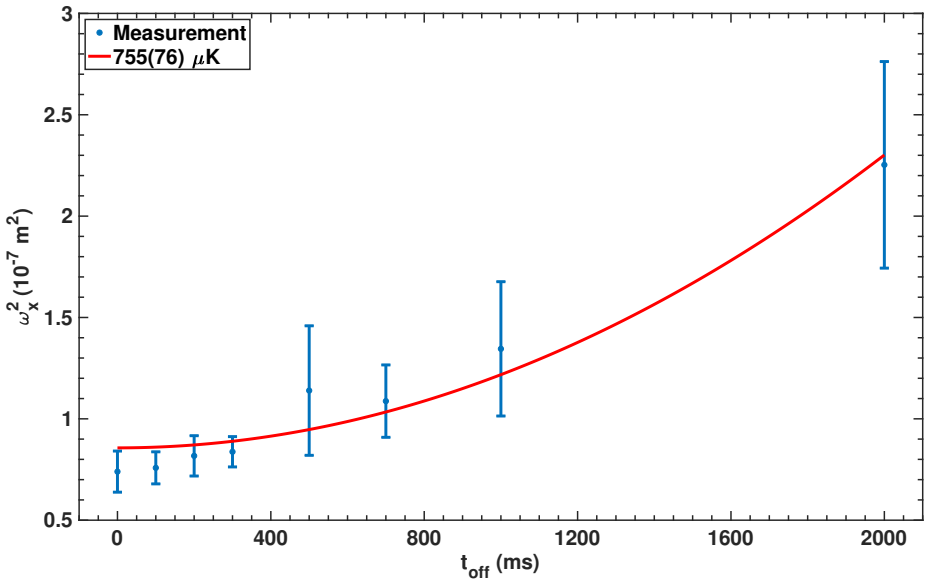

Figure 3.5: Dependence of the square of the atom cloud 1/e radius in the X direction ω_x on the expansion time t_{off}. The measured temperature of the atom cloud was found to be 755(76) μK.

45° angle to the X axis. Equation (3.2) relates the observed expansion on the EMCCD camera to the real expansion in X direction. ω_y is the radius of the cloud in Y direction. Expansion of the cloud in Y and Z was negligible during the 1d expansion, thus the temperature of the atoms can be calculated from the observed EMCCD image. In his thesis, Hall relied on a mechanical shutter for fast on / off switching of the laser beams. Due to the new AOM setup

in the beam path, the switching is done in a more precisely controlled way. With a switching time of the AOMs from 'beam on' to 'beam off' of about 1 µs, a variety of 'beam off' delays from 0.1 ms to 2 ms were possible. The EMCCD camera and AOMs were triggered from a PulseBlaster pulse generator for the experiment. The expansion pictures are analysed using a LabVIEW program (for further information see Ref. [8]). Figure 3.5 shows ω_x^2 in dependence of the expansion time t_{off}. The red line is the best fit to Equation (3.1) and yields a temperature for the atoms of 755(76) µK.

3.2.2 Average Density n_{avg}

In order to calculate the average density of the atom cloud, first an image of the stationary atom cloud is taken and followed by an additional image without the atom cloud for background subtraction. N_{ph} are the background - subtracted photon counts registered by the EMCCD camera. The scattering rate R is calculated following

$$R = \frac{\pi \Gamma S_0}{1 + S_0 + \left(\frac{2\delta}{\Gamma}\right)^2}, \tag{3.3}$$

where $\Gamma = 2\pi \cdot 6.0666(18)$ MHz (from Ref. [61]) is the natural linewidth of the ^{87}Rb cooling transition, δ is the laser detuning from resonance and S_0 is the saturation parameter. The saturation parameter is calculated according to $S_0 = I/I_s$, where I is the experimentally determined intensity of the cooling laser and $I_s = 9.2(17)\,\mathrm{mW\,cm^{-2}}$ is the saturation intensity according to [94]. The total imaging loss-factor L_T (Equation (3.4)) is factored into Equation (3.5), where $L_1 = 0.45(1)$ is the loss due to chopping, $L_2 = 0.0076(5)$ is the loss due to the finite solid angle of the imaging system, $L_3 = 0.93(2)$ is the loss at the view port, $L_4 = 0.098$ is the loss due to the camera sensitivity, $L_5 = 0.59(2)$ is the loss due to the bandpass filter, $L_6 = 0.84(2)$ is the loss due to the microscope optics and $L_7 = 0.484(5)$ is the loss due to the PMT beam splitter cube inside the microscope of the EMCCD setup. The atom number is calculated following Equation (3.5), where t_{exp} is the exposure time and G is the electron-multiplying gain of the camera.

$$L_T = L_1 \cdot L_2 \cdot L_3 \cdot L_4 \cdot L_5 \cdot L_6 \cdot L_7 \tag{3.4}$$

$$N = \frac{N_{ph}}{R \cdot t_{exp} \cdot L_T \cdot G} \tag{3.5}$$

Given it had an isotropic Gaussian density distribution $n(r)$ [95]:

$$n(r) = \frac{N}{\pi^{3/2}\omega^3} \exp\left\{-r^2/\omega^2\right\}, \tag{3.6}$$

the average density can be calculated by integrating over the product of the probability of an atom being at a distance r and the density at a distance r. With ω being the 1/e radius of the

atom cloud obtained from 2D fits to images of the atom cloud and knowing the atom number N, the average density n_{avg} for a stationary atom cloud is calculated as

$$n_{\text{avg}} = \int \frac{n(r)}{N} n(r) dV = \frac{N}{2\sqrt{2}\pi^{3/2}\omega^3}. \tag{3.7}$$

Typical average densities during the experiment for the stationary atom cloud are $n_{\text{avg,stat}} = 1.2(4) \times 10^8\,\text{cm}^{-3}$ atoms and for the dark shuttling atom cloud $n_{\text{avg,shut}} = 2.8(2) \times 10^8\,\text{cm}^{-3}$ atoms. Their respective uncertainties are as follows and are in the range of 5 % to 15 %:

$$\sigma_{L_T} = \sqrt{\sum_{n=1}^{7} \left(\frac{L_T}{L_n}\right)^2 \sigma_{L_n}^2} \tag{3.8}$$

$$\sigma_R = \sqrt{\left(\frac{\pi\Gamma^3(\Gamma^2+4\delta^2)}{(4\delta^2+\Gamma^2(S_0+1))^2}\right)^2 \sigma_{S_0}^2 + \left(\frac{8\pi\cdot S_0\cdot\delta}{\Gamma\left(1+S_0+(2\delta/\Gamma)^2\right)^2}\right)^2 \sigma_\delta^2} \tag{3.9}$$

$$\sigma_N = \sqrt{\left(\frac{N_{\text{ph}}}{R^2\cdot t_{\text{exp}}\cdot L\cdot G}\right)^2 \sigma_R^2 + \left(\frac{N_{\text{ph}}}{R\cdot t_{\text{exp}}\cdot L^2\cdot G}\right)^2 \sigma_L^2 + \left(\frac{1}{R\cdot t_{\text{exp}}\cdot L\cdot G}\right)^2 \sigma_{N_{\text{ph}}}^2} \tag{3.10}$$

$$\sigma_{n_{\text{avg}}} = \sqrt{\left(\frac{1}{2\sqrt{2}\pi^{3/2}\omega^3}\right)^2 \sigma_N^2 + \left(\frac{3N}{2\sqrt{2}\pi^{3/2}\omega^4}\right)^2 \sigma_\omega^2} \tag{3.11}$$

3.3 Shuttling atom cloud

Shuttling an atom cloud requires a complex switching sequence to move the atoms between two predefined off-center positions through the center position previously established in the stationary mode of the experiment. This operational mode of the experiment is illustrated in Figure 3.6. First the atom cloud starts in one off-center position, where it is kept and cooled by radiation imbalance on the shuttling axis X (Figure 3.6a). In the next step, the X axis cooling lasers are turned off and the on-resonance push beam, i.e., $XP+$ is turned on for a predetermined amount of time (Figure 3.6b). Subsequently to turning off $XP+$, the atom cloud enters a predefined free flight while passing the center position and is afterwards recaptured in the second off-center position by inversion of the radiation imbalance on the X axis (Figure 3.6c). The atom cloud is cooled again and the process is reversed (Figure 3.6d, 3.6e). An additional operational mode allows the atoms to relax into their ground state during the free flight phase by turning the Y/Z confinement laser beams off during transit

3.3.1 Optics, optical elements and pulse sequence generation

The laser beam path for this sequence is illustrated in Figure 3.4b and the switching sequences of the different laser beams involved are presented in Figure 3.7. The laser beams are split up into different pathways. The Y/Z axis of the experiment is one path. First, the beam passes

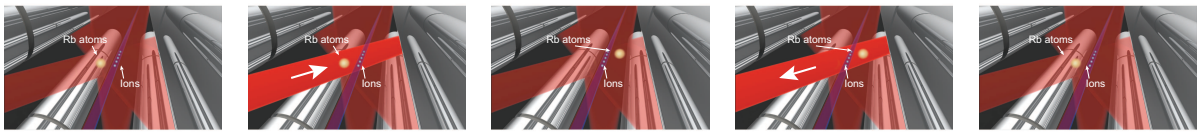

(a) (b) (c) (d) (e)

Figure 3.6: Schematic of atom shuttling. (a) Atom cloud in an off-center position. b) Cooling lasers on shuttling axis are turned off and on-resonant laser beam for pushing the atom cloud is activated. (c) Atom cloud gets recaptured and cooled in second off-center position. (d) Reversed pushing of the atom cloud. (e) Recapturing and cooling in the initial off-center position. This completes one shuttling cycle.

through an AOM to switch the laser beam on and off and adjust the cooling detuning. Second, sidebands are generated by passing through an EOM (Newport visible phase modulator 4851) with a frequency $f_{\mathrm{EOM}} = 6.568\,\mathrm{GHz}$ for repumping the population from hyperfine states of Rb not accessed by the cooling laser. Afterwards, the polarisation is cleaned, matched to the polarisation axis of the fibre and coupled into a fibre, which guides the beam to the experiment. At the experiment, the single fibre is split 4 ways with polarisation-maintaining fibre-splitters (Thorlabs, PFC780A) to generate four independent laser beams ($Y+$, $Y-$, $Z+$, $Z-$). The X axis has two different paths $X+$ and $X-$. Both of them are split further into $XC+/XP+$ and $XC-/XP-$. $XC+/-$ pass through an AOM which shifts their respective frequencies according to the set cooling detuning and $XP+/-$ pass through different AOMs to ensure an on-resonance frequency. $XC+$ and $XP+$ as well as $XC-$ and $XP-$ are then polarisation cleaned, matched to the polarisation axis of the fibre and combined into one PM-fibre each and guided to their respective positions on the experimental table. The pulse generator used for triggering the pulse sequences is a SpinCore PulseBlaster PB24-100-4k. It has 24 freely programmable channels and is used to address the different rf electronics to drive the AOM setup. This is described in detail in the work of Eberle [8] in chapter 3. The major difference in this work, however, is a change in the timing sequence. Figure 3.7 shows the time sequence for all laser beams involved. The X axis cooling laser for the atom cloud have three different settings, namely high intensity, low intensity and off. All other laser beams involved are only turned either on or off. Starting at the left of Figure 3.7, cooling laser $XC+$ is set to high and $XC-$ is set to low, laser Y/Z is on and the ion cooling laser is off, to move the atom cloud in the $X-$ off-center position. During time T_{P}, $XP-$ and Y/Z are on and all others are off, pushing the atom cloud from the off-center position in the direction of the $X+$ off-center position. Subsequently, during time T_{F} all lasers are off except Y/Z, which can be switched off for a period T_{D}. During this phase the atoms are in free flight. During sequence T_{H}, atoms are held in a off-center position. Atom and ion cooling alternates with adjustable timings and depending on the atom cloud position (off-center $X+/X-$ or center) with different intensities for $XC+$ or $XC-$. The last part of the Figure, after sT_{H}, shows the reversed pushing sequence.

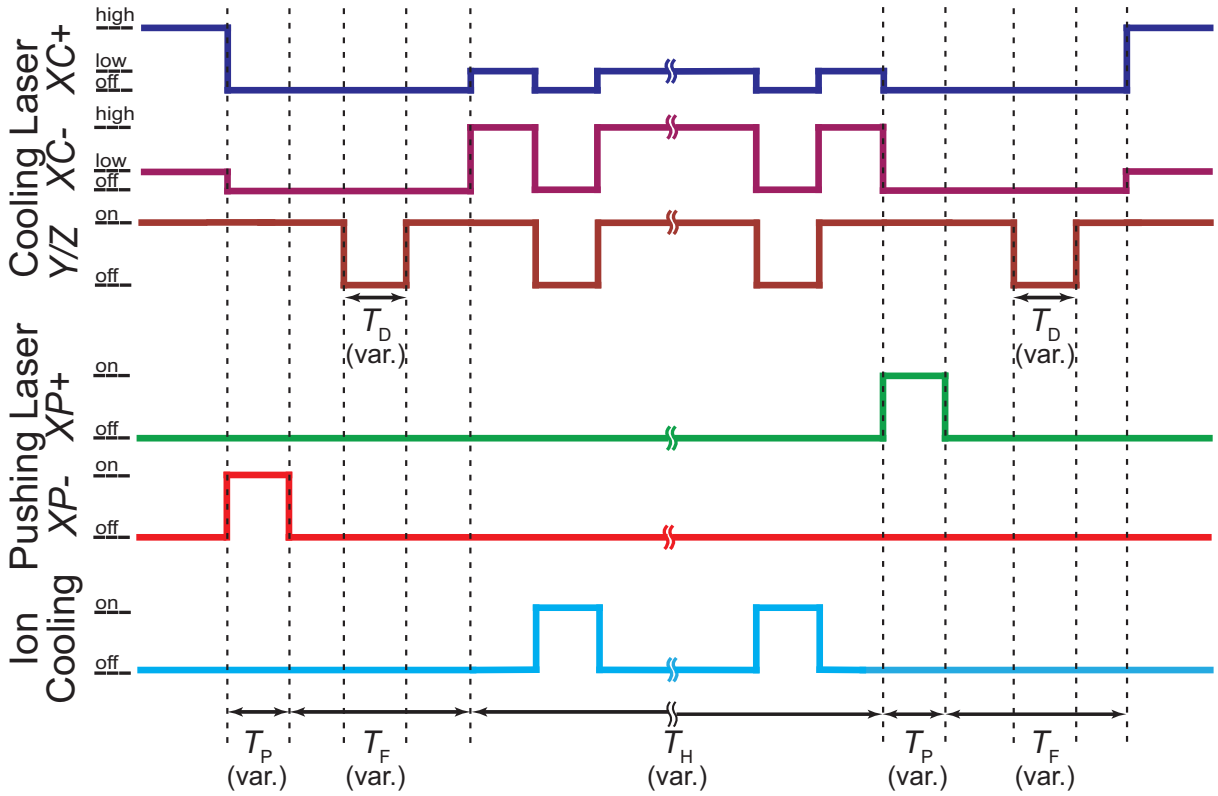

Figure 3.7: Timing sequence for the laser pulses in the experiment. T_P is the on-resonance push-laser light time. T_F is the free-flight time while the atoms pass slit 1, the ion interaction region and slit 2 (see Figure 3.8). T_H is the off-center re-cooling time, while the atoms are being held in an off-center position. T_D is the time, while the Y/Z axis confinement is turned off. All time periods can be freely varied. Typical experimental settings are $T_P = 175\,\mu s$, $T_F = 500\,\mu s$, $T_H = 80\,ms$ and $T_D = 0\,\mu s$ with Y/Z cooling or $T_D = 500\,\mu s$ without Y/Z cooling.

3.3.2 Velocity determination

Figure 3.8a illustrates the imaging setup for the atoms. It is a relay lens system, capable of imaging the atom cloud on a complementary metal-oxide semiconductor (CMOS) camera (Thorlabs DCC 1545M) and collecting fluorescence on a photomultiplier tube (PMT, Hamamatsu H11461-03). The image plane of the atom position is labelled 'I'. To measure the velocity of the atom cloud with the PMT, a double slit is inserted in the imaging system at position 'I_A' to block the atom cloud fluorescence from the PMT except for the two slits. While the atoms pass the slits, a fluorescence trace is recorded on the oscilloscope and sent to a computer. The slits have a slit width of 100 µm at a distance of 1 mm. Due to imperfections in the imaging system, a magnification factor of 0.955(31) was determined. Figure 3.8b shows an image of the CMOS camera of the moving atom cloud. Because of the long exposure time of the camera system (100 ms) and the shuttling period of 80 ms, atoms at both off-center position are visible. The green bars indicate the slit positions when inserted into the imaging system. Under normal experimental conditions the distance between both atom cloud positions is 2 mm.

3.3.3 Inferring the kinetic energy, the velocity, the kinetic energy spread and the velocity spread of the shuttling Rb atoms from simulations

Measuring the velocity of the flying atom cloud yields the experimentally achievable kinetic-energy E_{kin} available for reaction measurements. Another key characteristic of the dynamic atom cloud is the kinetic-energy resolution ΔE_{kin}. This information is buried in the velocity measurement due to the convolution of the finite widths of the two slits and the Gaussian spatial distribution of the atom cloud. So extracting this property of the atom cloud needs a different approach. Inferring the kinetic-energy and the kinetic-energy resolution from a theoretical Monte Carlo trajectory simulation of the moving atom cloud provides this information which can be directly compared with the experimental measurements. In chapter 4 of this work, the simulation of a moving atom cloud will be discussed in more detail. For now it is sufficient to understand that the temperature, off-center starting positions and settings like cooling laser intensity / detuning, $1/e^2$ radius of the laser beams, pushing-laser intensity / detuning and the magnetic-field gradient were experimentally determined and used in the simulations. Boundary conditions to describe the double slit and photon counting were implemented to match further experimental parameters. Figure 3.9a compares the time-resolved fluorescence of the atom cloud passing underneath the slits from a (red dashed line) with an experiment (solid green line). Both signals are inverted. The simulated curve has been normalized to the height of the first peak of the experimental spectrum. The simulation did not use any freely adjustable parameter except for a global scaling factor. The agreement is

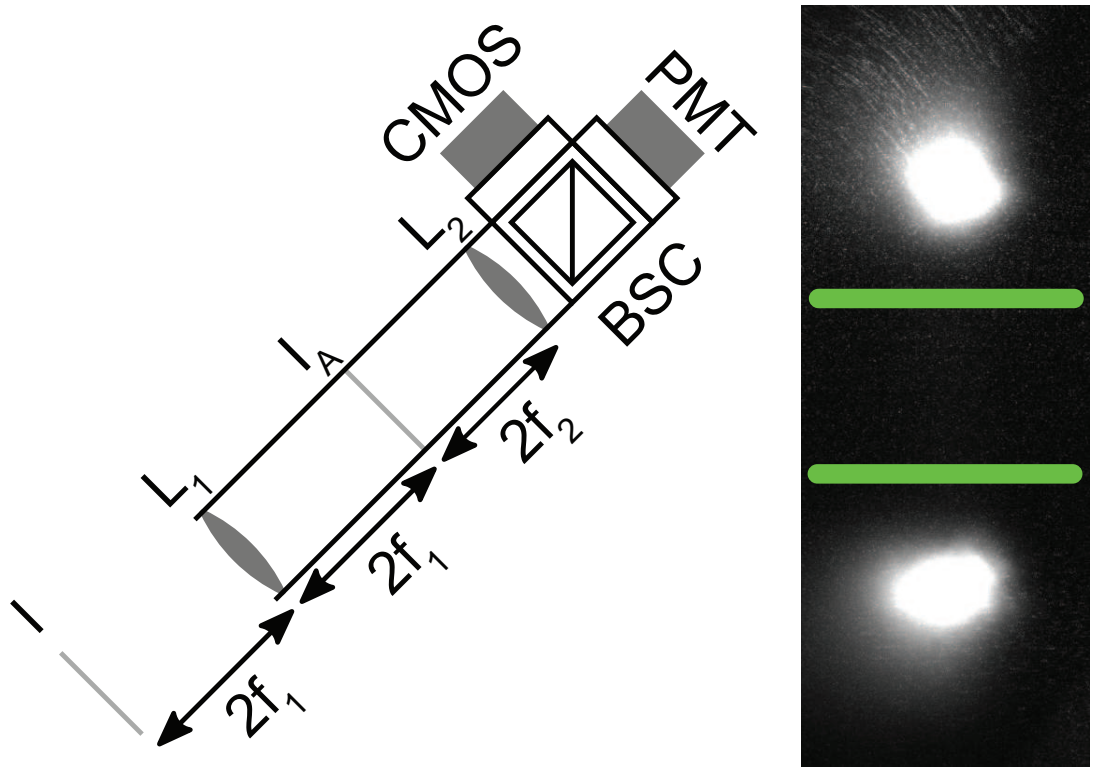

(a) (b)

Figure 3.8: (a) Schematic of the atom imaging setup. It consists of a relay lens system to image the atoms 1:1 on a CMOS camera and collect the fluorescence at a photomultiplier-tube (PMT) using a beam splitter cube (BSC). I is the image plane describing the atom position. At position I_A, a second image plane is created with L_1, which is then further relayed with L_2. A double-slit aperture to measure time-of-flight profiles is inserted at position I_A (see text for details). (b) is an image of the Rb atom fluorescence taken with the CMOS camera. The two solid green lines illustrate the position of the double slit. (These figures were adapted with permission from Ref. [8]).

considered to be good. Figure 3.9b shows experimental kinetic energies of the moving atom cloud, calculated from the ToF spectra in both, the forward and backward directions (green and blue dots, respectively). The data depicted are 10 measurements per point and ranges from $E_{\mathrm{kin}}/k_{\mathrm{B}}$ =40 mK to 120 mK. The errorbars extend to the size of the symbols and indicate one standard deviation of one series of ten measurements. This illustrates the excellent reproducibility and stability of the experiment. Tuning of the kinetic energies is achieved by changing the power of the push laser beams. Slight optical imperfections between $X+$ and $X-$ lead to differences in their intensities at the position of the atom cloud and need to be adjusted to gain similar kinetic-energies in both push directions. The red crosses show the mean kinetic-energies determined from the simulated ToF spectra. The good agreement between the simulation and the actual measurements further support the validity of the computational approach. Computed kinetic energies and kinetic energy resolutions are found and discussed in detail in Figures 4.5a, 4.6a, 4.7a and 4.8a for simulations with transversally cooled atoms and in Figures 4.5b, 4.6b, 4.7b and 4.8b for the free-flying atoms.

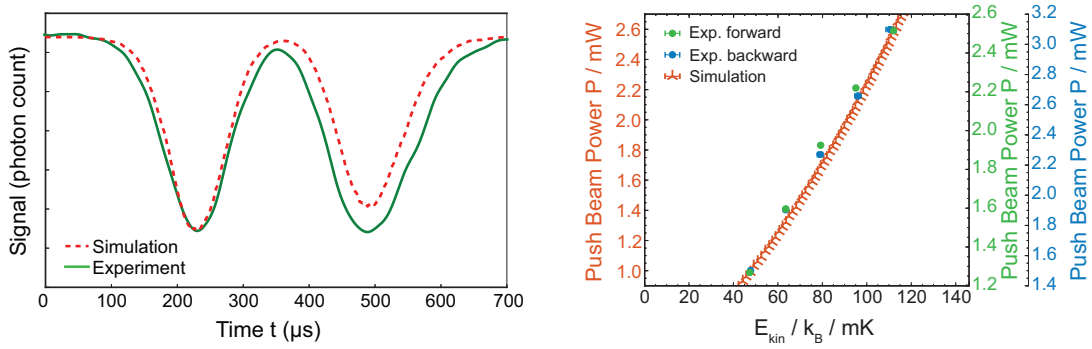

(a) (b)

Figure 3.9: (a) Comparison of a simulated time-of-flight profile of a shuttling atom cloud (dashed red line) to the experimentally measured time-of-flight profile (solid green line). The position of the minima of the ToF profiles and their corresponding width of the profiles fit together well. The loss of signal in the simulation is due to atoms not being constantly replenished from background vapor as happens in the experiment by a Rb atom dispenser. (b) Comparison of the measured kinetic energies E_{kin} in dependence of the power of the laser beams used to push the atoms. The green (forward shuttling direction) and blue dots (backward shuttling direction) are the experimentally measured points and the red crosses illustrate the simulated kinetic energies.

3.4 Atomic and molecular ions

In the following subsections the loading and trapping of all included atomic and molecular ions is discussed. Figure 3.10 depicts the laser setup for ionisation of the atomic and molecular

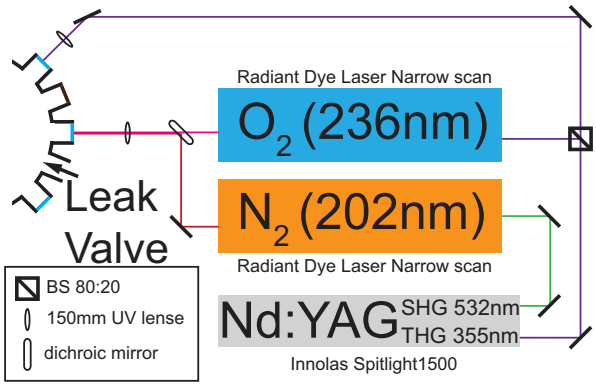

Figure 3.10: The ioinisation laser setup used to produce atomic and molecular ions consists of an Innolas Spitlight 1500 Nd:YAG laser with a frequency-doubling unit (SHG) and a frequency-tripling unit (THG) to generate 532 nm and 355 nm radiation respectively. The SHG output is used to pump a dye laser for N_2 ionisation. It is operated with a dye mixture lasing at 607 nm and frequency tripled to yield 202 nm. The THG output is split into two beams by a beam splitter, with 80 % of the intensity used for pumping a dye laser for the O_2 ionisation and 20 % for Ca ionisation. The dye laser operates at 462 nm and is frequency doubled to 236 nm. Both dye laser beams are spatially overlapped on a dichroic mirror and guided into the chamber through the trap. The 355 nm has a different path. Back reflections from the viewport windows are aligned onto the incoming beam to suppress stray light in t(he chamber.

ions. The dye laser systems contained an ethanolic solution of Rhodamin-B / Rhodamin-101 in case of N_2 and Coumarin-1 for O_2. The dye reservoirs are air-cooled by electric fans to prolong the lifetime of the dye.

3.4.1 Loading and trapping of Ca^+

From an atomic beam of Ca emanated by a resistively heated oven, $^{40}Ca^+$ ions were loaded into the trap by non-resonant multiphoton photoionisation at 355 nm ($\approx$ 15 mJ per pulse at 10 Hz, see Figure 3.10) and subsequently laser cooled forming a Coulomb Crystal of spatially localized ions [21]. With a first ionisation energy of 6.1 eV, two photons of 355 nm (3.84 eV) are required. The Ca atom source is a tube-shaped oven from Alfavakuo. It consists of a metal tube suitable for ultra high vacuum. The Ca is stored under argon atmosphere and the oven is shipped sealed with a pressed indium seal. The indium seal is opened during bake out and the oven shutter prevents the indium from sputtering on the skimmer and subsequently on the trap. In front of the oven sits a small slit skimmer to shield the linear Paul trap electrodes from Ca coating, hence preventing patch potentials. The oven-design is discussed in the appendix of Eberle [8].

3.4.2 Loading, trapping of molecular ions

Laser cooling of molecular ions is not very easily achieved. Molecular ions have many degrees of freedom and a complex energy - level structure. This means most of them cannot be cooled by Doppler laser cooling except if the molecule in question has nearly diagonal Franck - Condon factors and strong optical forces resulting from the short excited - state radiative lifetime as seen in the transverse laser cooling of SrF [13, 64]. A more versatile method to translationally cool molecular ions is sympathetic cooling with simultaneously trapped laser - cooled atomic ions [21], in this work a Ca^+ Coulomb crystal. Molecular ions were formed in the rf ion trap by ionisation from room temperature background gas at a background pressure of 1×10^{-8} mbar, using a $[2 + 1]$ resonance-enhanced multi photon-ionization (REMPI) via the Q branch $X^1\Sigma_g^+ \rightarrow a''\Sigma_g^+(\nu' = 0)$ transition in $^{28}N_2$ and via the $\Phi^3(\nu = 1)$ Rydberg state for $^{32}O_2$. After the ionisation, the background pressure was kept at 1×10^{-8} mbar for 30 seconds to equilibrate the rotational levels population by collisions and quench the vibrational level populations to the ground state. The ionisation laser setup is depicted in Figure 3.10.

4 Simulation of shuttling atom clouds

In the PhD thesis of Eberle [8], the experimental work on the dynamic ion-atom hybrid trap with the shuttling atom cloud was described extensively and summarized in this work in chapter 3, section 3.3. However, in his thesis the simulation of this process was only discussed briefly. The first systematic simulation study on shuttling atom clouds in the trap used in this work was undertaken by von Planta [96]. In his thesis, the theoretical background for the simulations is discussed, as well as a description of the program codes for first numerical simulations to be compared to the experiments, is presented. Von Planta [96] suggests the possibility to further narrow the kinetic-energy spreads with advanced switching schemes of the pushing and cooling lasers involved. His work presents a fundamental base for a more precise investigation. To help with the analysis of the initial approach to the simulations, the changes in the code will be reviewed first (section 4.1) and complemented with an extensive discussion on the explored parameter space and the influence on either moving atoms with transversal (Y/Z-axis) cooling, namely bright atom simulations, or without transversal cooling, namely dark atom simulation. To better understand the difference between bright-atom and dark-atom shuttling simulations, Figure 3.7 illustrates the laser timing sequence of the experiment. Details on this figure are discussed in chapter 3 under subsection 3.3.1. To compare the results from the bright atom simulation with the dark atom simulation the variable timings of Figure 3.7 for T_P, T_F and T_H were kept identical and only T_D was changed from $0\,\mu s$ to $500\,\mu s$.

4.1 Description of the approach

Calculating the behaviour of a travelling ultra-cold atom cloud was accomplished with Monte-Carlo Trajectory simulations. The computational approach consists of two major program parts, namely the equilibration code and the shuttling code. These two codes describe the equilibration of a ultra-cold atom cloud in an off-center position and the shuttling of the atoms from the first off-center position through the interaction region with the ions until a boundary condition (e.g. all atoms passed the second slit, see Figure 4.1) is met. Figure 4.1 is a visualization of an actual computational run at different time steps. Slit 1 and Slit 2 represent the boundary conditions in the simulation. The illustrated Coulomb crystal in blue is not part

of the simulation and only serves as and indicator for the interaction region. Both programs were initially written in Fortran 77 and were transferred to Fortran 95 to make use of dynamically allocatable memory. This helps to more freely define the memory for the variables used in the calculations. Generally, those programs can be run on any computer, given that it has a Fortran 95 compiler such as gfortran or ifort, but to minimise the calculation time they were done on the studix-cluster at the University of Basel. The cluster consists of a master with 8 nodes. The master runs on a 12 core Intel Xeon E5-2650v4 2.2 GHz, 4x8 GB 2133 MHz RAM and 3 WD 1 TB 7200 rpm HDD. The 8 nodes run on two 8 core Intel Xeon E5-2650v2 2.6 GHz, 8x4 GB 1600 MHz RAM and 1 Intel 535 SSD with 120 GB. The master and the nodes are connected with a Netgear GS748T-500US. The code is written for serial computation. The equilibration code runs for about 10 min. The initially equilibrated atom cloud is saved to a separate file and can be reused for multiple instances of the shuttling code. One simulation run of the shuttling code takes about 4 h to complete. Since multiple shuttling simulations can be sent to the cluster, there is no need for parallelisation.

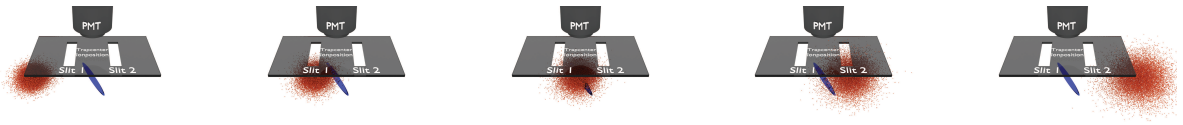

(a) (b) (c) (d) (e)

Figure 4.1: Rendering of the actual simulation process. (a) Starting point of the simulation with the initial equilibrated atom cloud. (b) Passing of the first slit and collection of the simulated fluorescence of the single atoms at the simulated PMT for the time-of-flight profile. (c) Interaction region of the atom cloud with the ion crystal. Collection of all position and velocity of each atom in the simulation for further calculating the kinetic energy and the kinetic-energy distribution. (d) Passing of the second slit and collection of the simulated fluorescence of the single atoms at the simulated PMT for the time-of-flight profile. (e) Stopping point of the simulation.

4.1.1 Equilibration

In the equilibration code, a model ultra-cold atom cloud is generated under conditions comparable to the experiment by utilising measured parameters from the experiment, e.g., the laser beam intensity, cooling laser detuning, cooling laser $1/e^2$ beam radius and magnetic-field gradient. The calculation starts by giving each atom an initial velocity, acceleration and position following a Maxwell distribution and in the first time step a new velocity and position is calculated. Then the time step is increased by $\Delta t = 1\,\mu s$ and the scattering force and the additional heating force is calculated. The scattering force acting on each atom is calculated with a Velocity Verlet integration algorithm (discussed in more detail in subsection 4.1.3) and determines the scattering rate in each spatial direction considering the Zeeman shift and the

laser polarisation for every laser beams individually. From the scattering rate, the total number of photons scattered per time step is determined by applying a Poisson distribution function on the product of the time step accumulated with the absolute photon count for each individual direction and then summing them up. This total photon count is then randomly distributed and implemented as momentum kicks, from which the acceleration of each atom can be calculated. Since the density of the atom cloud is very low, in the range of $1 \times 10^8\,\mathrm{cm}^{-3}$ to $1 \times 10^9\,\mathrm{cm}^{-3}$, the atom - atom interaction can be neglected. To adjust the temperature of the atom cloud, a random heating force is implemented. After calculation of the random heating force and the scattering force, the acquired parameters are then used to calculate the initial velocity for the next time step. This code runs for a predefined number of steps and in the end a final spatial and velocity distribution is achieved, giving a terminal temperature and overall position of the ensemble.

4.1.2 Shuttling

The shuttling code makes use of the equilibrated ultra - cold atom cloud of the previous subsection 4.1.1 and recreates the experimental mechanism of shuttling the atom cloud. The program loads the initial spatial and velocity distribution of the equilibrated atom cloud. Afterwards the shuttling sequence is started by switching off the x - axis cooling lasers and applying an on - resonance Gaussian laser beam (pushing) at a pre - defined intensity and time T_P in the simulation. The positions and velocities of each individual atom per time step is calculated making use of the 4^{th} order Runga - Kutta integration method. This integration method is an improved Euler method and evaluates the scattering force four times per time step, with the parameters for each evaluation depending on the results of the former. This gives a weighted incremental step for each evaluation and finally results in new velocity and position for each atom. These new parameters are the initial velocity and position for the new integration in the next time step. In the experiment, a double slit is implemented into the imaging system to measure the velocity of the atom by fluorescence collection of the passing atom cloud with a PMT. To incorporate this into the simulation, two boundary conditions according to the slit positions are implemented in the simulation, as long as the atom position is located inside these confines its photon count is accumulated. This information is then saved into a file which can then be used to illustrate the photon count dependent on the travel time. If all atoms passed the second slit completely and no photon count is registered anymore, the simulation is stopped. The whole simulation is repeated in an adjustable step size over the available laser intensities for the on - resonant Gaussian beams. In addition to the photon count per time step, the kinetic - energy distribution ΔE_kin, the velocity distribution Δv and the three dimensional cartesian coordinates $\{x, y, z\}$ with their associated velocities $\{v_x, v_y, v_z\}$ are saved to separate files. With those files, the kinetic - energy distribution of the atoms can be calculated and the behaviour of the atoms during the process can be visualized (see figures 4.1). A

comparison of the simulated time-of-flight result to the experimental time-of-flight trace was presented in subsection 3.3.3 in Figure 3.9a. Results of the varying ΔE_{kin} depending on the variation of different parameters will be discussed in subsection 4.2.

4.1.3 Integration algorithm

In the initial code of the equilibration program, the explicit Euler method was used as an integration method. For the purpose of the previous work [96], it was deemed sufficient. During the further development of the code and the implementation of new boundary conditions to reconstruct the double slit measurement of the experiment for the time-of-flight profiles in the simulation, it was discovered that the initial equilibrated atom cloud size does not match the expected cloud size of the experiment. In fact, it produced such a malformed atom cloud that it already initiated photon counting in the first step of the shuttling simulation. To avoid this miscalculation, first it is important to understand why this error occurred. In the following paragraphs, the theoretical background for the equilibration process is set, the explicit Euler method will be discussed and the Velocity Verlet algorithm is presented as a solution.

Newtons equation of motion (EOM) of classical mechanics

In a Hamiltonian system of particles, the Lagrangian equation of motion is given by

$$\frac{d}{dt}\left(\frac{\partial L}{\partial \dot{q}_i}\right) - \frac{\partial L}{\partial q_i} = 0, \tag{4.1}$$

where q_i are the generalized coordinates and $\partial \dot{q}_i$ the velocities associated. The Lagrange function in terms of the kinetic energy E_{kin} and potential V_{pot} is given by:

$$L = E_{\text{kin}} - V_{\text{pot}}. \tag{4.2}$$

In Cartesian coordinates $\boldsymbol{r}_i$, using the following definitions of the kinetic energy and the forces $\mathbf{f}_i$

$$E_{\text{kin}} = \frac{1}{2}\sum_i m_i \dot{\boldsymbol{r}}_i^2 \tag{4.3}$$

$$\mathbf{f}_i = -\nabla_{\boldsymbol{r}_i} V_{\text{pot}}, \tag{4.4}$$

the Euler-Lagrange Equation (4.1) returns Newton's equation of motion:

$$m_i \ddot{\boldsymbol{r}}_i - \mathbf{f}_i = 0. \tag{4.5}$$

A Hamiltonian for the system can be defined by the introduction of generalized momenta p_i following

$$p_i = \frac{\partial L}{\partial \dot{q}_i} \tag{4.6}$$

$$H = \sum_i \dot{q}_i\, p_i - L. \tag{4.7}$$

With a velocity and time independent potential, the Hamiltonian is equal to the energy and in Cartesian coordinates it follows

$$\dot{\boldsymbol{r}}_i = \frac{\boldsymbol{p}_i}{m_i}, \tag{4.8}$$

$$\dot{\boldsymbol{p}}_i = \mathbf{f}_i. \tag{4.9}$$

Since the explicit Euler method is a numerical method to solve first-order differential equations, it will be used to solve Equation (4.8). The Velocity Verlet method, on the other hand, works with second-order differential equations, hence Equation (4.5). To utilize the integration schemes, the EOMs have to be discretised. This can be obtained by Taylor expansion:

$$\boldsymbol{r}_i(t+\Delta t) = \boldsymbol{r}_i(t) + \Delta t\,\mathbf{v}_i(t) + \frac{\Delta t^2}{2m_i}\mathbf{f}_i(t) + \frac{\Delta t^3}{3!}\dddot{\boldsymbol{r}}_i(t) + \mathcal{O}(\Delta t^4), \tag{4.10}$$

$$\mathbf{v}_i(t+\Delta t) = \mathbf{v}_i(t) + \frac{\Delta t}{m_i}\mathbf{f}_i(t) + \frac{\Delta t^2}{2}\ddot{\mathbf{v}}_i(t) + \frac{\Delta t^3}{3!}\dddot{\mathbf{v}}_i(t) + \mathcal{O}(\Delta t^4). \tag{4.11}$$

Explicit Euler method

The trajectories can be calculated based on Equations (4.10) and (4.11) according to

$$\boldsymbol{r}_i(t+\Delta t) = \boldsymbol{r}_i(t) + \Delta t\,\mathbf{v}_i + \frac{\Delta t^2}{2m_i}\mathbf{f}_i(t) + \mathcal{O}(\Delta t^3), \tag{4.12}$$

$$\mathbf{v}_i(t+\Delta t) = \mathbf{v}_i(t) + \frac{\Delta t}{m_i}\mathbf{f}_i(t) + \mathcal{O}(\Delta t^2), \tag{4.13}$$

with higher order terms ($\mathcal{O}(\Delta t^3)$ and $\mathcal{O}(\Delta t^2)$) being neglected. The explicit Euler method is called a first order method and is only accurate when the rate of change is constant over the integration time step. However, in the equilibration of an atom cloud acceleration slows down as the atoms are getting colder and achieve equilibrium. This behaviour is qualitatively comparable to a damped harmonic oscillator. Hairer *et al.* [97] discusses the explicit Euler method for the cases of a mathematic pendulum and the Kepler problem. In both numerical integrations, the explicit Euler method spirals outwards, meaning the energy in the system increases, as illustrated in Figures 4.2 and 4.3. Even adding a damping force to the Hamiltonian does not yield the desired result. The disadvantage of the explicit Euler method lies in the non-symplecticity of the method. Symplectic methods conserve the total energy (the Hamiltonian) of the conservative simulation problem. The Euler algorithm unfortunately builds up a small numerical drift over a long period of integration and hence position and velocity drift apart and total energy is not conserved. Hairer *et al.* [97] also investigate the symplectic Euler method. Numerical integration of this method shows the right qualitative behaviour, but destroys the left-right symmetry of the pendulum depicted in Figure 4.2. As a result of the calculation for the Kepler problem, depicted in Figure 4.3, the nonsymmetric symplectic Euler method distorts the ellipse. The precession effect of the numerical calculation, although,

is also present in the exact solution of the perturbed Kepler problem and has occupied astronomers for centuries. To achieve the precision needed for the equilibration of the atom cloud, the aforementioned behaviours are not favourable and hence the explicit Euler method as a numerical integration method for the equilibrium code was discarded in favour of the Velocity Verlet method described in the next paragraph.

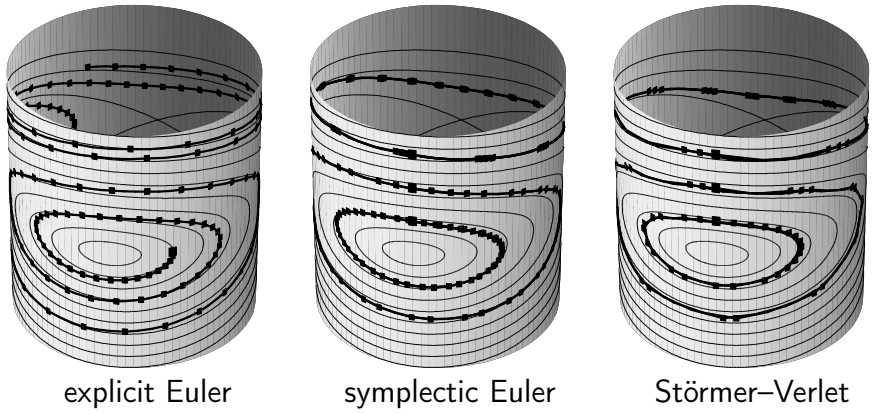

Figure 4.2: Solutions of the pendulum problem. (Reprinted with permission from reference [97]. Copyright (2002) Spinger Nature.)

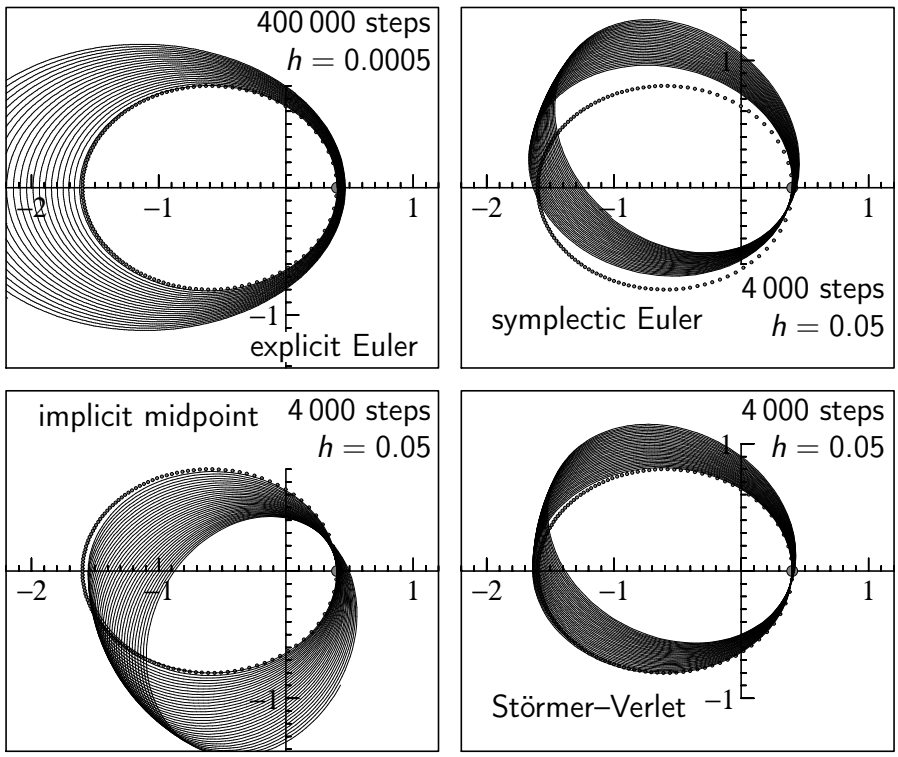

Figure 4.3: Numerical solutions of the Kepler problem with stepsize h. (eccentricity $e = 0.6$; in dots: exact solution) (Reprinted with permission from reference [97]. Copyright (2002) Spinger Nature.)

Velocity Verlet method

The positions and velocities are updated according to following equation and hence the algorithm returns the positions, velocities and forces at the same time.

$$\boldsymbol{r}_i(t+\Delta t) = \boldsymbol{r}_i(t) + \Delta t\,\mathbf{v}_i + \frac{\Delta t^2}{m_i}\,\mathbf{f}_i(t) + \mathcal{O}(\Delta t^3), \tag{4.14}$$

$$\mathbf{v}_i(t+\Delta t) = \mathbf{v}_i(t) + \frac{\Delta t}{2m_i}\left(\mathbf{f}_i(t) + \mathbf{f}_i(t+\Delta t)\right) + \mathcal{O}(\Delta t^3), \tag{4.15}$$

with higher order terms ($\mathcal{O}(\Delta t^3)$ and $\mathcal{O}(\Delta t^3)$) being neglected. The Störmer-Verlet method, depicted in Figure 4.4, can be either interpreted as produced by parabolas with the right second derivative at t_n (see Figure 4.4 to the left) or polygons with the right slope in the midpoint (see Figure 4.4 to the right). It is also known as the Verlet method in molecular dynamics. Generally, it provides a good numerical stability, as presented in figures 4.2 and 4.3, and is a symplectic integrator method and time-reversable. Those are desirable properties, especially when it comes to reflect the physical reality of simulation problems. It comes at no significant additional computational cost over the simple Euler method. In this work, however, the Velocity Verlet method is used, since it calculates the velocity and the position at the same time. This solves the problem of the Störmer-Verlet method in the first time step, where no velocity is known. This leads to a correct spatial and velocity distribution of the ultra cold atoms after equilibration and provides appropriate starting conditions for the simulation.

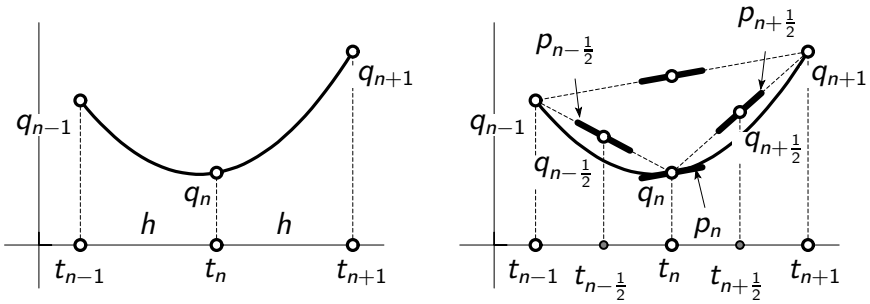

Figure 4.4: Illustration for the Störmer–Verlet method. (Reprinted with permission from reference [97]. Copyright (2002) Spinger Nature.

4.2 Influence of different parameters on the atom cloud

4.2.1 Introduction

To gain comparable results of the shuttling simulations to the actual experiment, it is very important to start with similar conditions. During the initial phase of the simulations, multiple different parameters were tested to understand the simulation behaviour and their influence. Firstly, the initial temperature for the simulation was varied. The initial temperature in the off-center starting position has a big effect on the spread of the kinetic energy of the atom cloud

during the interaction with the atomic and molecular ions and hence on the time-of-flight profiles. In subsection 4.2.2 two temperatures, $T_{\text{init}} = 163\,\mu\text{K}$ and $T_{\text{init}} = 1024\,\mu\text{K}$ separated by an order of magnitude, serve as base differentiation on how other parameters will have an impact on the kinetic-energy spread of the free-flying atom cloud. In general, it has to be mentioned that the initial temperature has no impact on the overall maximum achievable kinetic-energy, only on the kinetic-energy spread. Overall, the kinetic-energy spread for the $1024\,\mu\text{K}$ atom cloud is around 3 mK larger than for the $163\,\mu\text{K}$ atom cloud. The initial position of the atom cloud has to be fixed to ensure the atom cloud is in free flight during the passing of the two boundary conditions representing the two slits of the time-of-flight measurement, otherwise the atom cloud would be accelerated or decelerated and thus falsifying the results. These two conditions are fixed in the equilibration code and are checked manually before the shuttling code is started. To generalise the simulations, the shuttling code has been modified to accept an input file. The shuttling code is available in two variations, one with Y/Z cooling and one without Y/Z cooling.
The input file (see A.2.1) controls following aspect of the simulation:

- Filename of the equilibrated atom cloud
- Additional heating force, saturation intensity and natural linewidth of the ^{87}Rb transition
- Cooling / pushing laser power and detuning, Laser beam $1/e^2$ radius
- Number of atoms
- Predefined time for the pushing laser and the free-flight time (x-axis cooling and pushing laser off)
- Step size of the increase of the push-beam laser power each simulation run and maximum achievable push-laser beam power
- Integration time step size
- Magnetic coil dimensions and the magnetic-field gradient
- Boundary conditions for the single slit at the ion interaction region and the double slit

4.2.2 Initial conditions

For this study, the off-center position of the atom cloud is 1.036 mm from the interaction region and the two different temperatures, are $163\,\mu\text{K}$ and $1024\,\mu\text{K}$. These values were the result of setting the initial conditions of the equilibration code to represent experimental conditions for the off-center position and to achieve two initial temperatures, one close to the Doppler-temperature of Rb and the other offset by an order of magnitude. To distinguish between the two initial temperatures the upper panel of each following figure depicts $T_{\text{initial}} = 163\,\mu\text{K}$

and the lower panel $T_{\text{initial}} = 1024\,\mu\text{K}$. The parameters in question influencing the outcome of the shuttling simulations are the detuning of the cooling laser, the $1/e^2$ beam radius of the cooling and pushing laser, the cooling laser intensity and the magnetic-field gradient of the anti-Helmholtz coils. Each simulation only varies one parameter and all simulations are grouped together by the parameter in question. The results are presented in subsections divided by the parameter in question and simultaneously discuss and compare bright and dark atom simulations. The main focus lies on the difference of the kinetic-energy spread as this influences the collision energy for the reaction dynamics of the atom-ion interaction. The standard parameter sets, which are closest to the experimental condition, is depicted in ○ for both temperatures, as well as for both simulation types with the following values:

- Detuning of the cooling laser: 10 MHz
- $1/e^2$ beam radius: 3.7 mm
- Cooling laser intensity: 15 mW
- magnetic-field gradient of the anti-Helmholtz coils: $18\,\text{G}\,\text{cm}^{-1}$

In the next two subsection the figures of the bright atom simulation and the dark atom simulation will be described. A summary and conclusion of the results will follow in 4.3.

4.2.3 Bright- and dark-atom shuttling simulations

Variation of the cooling-laser detuning

Figure 4.5a (bright-atom simulation) and Figure 4.5b (dark-atom simulation) compare different cooling laser detuning settings. For both temperatures the detuning of 2 MHz (+), 10 MHz (○) and 18 MHz (∗) were assumed in the simulation. The qualitative behaviour of the atom cloud is similar in Figure 4.5a and 4.5b for both temperatures. The atom clouds show a larger minimum and maximum achievable kinetic energy with a larger detuning of the cooling laser. This is due to the relative detuning of the cooling laser to the detuning of the pushing laser, which is 0 MHz detuned to the resonance of the transition. In Figure 4.5a for the case of the 1024 µK atom cloud the kinetic-energy spread disparity at $E_{\text{kin}} = 23$ mK between 2 MHz and 10 MHz is less than 1 mK and between 10 MHz and 18 MHz it is 1 mK. For the 163 µK atom cloud at $E_{\text{kin}} = 23$ mK, the difference is 1 mK between 2 MHz and 10 MHz and 2 mK between 10 MHz and 18 MHz. Comparing the dark-atom kinetic-energy spread of Figure 4.5b to the bright-atom simulations in Figure 4.5a shows a significant improvement. The overall variance is smaller. Between the different detuning settings, it is less than 0.5 mK at $E_{\text{kin}} = 23$ mK for all cases discussed. One striking feature is the larger influence of a cooling effect at a higher detuning on the bright atom simulations. Here, the transversal cooling for the bright atom simulation is indeed beneficial. For the dark atom simulation this effect is negligible.

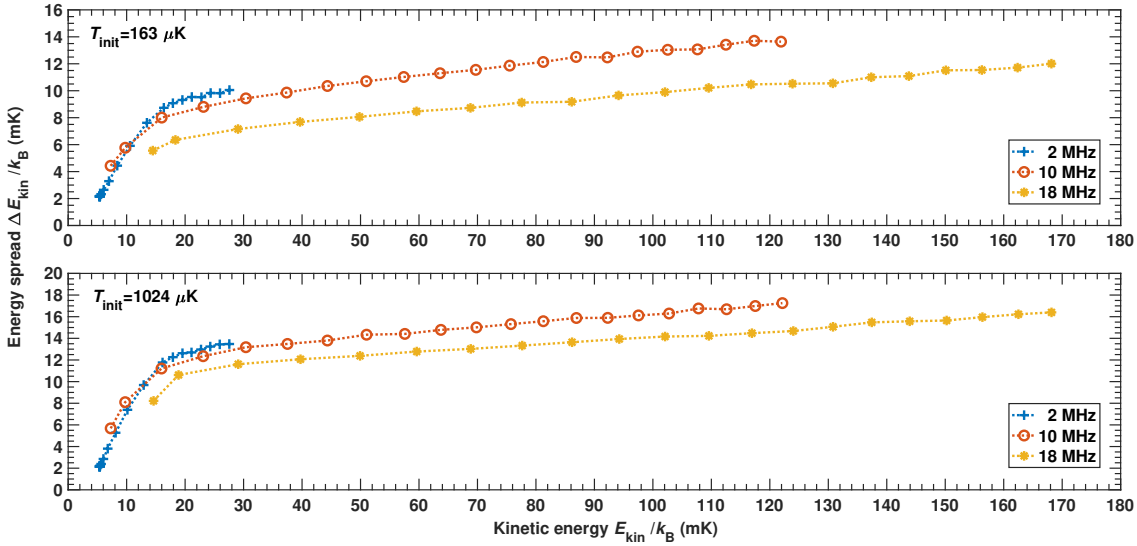

(a) $T_{\text{init}} = 163\,\mu\text{K}$ in the upper panel and $T_{\text{init}} = 1024\,\mu\text{K}$ in the lower panel with additional Y/Z - axis cooling during the free flight period.

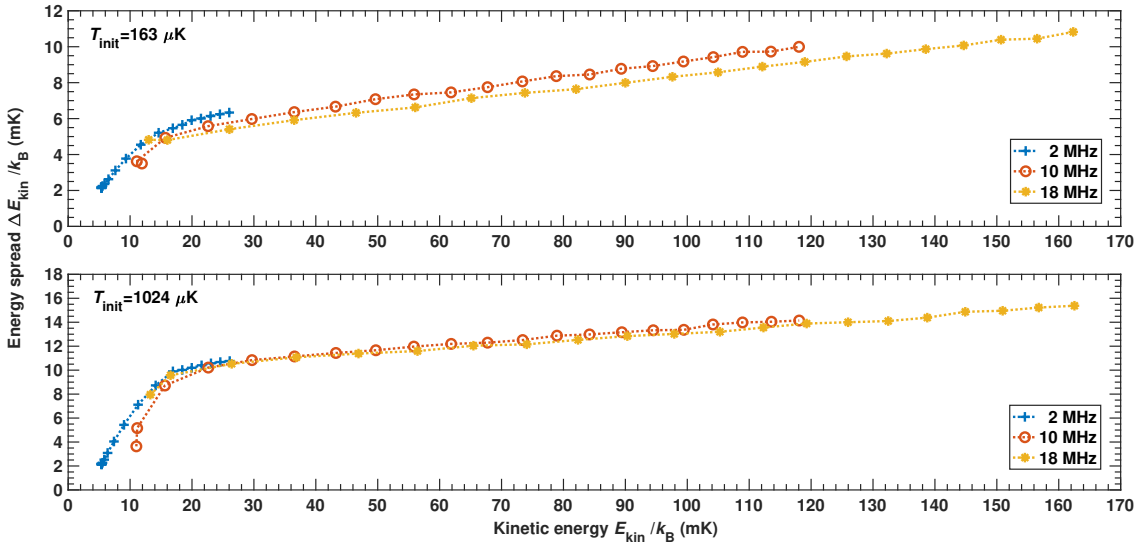

(b) $T_{\text{init}} = 163\,\mu\text{K}$ in the upper panel and $T_{\text{init}} = 1024\,\mu\text{K}$ in the lower panel without additional Y/Z - axis cooling during the free flight period.

Figure 4.5: Influence of the cooling - laser detuning from resonance for 2 MHz, 10 MHz and 18 MHz on the kinetic - energy spread of the shuttling atom cloud for two different temperatures ($T_{\text{init}} = 163\,\mu\text{K}$ in the upper panel and $T_{\text{init}} = 1024\,\mu\text{K}$ in the lower panel). (a) with additional Y/Z cooling during the free flight period. (b) without additional Y/Z cooling during the free flight period.

In conclusion, the cooling detuning variation has an identical influence on the minimum and maximum achievable kinetic energy of the atoms for both types of clouds in both simulations. The kinetic-energy spread is overall smaller for the colder atom cloud and for the dark atom simulation indicating an alteration of the energy spread during the free flight period by the transversal cooling lasers. This effect is also more pronounced in the colder atom cloud.

Variation of the $1/e^2$ radii of the laser beams

Figure 4.6a (bright atom simulation) and Figure 4.6b (dark atom simulation) show the influence of different $1/e^2$ laser-beam radii on the shuttling atom cloud. Different $1/e^2$ beam radii were simulated and are depicted as 1.8 mm (+), 3.7 mm (○) and 7.4 mm (∗). All laser beams are adjusted by setting the beam radii, which also includes the pushing laser, since they use the same out-coupler in the experiment (x-axis beams). Due to the change in the beam radii, the intensity exerted on the atom cloud changes, thus accelerating the atoms differently. A smaller beam radius also leads to less cooling in Y/Z, hence allowing for a larger kinetic-energy spread. The stronger pushing intensity and the lesser cooling lead to a larger energy spread for the 1.8 mm simulations. Comparing the three different beam radii of the bright atom simulation at a kinetic energy of $E_{\text{kin}} = 54\,\text{mK}$ the difference of the energy spread between 1.8 mm and 3.7 mm is 4 mK for the 163 µK cloud and 5 mK for the 1024 µK cloud respectively. The difference of the energy spread between the 3.7 mm and the 7.4 mm is 1.5 mK for the 163 µK cloud and 1 mK for the 1024 µK cloud respectively. In case of the dark-atom simulation, the difference between 1.8 mm and 3.7 mm is 4 mK for the 163 µK cloud and 5 mK for the 1024 µK cloud respectively. This is the same as seen in the bright-atom simulation. The difference of the energy spread between the 3.7 mm and the 7.4 mm is in both temperature cases is marginal. Comparing the results of the simulations, there is not much of a gain in energy spread by making the beam radius twice the size and a huge loss in energy spread when the beam radius is halved compared to the standard size. In conclusion the beam radius chosen for the experiment presents a very stable environment with a large range of selectable kinetic energies at a decent kinetic-energy spread.

Variation of the cooling-laser intensity

Figure 4.7a (bright-atom simulation) and Figure 4.7b (dark-atom simulation) provide information on the effect of the variation of the cooling-laser intensity (6 mW (+), 15 mW (○) and 24 mW (∗)). The intensity listed is the overall intensity of all the cooling-laser beams. A striking feature in Figure 4.7a is not only the kinetic-energy spread, also the highest achievable kinetic energy is influenced by the cooling-laser intensity. The difference of the kinetic-energy spread for the bright atom simulation is 2 mK between 6 mW and 15 mW. Comparing the 24 mW with the 15 mW results, there is only 0.5 mK difference in the kinetic-energy spread, i.e. that the higher the cooling intensity, the smaller the change in the spread.

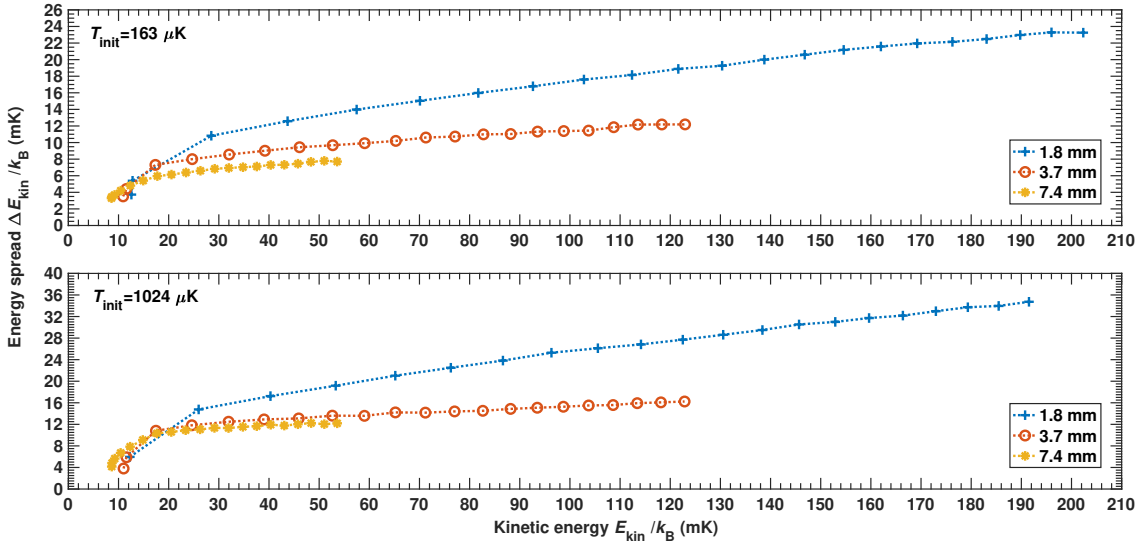

(a) $T_{\text{init}} = 163\,\mu\text{K}$ in the upper panel and $T_{\text{init}} = 1024\,\mu\text{K}$ in the lower panel with additional Y/Z - axis cooling during the free flight period.

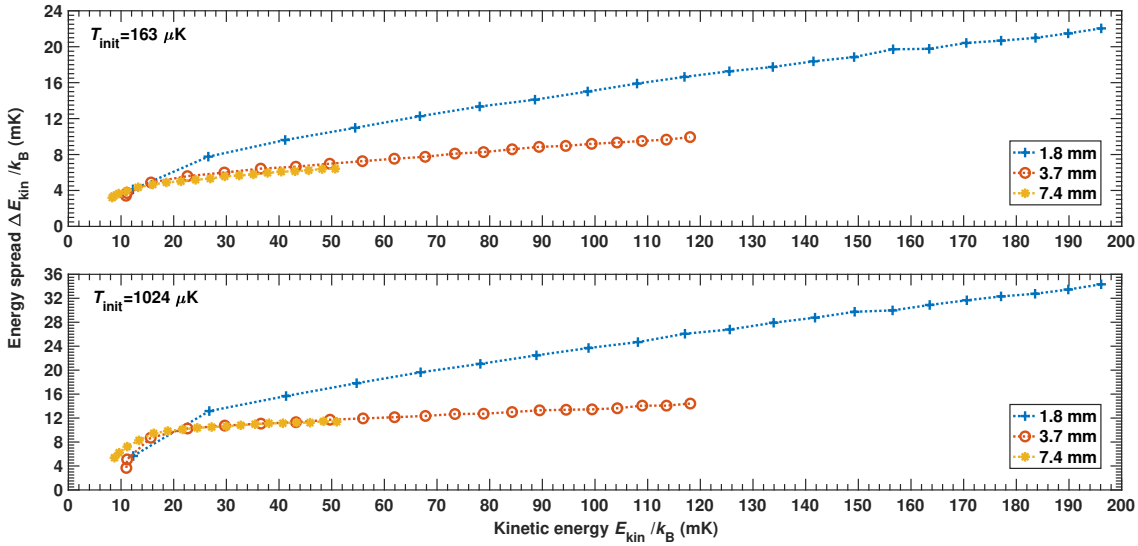

(b) $T_{\text{init}} = 163\,\mu\text{K}$ in the upper panel and $T_{\text{init}} = 1024\,\mu\text{K}$ in the lower panel without additional Y/Z - axis cooling during the free flight period.

Figure 4.6: Influence of the $1/e^2$ laser - beam radius (1.8 mm, 3.7 mm and 7.4 mm) on the kinetic - energy spread of the shuttling atom cloud for two different initial temperatures ($T_{\text{init}} = 163\,\mu\text{K}$ in the upper panel and $T_{\text{init}} = 1024\,\mu\text{K}$ in the lower panel). (a) with additional Y/Z cooling during the free flight period. (b) without additional Y/Z cooling during the free flight period.

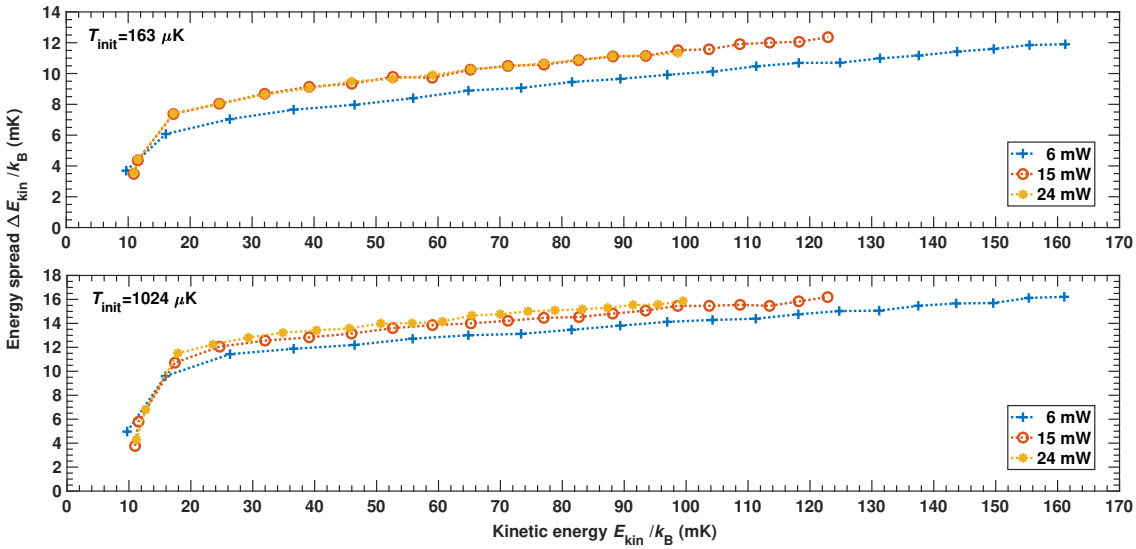

(a) $T_{\text{init}} = 163\,\mu\text{K}$ in the upper panel and $T_{\text{init}} = 1024\,\mu\text{K}$ in the lower panel with additional Y/Z - axis cooling during the free flight period.

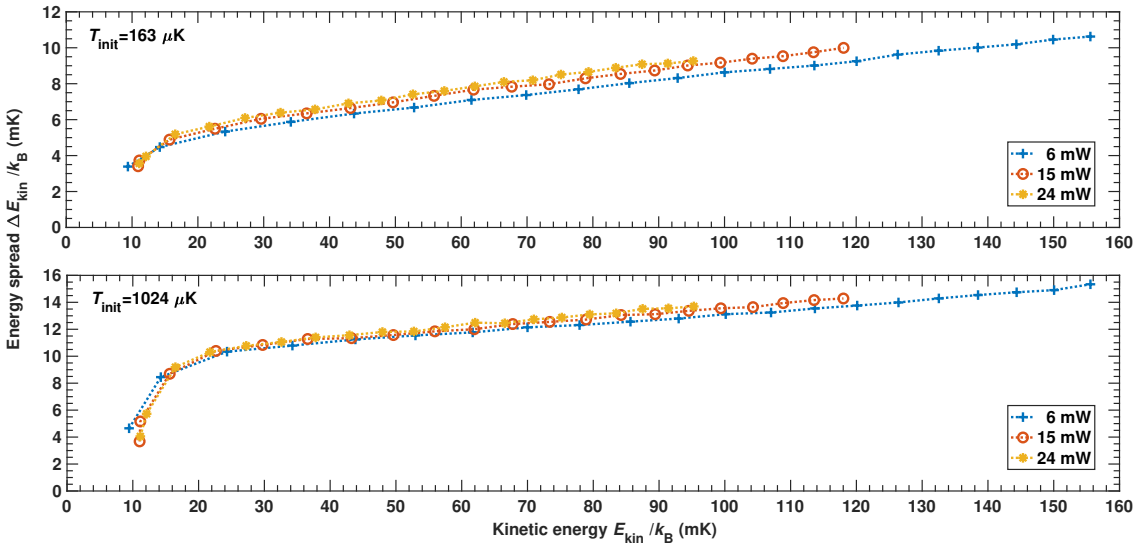

(b) $T_{\text{init}} = 163\,\mu\text{K}$ in the upper panel and $T_{\text{init}} = 1024\,\mu\text{K}$ in the lower panel without additional Y/Z - axis cooling during the free flight period.

Figure 4.7: Influence of the cooling laser intensity (6 mW, 15 mW and 24 mW) on the kinetic-energy spread of the atom cloud for two different initial temperatures ($T_{\text{init}} = 163\,\mu\text{K}$ in the upper panel and $T_{\text{init}} = 1024\,\mu\text{K}$ in the lower panel). (a) with additional Y/Z cooling during the free flight period. (b) without additional Y/Z cooling during the free flight period.

The disparity of the energy spread between the different intensities is less in case of the dark atom simulation. The maximum kinetic-energy for the 6 mW simulation is 60 mK higher than for the 24 mW results in both simulations, thus the cooling intensity has a large influence on the maximum kinetic energy. This rises the question how the transversal cooling alters the kinetic energies of the atom cloud. For both simulations, the atom clouds slow down as the cooling-laser intensity gets stronger. Since there is no transversal cooling in Figure 4.7b, but the kinetic energies are still lower for the highest cooling intensity, it leads to the conclusion that the influence on the kinetic-energy is already present during the pushing period of the simulation. At the beginning of the simulation, the atom cloud gets accelerated and is simultaneously cooled transversally. The higher cooling-laser intensity during this stage does not allow the atom cloud to reach higher velocities. An analogy to understand this behaviour is a ball thrown through a stream of honey at different densities, hitting the ball at a ninety degree angle. The higher the density of the honey the harder it would be for the ball to pass through, at a given force exerted on the ball in forward direction.

Variation of the magnetic-field gradient

Figure 4.8a (bright atom simulation) and Figure 4.8b (dark atom simulation) illustrate the results on the variation of the magnetic-field gradient of the anti-Helmholtz coils. Simulations are presented at $4\,\mathrm{G\,cm^{-1}}$ (+), $18\,\mathrm{G\,cm^{-1}}$ (○) and $32\,\mathrm{G\,cm^{-1}}$ (∗). This parameter has no observable effect on the kinetic-energy spread nor the highest achievable kinetic-energy. In the experiment however, the magnetic-field gradient determines the position of the atom cloud in space and is critical for stable shuttling conditions. $18\,\mathrm{G\,cm^{-1}}$ was the most stable setting and hence it was used for all experimental data presented in this work.

4.3 Summary and conclusion

This chapter has discussed the numerical calculation of a shuttling ultra-cold atom cloud. In a short introduction, the link to the experiment was given and the approach of the work of von Planta [96] was described. The two separate codes 'Equilibrium' and 'Shuttling' were introduced and how they generate the results in section 4.2. The change from the explicit Euler method to the Velocity Verlet method was covered in section 4.1.3. The exchange is justified based on the non-symplecticity of the explicit Euler method. The explicit Euler method causes the two test cases presented in Figure 4.2 and Figure 4.3 to result in non-physical behaviour. By contrast the Störmer-Verlet method, a symplectic integration method, calculates physically correct results. Its shortcoming of the unknown velocity for the first integration step was bypassed by using the Velocity-Verlet method instead, resulting in appropriate starting conditions after equilibration. The simulations were computed with two different initial temperatures (T_{init}=163 µK, T_{init}=1024 µK) of the atom clouds at the same initial off-center position to ensure comparable results. Additionally, the influence of the transversal cooling

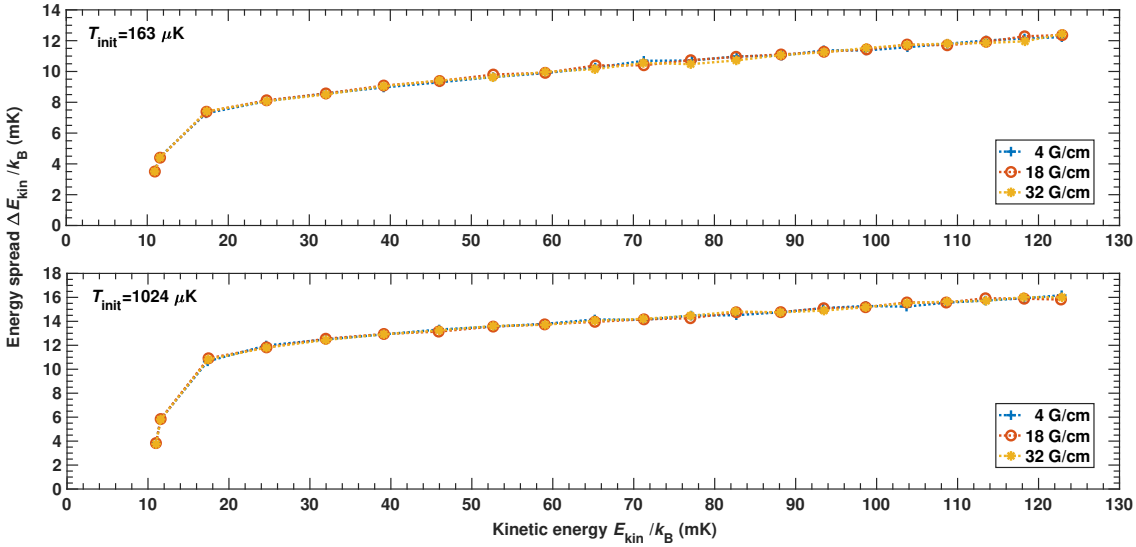

(a) $T_{\text{init}} = 163\,\mu\text{K}$ in the upper panel and $T_{\text{init}} = 1024\,\mu\text{K}$ in the lower panel with additional Y/Z - axis cooling during the free flight period.

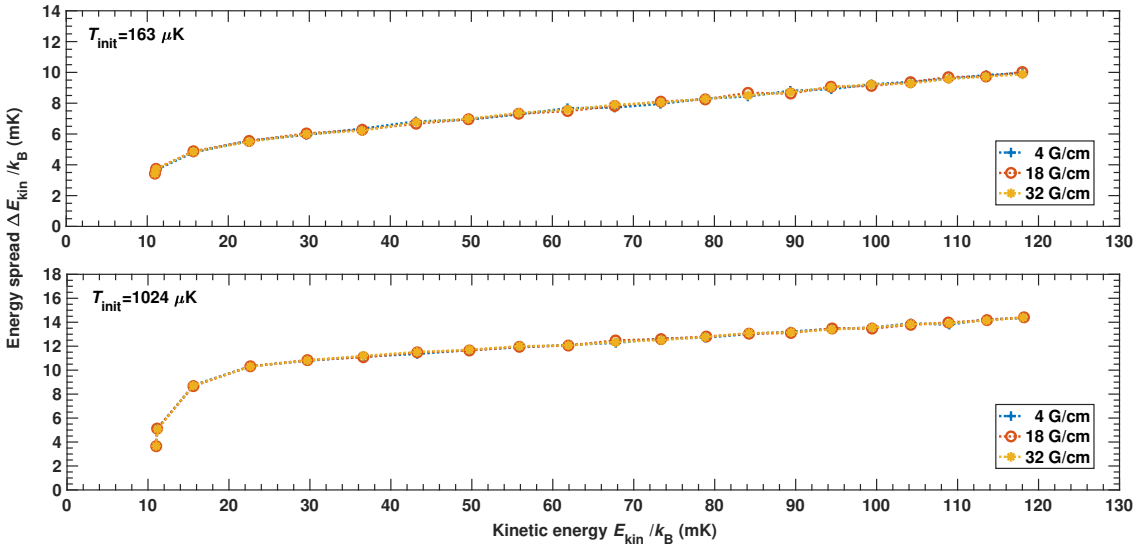

(b) $T_{\text{init}} = 163\,\mu\text{K}$ in the upper panel and $T_{\text{init}} = 1024\,\mu\text{K}$ in the lower panel without additional Y/Z - axis cooling during the free flight period.

Figure 4.8: Influence of the magnetic - field gradient ($4\,\text{G}\,\text{cm}^{-1}$, $18\,\text{G}\,\text{cm}^{-1}$ and $32\,\text{G}\,\text{cm}^{-1}$) on the kinetic - energy spread of the atom cloud for two different initial temperatures ($T_{\text{init}} = 163\,\mu\text{K}$ in the upper panel and $T_{\text{init}} = 1024\,\mu\text{K}$ in the lower panel). (a) with additional Y/Z cooling during the free flight period. (b) without additional Y/Z cooling during the free flight period.

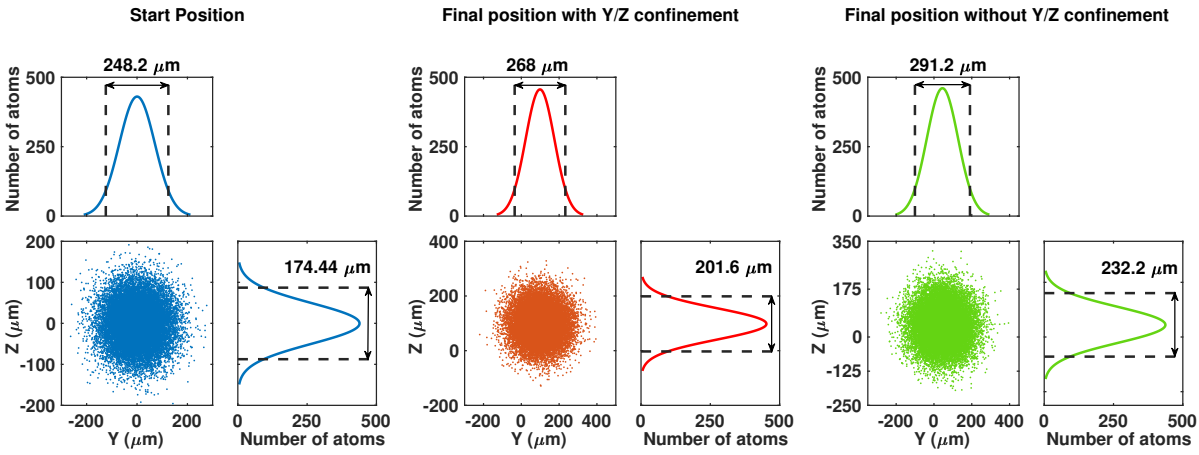

Figure 4.9: Sample of the transversal spatial spread of the atom cloud at the beginning of the simulation(left), at the stop of the bright-atom simulation (middle) and the stop of the dark-atom simulation (right). The atom cloud at the end of the dark-atom simulation is slightly larger than the atom cloud for the bright-atom simulation. This is due to the lack of transversal cooling during the free flight period and influences the final kinetic energy of the simulation.

during the free flight period of the atom cloud was investigated. The investigated parameter space includes variations of the cooling laser detuning, the $1/e^2$ beam radius, the cooling laser intensity and the magnetic-field gradient of the anti-Helmholtz coils. The results are depicted in Figures 4.5a, 4.6a, 4.7a and 4.8a for the transversally confined atom simulations and in Figures 4.5b, 4.6b, 4.7b and 4.8b for the non transversally confined atom simulations, respectively. In each simulation, the standard parameters are shown as ○. Generally, the simulations with the transversally confined atoms show a higher kinetic-energy in contrast to the transversally unconfined atoms. The reason behind this difference can be explained by the larger transversal spatial spread of the atoms at the final stop of the simulation depicted in Figure 4.9. Since there is no cooling during the dark shuttling simulations, the atom cloud slightly expands in the transversal direction, hence loosing kinetic-energy in the longitudinal direction. Simulations concerning the variation of the magnetic-field gradient show no influence neither in the resulting kinetic-energy spread nor the maximum achievable kinetic energy of the atoms, thus the standard parameter is used in the experiments, because it provided the most controllable environment. For the variation of the cooling-laser detuning in Figure 4.5a and Figure 4.5b, the only difference which needs to be highlighted is the overall kinetic-energy spread being smaller for the initially colder atom cloud. The illustration of the effect of the variation of the different $1/e^2$ beam radii in Figure 4.6a and Figure 4.6b have presented a similar result. In both

cases the 1.8 mm $1/e^2$ beam radius showed a strong increase of the maximum finally achieved kinetic energy, due to the higher spatial intensity exerted on the atoms. The resulting kinetic-energy spread is also large, since part of the kinetic-energy is reverted into a spatial spread of the atoms. At the largest beam radius investigated, the maximum kinetic-energy does not exceed 54 mK. Considering the lower momentum exerted on the atoms the kinetic-energy spread is much smaller, about 6 mK compared to the smallest beam radius. In case of the cooling-laser intensity variation, the figures present a similar but reversed behaviour as previously seen in simulations concerning the cooling-laser detuning variation. For both temperature cases, the dark atom simulations show a lower kinetic-energy spread and a slightly smaller maximum kinetic energy. The influence of the cooling laser intensity, altering the maximum kinetic energy between the largest and the lowest intensity simulated, impacts the atom cloud during the pushing period only. Both dark- and bright-atom simulations show a difference of $E_{\mathrm{kin}} = 60$ mK between 6 mW and 24 mW. In conclusion, the simulations presented a very steady picture for the standard parameters with an upper bound for the achievable energy spread in the experiment as indicated by the bright atom simulation. The standard parameters used in the simulations in combination with the warmer atom cloud are comparable to the experiment and can be used to discuss the experimental results.

5 Rotational state-changing collisions and radiative association of $N_2^+ + Rb$

In cold ion-neutral collisions of $N_2^+ + Rb$, rotational state-changing collisions and radiative association to form a molecule like $[N_2Rb]^+$ or $[N_2Rb]^{+*}$ occur. The theoretical investigation of these processes will be the subject of this chapter. The first part aims to explore the rotational state-changing collisions computationally, to justify if an experimental exploration is feasible in the present experiment. The main idea is to make use of the dynamic hybrid trap system to find out if the rotational states change depending on the collision energy and if there are specific resonant features, especially in the low collision energy regime at the mK range. In this work, two theoretical approaches were considered. One is the work of González-Martínez *et al.* [98]. In his work he discusses the statistical product-state distributions for ultracold reactions in external fields. It is a generally tractable, rigorous theoretical framework which evades the main limitation of most ultracold chemistry studies, which is the lack of an analysis of reaction products. The second theoretical approach is the all spin scattering code (ASPIN), developed by López-Durán *et al.* [99]. This code aims at the quantum calculation of integral cross sections for atom-molecule (linear) scattering processes. The atom is considered structureless, while the molecule is a rigid rotor in its singlet, doublet or triplet spin states ($^1\Sigma$, $^2\Sigma$ or $^3\Sigma$). Both methods have their benefits. While the statistical approach does not have the need for a pre-calculated potential energy surface, it does need the two collision partners to stay long enough together, in close vicinity, for the reaction product distribution to become statistical. The ASPIN code calculates all the relevant state-to-state integral cross sections and their sums over final states, but it does need a potential energy surface, which can be tricky to obtain and in some cases needs a very careful selection of the right surface. The following section will discuss the statistical approach and why it is not feasible in the context of this theoretical exploration and the ASPIN code and its results in more detail. The final section of this chapter will discuss the results obtained for the radiative association (RA) process in case of N_2^+-Rb $(5s)\ ^2S_{1/2}$ and will explain in more detail, why the molecular ions $[N_2Rb]^+$ or $[N_2Rb]^{+*}$ are not likely to show in the experiment in contrast to atomic systems investigated previously [25, 27, 30, 38]

5.1 The statistical product - state distributions for ultracold reactions in external fields

In the work of González-Martínez *et al.* [98], a method to theoretically obtain statistical product - state distributions and state - to - state cross sections for ultracold reactions in external fields is derived. Two main effects are discussed as a result of the external fields. One is the modification of the product energy levels and subsequent reshaping of the product distribution. The second one is adding or removing product states as the reaction exothermicity is changed. This is achieved by connecting traditional statistical theories [100, 101] and ultracold collision theory [102]. To obtain the product - state distribution, the reaction cross section needs to be calculated first, which is done by adding all contributions from state - to - state cross section. Equation (5.1) describes the rigorous quantum - mechanical expression from reactant state α to product state β at a given projection of the total angular momentum on the field axis, M, energy E, and a field strengh F.

$$\sigma^M_{\alpha\to\beta} = \frac{\pi\hbar^2 g_\alpha}{2\mu_\alpha(E-E_\alpha)} \times \sum_{L_\alpha M_\alpha} \sum_{L_\beta M_\beta} \left| S^M_{\alpha L_\alpha M_\alpha;\beta L_\beta M_\beta}(E,F) \right|^2 \tag{5.1}$$

The reactant state are α and β with their respective energies E_α and E_β, their space - fixed orbital angular momenta are L_α and L_β with their respective projections on the field axis M_{L_α} and M_{L_β}. The transitions probability $P^M_{\alpha rightarrow\beta}$ form state α to β is defined by the sum over the absolute squares of S - matrix elements. In this model, it is assumed that reaction always proceeds through complex formation, rendering the reactant and product channels dynamically independent. The transition probability can be rewritten following Hauser and Feshbach [100] and Miller [101],

$$P^M_{\alpha\to\beta} \approx p^M_\alpha p^M_\beta / \sum_\gamma p^M_\gamma, \tag{5.2}$$

where the explicit E and F dependence has been omitted. The p^M are capture probabilities (i.e. the probability of complex formation, for given M). If all capture probabilities are considered uncorrelated, equation (5.2) satisfies the principle of detailed balance. The statistical state - to - state cross section can be rewritten as:

$$\sigma_{\alpha\to\beta,r} = \frac{\pi\hbar^2 g_\alpha}{2\mu_\alpha(E-E_\alpha)} \sum_M p^M_\alpha \frac{p^M_\beta}{p^M_\gamma}. \tag{5.3}$$

The total reaction cross section $\sigma_{\alpha,r}$ is then found by summing over all possible product states β and the related total reaction rate $k_{\alpha,r} = \left[2\left(E-E_\alpha\right)/\mu_\alpha\right]^{1/2}\sigma_{\alpha,r}$. The probability density corresponding to an observable X in the product is expressed by

$$\mathcal{P}_\alpha(X) = \left(\sum_M p^M_\alpha \frac{\sum_\beta p^M_\beta}{\sum_\alpha p^M_\gamma}\right)^{-1} \left(\sum_M p^M_\alpha \frac{\sum_\beta \frac{\partial p^M_\beta}{\partial X}}{\sum_\alpha p^M_\gamma}\right), \tag{5.4}$$

where the proportionality constant is represented by the first term in the parentheses. Detailed statistical predictions for observables of a chemical reaction in an external field are then provided by equations (5.3) and (5.4). The implementation details, the capture models as well as the results of the test case involving ^{40}K, ^{87}Rb, are discussed in detail in Ref. [98]. As mentioned previously, a reaction can be seen as statistical if the reaction always proceeds through complex formation, rendering the reactant and product channels statistically independent. Following the reaction dynamics explored in Ref. [4, 103] and considering the computed results for the rates and the involved RA processes, the discussed reaction dynamic of $N_2^+ + Rb$ can not be considered statistically independent. Also it will become later apparent with results presented in Figures 5.4a, 5.4b and Figure 6.8b, that due to the dependence of the cross section on the initial rotational state of the N_2^+ and the collision-time t dependence on the impact parameter b the reaction can also not be considered statistical. Therefore calculations based on the theoretical construct of the work of González-Martínez *et al.* [98] shall not be considered further.

5.2 ASPIN: Methods, Results and Discussion

5.2.1 Computational Methods

Ab initio potential and multichannel quantum dynamics

Relevant PESs (potential energy surface) were calculated by Prof. Yurtsever [103] using the MOLPRO suite of *ab initio* computational programs [104]. The basis set used was aug-CC-PVQZ (aug: augmented, CC-P: correlation consistent-polarised, V: valence-only, QZ: Quadruple-zeta). For the selections at the CASSCF (Complete Active Space Self Consistent Field) level [104], the complete active space for the molecular ion and an ECP (effective core potential) for the Rb atom were considered, as defined in Ref [105]. Nine out of the 28 electrons from the ECP were correlated with the active electrons from the nitrogen molecular ion. Four states, with six closed shell, nine active orbitals and ten electrons, were employed for the MCSCF (multi-configural self-consistent-field) method to optimise the wave-functions. For the lowest four states, MRCI (multi-reference configuration interaction) calculations were carried out, starting with the MCSCF wave-functions. At medium to large distances, the lowest root always corresponded to an exit channel with the Rb^+ ion and depending on the complex, the lowest 3^{rd} or 4^{th} root was usually the entrance channel with the N_2^+ [103]. For Davidson-rotated reference-corrected MRCI eigenvalues, the energies corresponding to both channels were selected by analysing the charge on the Rb. N_2^+ was treated as a rigid rotor in its vibrational ground state in Jacobi coordinates (R,Θ,r_{eq}),where R denotes the radial distance of either the Rb (or the Rb^+) from the mid-point of the N_2^+ (or of the N_2 molecule at the same geometry) bond, Θ is the angle of approach ($\Theta = 0°$ for the collinear $N_2^+ \cdots Rb$, $\Theta = 90°$

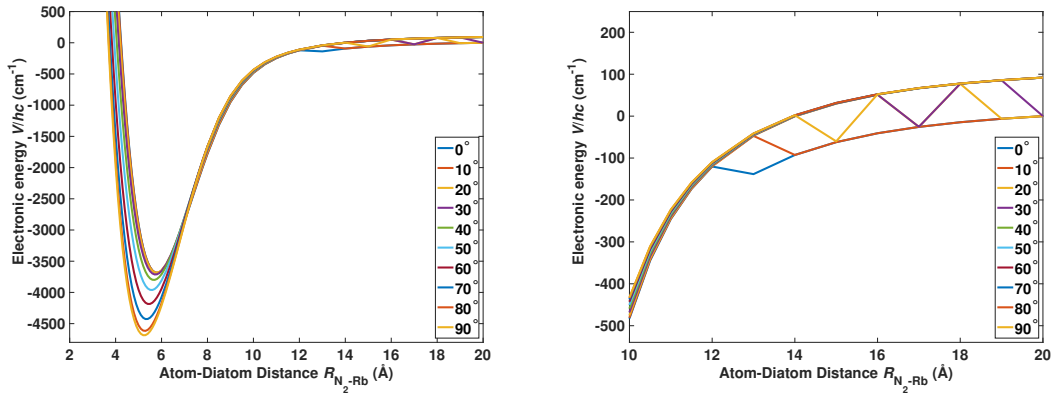

(a) (b)

Figure 5.1: Calculated 2d PES are shown with (a) an illustration of the calculated angle dependent PES from MOLPRO for $N_2^+ + Rb$ and (b) a D detailed zoom of the asymptotic behaviour of the PES. The jumps in the values in the range of 12 Å to 20 Å in (b) are according to Yurtsever [106] the results of the size constrains in the definition of the active space in MCSCF and MRCI calculations limited by computing power.

for the T-shaped geometry) and the neutral and an equilibrium distance of $r_{eq} = 1.178$ Å. A discrete radial grid ranging from R =2 Å to 20 Å at the angles $\Theta = 0°$ to 90° with a step size of $\Delta\Theta = 10°$ was used to build a 2d PES. Figure 5.1 shows the energies of the calculated PES from MOLPRO by Yurtsever for N_2^+-Rb in dependency of atom-diatom distance for different values of Θ. In the short range part up until 10 Å the PESs look reasonable. Figure 5.1b shows a detailed zoom on the range R = 10 Å to 20 Å. According to discussions with Yurtsever, the irregularities in the long-range part of the potential are due to the size constrains in the definition of the active space in MCSCF and MRCI calculations limited by the available computing power. As the distance from Rb to the center of mass of N_2^+ changes, the orbitals (and sometimes the order of them) may change drastically, especially in the region where the molecule is no longer a complex but two separate species. So he concludes, using the same ordered orbitals in these regions create these fluctuations. One solution would have been to test the orbitals at every step. That still would have resulted in oscillations, since different orbitals are used for near geometries. To overcome this limitation, the PES were fitted as described below.

Potential energy surface fitting

P. Villarreal *et al.* prepared the PES for their calculations of the radiative association process (see [103]) by fitting the potential of the entrance energy surface following (5.5) within the

radial interval 2.5 Å$\leq R \leq$20 Å at $\theta = 0°$ and $\theta = 90°$

$$V(R;\theta) = \begin{cases} \sum_{n=0}^{6} p_n(\theta) exp[-n\alpha(\theta)(R - R_0(\theta))], & R \leq R_c \\ \sum_{n=4}^{8} \frac{C_n(\theta)}{R^n}, & R > R_c, \end{cases} \tag{5.5}$$

with the matching point at R_c =10 Å which behaves properly at long distances as the leading term is of the form $\propto -1/R^4$. From the averaged value $C_4 = (C_4(0) + 2C_4(90))/3$, the obtained isotropic dipole polarisability of Rb is $\alpha_0^{Rb} = -2C_4 \approx= 46.7\,\text{Å}^3$ which is close to the asymptotic experimental value (48.7 Å^3) [107]. The corresponding parameters for the two extreme orientations ($\theta = 0$, $\theta = \pi/2$), and also at the intermediate one θ =40° are listed in Table 5.1. If one considers a simple expansion in terms of P_0, P_2 Legendre polynomials

$$V(R,\theta) = V_0(R) + V_2(R)P_2(cos\theta) \tag{5.6}$$

the components are straightly obtained from

$$\begin{aligned} V_0(R) &= [V(R,0) + 2V(R,\pi/2)]/3, \\ V_2(R) &= 2[V(R,0) - V(R,\pi/2)]/3. \end{aligned} \tag{5.7}$$

Expanding to the $V_4P_4(cos\theta)$ term by considering, e.g. an intermediate configuration ($\theta = 40$) one obtains by collocation

$$\begin{aligned} V_2(R) &= [0.694V(R,0) + 0.625V(R,40) - 1.319V(R,\pi/2)]/1.5925, \\ V_4(R) &= [V(R,0) - V(R,\pi/2) - 1.5V_2(R)]/0.625, \\ V_0(R) &= V(R,0) - V_2(R) - V_4(R). \end{aligned} \tag{5.8}$$

Analytical fits with just P_0, P_2 terms are depicted in Fig.5.2a. The fit yielded almost acceptable results, although at the intermediate orientations (from 40° to 60°), the analytic curves overestimate the well - depth by $\sim$100 cm^{-1}. The situation is fully corrected when an additional P_4 term is included, see Fig.5.2b. Fig.5.2c displays the coefficients $V_\lambda(\lambda = 0, 2, 4)$. The overestimation of the well - depth of the isotropic term V_0 from the P_0, P_2 expansion is a consequence of what happens with the intermediate orientations. Higher order terms are not depicted since their contributions are shielded by the steep repulsive potential generated by the $\lambda = 2$ term below $R = 4$ Å. The isotropic polarisability α_0 is represented by the $\lambda = 0$ term and the dipolar polarisability α_2 by the $\lambda = 2$ term. Both terms scale with R^{-4} for $R \to \infty$ and together they describe the polarisability as $\alpha_0 P_0 + \alpha_2 P_2(\cos\Theta)$. The molecular ion polarising the impinging atom caused by the attractive long - range forces and by the anisotropic forces at short distances up to the repulsive wall describing the interaction between the molecular ion and the interacting Rb atom. The terms $\lambda = 2, 4$ terms represent the anisotropy of the interaction and is the driving force for the rotationally state - changing collisions. A strong indication for the elastic process to be dominant over the inelastic ones in

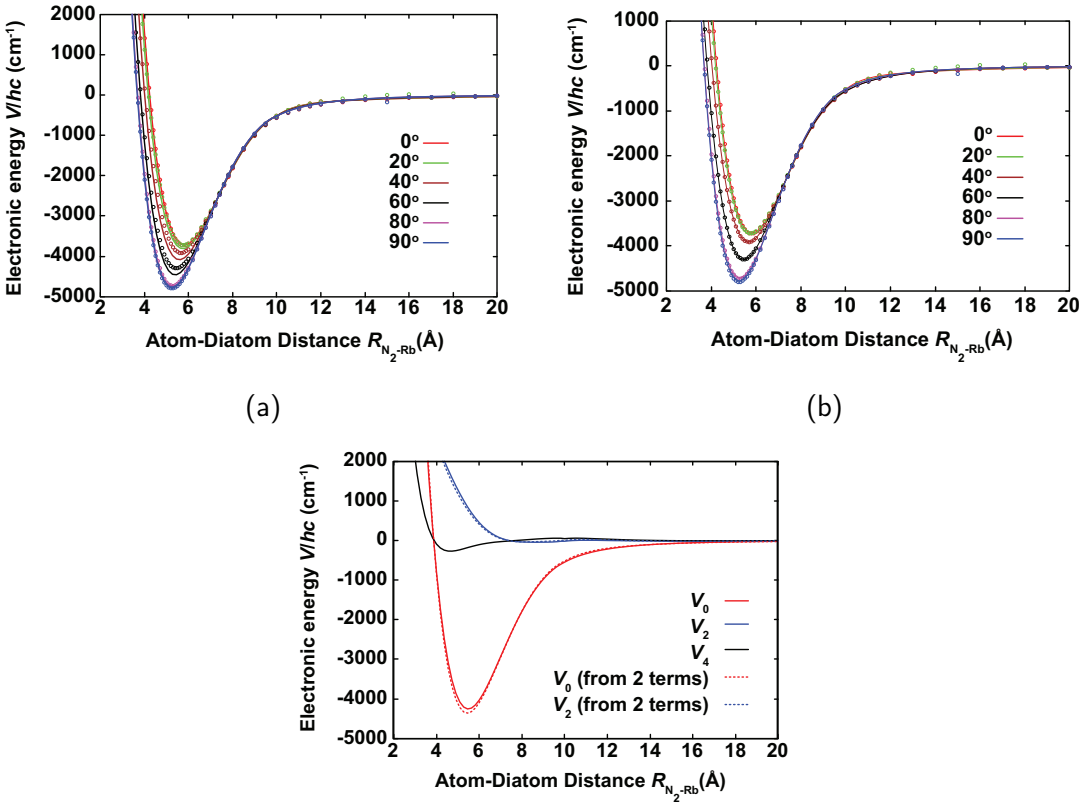

Figure 5.2: Illustration of the analytically fitted rebuilt of the PES for two-terms Legendre (a) and three-terms Legendre expansions (b), respectively. (a) The analytical fit of the rebuild PES with a two-terms Legendre terms P_0 and P_2. The fits works well for the extreme orientations, buts overestimates at the intermediate orientations. (b) The same analytical curves fitted to the rebuild PES with the additional Legendre term P_4. The PES is now correctly represented by the including the 4^{th} term. (c) The analytical terms in the Legendre expansion up to the fourth order depicted in solid lines and up to the second order in dotted lines.

Table 5.1: Parameters for the analytic description of the interactions. Note that in order to maintain the actual relative position of the potentials, those of the entrance channel (*up*) should be shifted by adding an amount of 0.430176332 E_h=94,412.79 $cm^{-1} \approx 11.71$ eV.

	V_{coll}^{up}	V_{T}^{up}	V_{coll}^{down}	V_{T}^{down}
R_0(Å)	5.8	5.25		
α(Å^{-1})	0.034368	0.034468		
p_0(cm^{-1})	-1756256.63	-262228016.79		
p_1(cm^{-1})	12544629.15	1657141129.59		
p_2(cm^{-1})	-30069857.17	-4348781360.99		
p_3(cm^{-1})	26102330.12	6062945894.88		
p_4(cm^{-1})	3701700.96	-4733245170.05		
p_5(cm^{-1})	-17639551.38	1960411915.99		
p_6(cm^{-1})	7113286.78	-336249184.65		
C_4(cm^{-1}Å^4)	-2437572.32	-2869054.88	-691768.92	221520.69
C_5(cm^{-1}Å^5)	-308701429.10	-535117.89		
C_6(cm^{-1}Å^6)	5063017522.48	-113620695.71	27268840.32	-10591580.01
C_8(cm^{-1}Å^8)	-225693428343.86	-11575979814.12	-800973102.58	215252540.69
C_{10}(cm^{-1}Å^{10})			10655848942.91	-2679823716.66
C_{12}(cm^{-1}Å^{12})			-56274742470.61	19810792602.71
C_{14}(cm^{-1}Å^{14})			111187148552.10	-56895816557.42

the present system is the magnitude of the isotropic V_0 significantly exceeding the on of the anisotropic contributions V_2 and V_4. An other interesting feature is the effective shielding of large parts of the non - vanishing sections of the $V_4(R)$ potential by the repulsive part of the $V_2(R)$ curve so that it can be expected that the major inelastic processes will involve changes of two units of rotational angular momentum, i.e., $\Delta N = \pm 2$.

Multichannel quantum dynamic calculations

The coupled channel equation (Ref. [99], Equation (2.6)) is as follows:

$$\left\{\mathbb{I}\frac{d^2}{dR^2} - \frac{\mathbb{L}^2(R)}{R^2} + \mathbb{K}^2 - \mathbb{V}(R)\right\}\mathbb{G}(R) = \mathbb{O}, \tag{5.9}$$

where $\mathbb{L}^2(R)$ being the squared orbital angular momentum L represented as a matrix and $\mathbb{K}^2$ being the diagonal matrix of the asymptotic squared wavevectors. The LogDerivative matrix $\mathbb{Y}$, Equation (5.10), is defined as a combination of the solution vectors to a matrix Υ, which

then satisfies the Riccati matrix Equation (5.11).

$$\mathbb{Y} = \frac{\Upsilon'}{\Upsilon}, \tag{5.10}$$

$$\frac{d\mathbb{Y}}{dR} + \mathbb{W} + \mathbb{Y}^2 = 0, \tag{5.11}$$

$$\Upsilon(R) = \mathbb{J}(R) - \mathbb{N}(R)\mathbb{K}, \tag{5.12}$$

$$(\mathbb{N}' - \mathbb{Y}\mathbb{N})\,\mathbb{K} = \mathbb{J}' - \mathbb{Y}\mathbb{J}. \tag{5.13}$$

The potential matrix $\mathbb{V}$ is contained in $\mathbb{W} = \mathbb{K}^2 - \mathbb{V}(R) - \mathbb{L}^2(R)\,R^{-2}$. The S - matrix and the cross section are obtained by calculating the $\mathbb{K}$ - matrix. The propagation finishing in the asymptotic region presents scattering observables in the form of free - particle solutions and unknown mixing coefficients expressed in Equation (5.12). $\mathbb{J}(R)$ and $\mathbb{N}(R)$ are the Riccati - Bessel and Riccati - Neumann functions respectively and the $\mathbb{K}$ - matrix can be calculated following Equation (5.13). The radial range of integration for large collision energies up to 1000 K was 220 Å, using a total of 3000 steps, with a maximum number of total angular momentum values $J_{max} = 350$, while the maximum number of rotational channels was 23. The radial range of integration for very low collision energies up to 70 mK was 30 000 Å, using a total of 60000 steps, with a maximum number of total angular momentum values $J_{max} = 18$, while the maximum number of rotational channels was 23. Convergence of the calculation was checked for both.

5.2.2 Analysis and results of the ASPIN calculations

Figure 5.3 shows the integrated cross sections (ICS) for the rotationally elastic collisions. In Figure 5.3a, the N_+^2 moiety is treated as pseudo - singlet electron species, i.e., it is treated as a closed - shell system and spin - rotation coupling is neglected. The reported elastic cross sections are for the lowest rotational levels $N = 1, 3, 5, 7$ of the molecular ion for collision energies up to $E_{coll}/k_B = 1000$ K. The resulting cross sections are monotonically decreasing with increasing collision energy which is a general behaviour often observed in elastic cross sections. To prove the computational validity of treating N_+^2 as a pseudo - singlet rather than a doublet electronic state, the latter requiring the incorporation of spin - rotation coupling in the scattering calculations, was done by comparison of the computed spin - rotation resolved elastic cross sections in Figure 5.3b with the results of Figure 5.3a. Both calculations agree well with each other showing a consistent energy dependence. The present discussion of purely rotational effects in the scattering is represented well by the pseudo -, singlet approach due to the marginal differrences which are negligible, thus producing physically reliable results for the quantities of interest (rotationally resolved cross sections). In Figure 5.4 the ICS for rotational excitation, Figure 5.4a, and rotational de - excitation, Figure 5.4b, are shown for the lowest rotational states in collisions between N_2^+ and Rb in the energy range up to

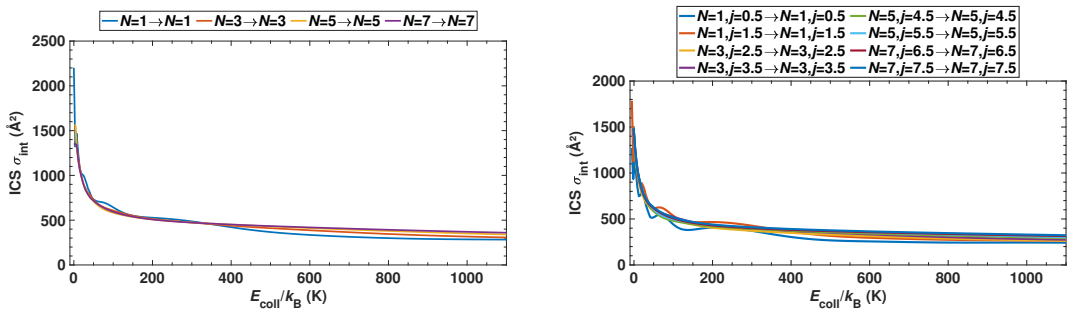

(a) (b)

Figure 5.3: Comparison of the computed elastic integrated cross sections (ICS) for N_2^+ treated as a pseudo-singlet-spin (a) with the results of with N_2^+ treated as a doublet-electron-spin (b). Both calculations were performed with the same settings. The difference in the results is a marginal lower ICS for the doublet treatment, hence for further investigation it was deemed sufficient to performed the calculation with N_2^+ considered as a singlet to reduce computing time.

$E_{coll}/k_B = 1200\,K$. It has to be noted that only state changes with even values of ΔN are allowed given the conservation of nuclear spin symmetry during the collision. Over the entire range of collision energies surveyed, the rotational excitation and de-exitation cross sections show a monotonically increase with collision energy and a fairly similar behaviour. The rotationally inelastic cross sections in both processes on the order of 1 Å to 100 Å in the collision energy interval E_{coll}/k_B =100 K to 1000 K are in line with the expected order of magnitude for such processes in an ionic system, see, e.g., Refs. [108, 109] for comparison. For the transitions involving the lowest rotational states ($N = 1$ to 3 and $N = 3$ to 5 and vice versa), the most distinctive difference is the factor of two difference between the ICS of the excitation and de-excitation. Given the different energy gaps exhibited by the processes, this is reasonable. The cross sections involving changes in the rotational quantum number $\Delta N = \pm 4$ are about one order of magnitude smaller compared to those associated with $\Delta N = \pm 2$. This reflects the relative magnitude off the $V_{\lambda=2,4}(R)$ discussed in 5.2.1.

In Figure 5.5, the cross section in the cold regime at collision energies around several tens of millikelvin are shown. These are particularly relevant for hybrid trap experiments. Figure 5.5a and rate constant k (5.5c,5.5e) for elastic collisions. The rate coefficient in Figure 5.5c were calculated under the assumption of an infinitely narrow spread of collision energies in the experiment according to

$$k = \sigma \sqrt{\frac{2E_{coll}}{\mu}}, \tag{5.14}$$

where σ is the ICS and μ the reduced mass of the N_2^+-Rb collision. Hence representing a situation approximating an experiment with a high resolution in the collision energy, see Refs. [9, 58]. Figure 5.5e shows the thermal rate coefficient obtained by integrating the cross

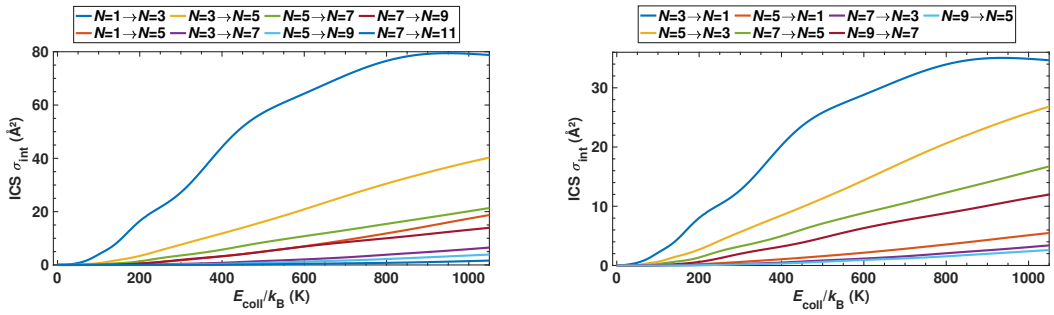

(a) (b)

Figure 5.4: Calculation results of the state-to-state excitation (a) and de-excitation (b) inelastic integral cross section (ICS) at collision energuies up to 1100 K.

sections over a Maxwell-Boltzmann distribution of velocities at the relevant temperature. In this energy range marked variations are exhibited by the cross sections which are attributed to scattering resonances. The narrow features manifest themselves in the rate coefficients in the experiments at high energy resolution (Figure 5.5c), while they are completely smoothed out in the rate coefficients under thermal conditions (Figure 5.5e). The physical origin of the narrow resonances in the cross sections should be linked to the rather strong ionic interactions which drive the present dynamics. The observed resonances could be shape resonances, trapping the system intermittently in a metastable state behind the centrifugal barrier. Additionally, the rotational structure of the isolated molecular target is distorted by the strong coupling between scattering channels due to long-range ion-neutral interactions creating virtual excitations to excited rotational states (Feshbach resonaces) which can be populated during a short time interval during the collisional events. The short lifetimes of the observed resonances indicated by their narrow widths are producing rather limited contributions to the thermal rate coefficients, thus would not translate into observable increases of the overall collision rate over the range of energies of interest studied in thermal experiments. Figure 5.5b shows the rotational de-excitation cross sections and rate coefficients (5.5d, 5.5f) across the same range of collision energies. It has to be noted that rotational excitation at these low collisions energies are energetically forbidden. Pronounced modulations are again show up in the cross sections pointing to scattering resonances. At, e.g., the one observed in the $N = 2 \rightarrow N = 0$ channels around $E_{coll}/k_B = 5\,mK$ and similar strong resonances even manifest themselves in the thermal averaging in Figure 5.5f. The overall de-excitation rate coefficients are small with $k < 10^{-11}\,cm^3 s^{-1}$ in the energy range shown and in particular well below the Langevin limit for this system.

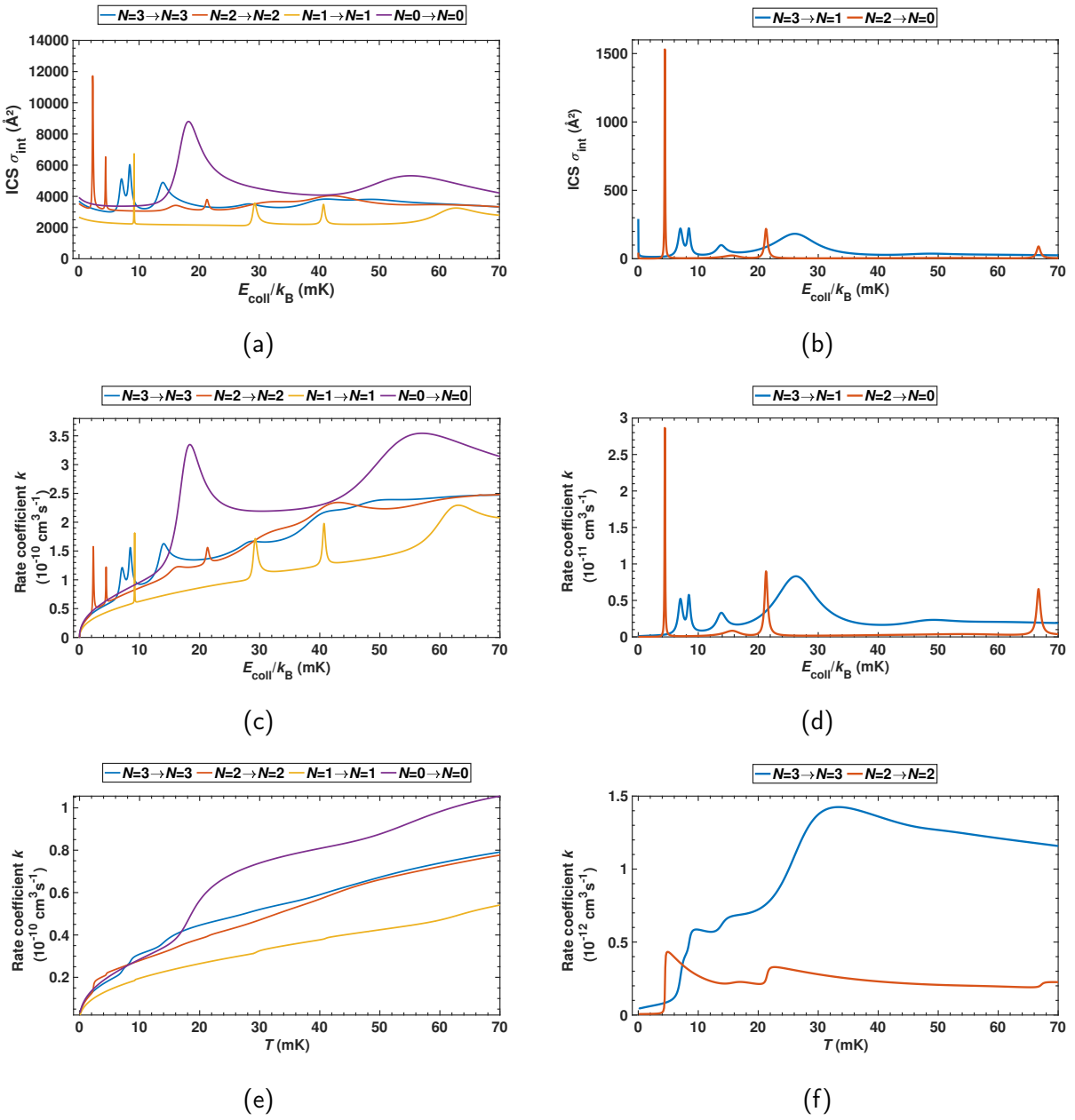

Figure 5.5: The left column presents rotationally elastic integrated cross sections (ICS) (a), rate coefficients at an infinitely small spread of of collision energies (c) and thermal rate coefficients (e) for $N_2^+ + Rb$ ($^2S_{1/2}$) at low collision energies up to 70 mK. The right column presents rotationally de-excitation integrated cross sections (ICS) (b), rate coefficients at an infinitely small spread of of collision energies (d) and thermal rate coefficients (f) for $N_2^+ + Rb$ ($^2S_{1/2}$) at low collision energies up to 70 mK.

5.3 Modeling ion losses from radiative association paths

Radiative association was found to be a dominant process in recent findings of atomic collision systems like $Ca^+/Ba^+/Sr^+$-Rb [27, 30, 38]. In the scope of this work, the questions arose

if N_2^+ and Rb form bound states, which are detectable in the experiment. They can cause significant trap losses and can be formed in radiative transitions to a charge - transfer state and hence reduce the possible yield of non - adiabatic charge exchange in the experiment. The collaboration with Gianturco *et al.* [103] presents a semi - quantitative modeling for the possible event of radiative association (RA) reactions in this work's hybrid trap system. P. Villarreal and T. González-Lezana performed the calculations based on the PESs of Yurtsever. Two types of processes shall be named to describe radiative association. The 'vibrational' RA path produces a triatomic ion in the same electronic state by associative recombination of the initial partners N_2^+ $(^2\Sigma_g) + Rb$ $(5s)$ $(^2S_{1/2})$ and the 'vibronic' RA path involves a transition to a different electronic state. This state has to be asymptotically connected to the charge - transfer products N_2 $(X^1\Sigma_g) + Rb^+$ $(4p^6)$ $(^1S_0)$.

$$N_2^+(X^{+2}\Sigma_g, \nu = 0) \; + \; Rb \; (5s) \; (^2S_{1/2}) \rightarrow [N_2Rb]^{+*} + \hbar\omega, \tag{5.15}$$

$$N_2^+(X^{+2}\Sigma_g, \nu = 0) \; + \; Rb \; (5s) \; (^2S_{1/2}) \rightarrow [N_2Rb]^{+} + \hbar\omega. \tag{5.16}$$

The 'vibrational' process forms an ionic triatomic complex in the initial, excited electronic state, while the 'vibronic' process produces the triatomic bound species in the ground electronic state with the dissociation limit corresponding to N_2^+ $(^1\Sigma_g)$ and Rb^+ $(^1S_0)$ (CT products). To simplify the investigation and keep the work related to the experiment, one combination was selected to represent the most abundant electronic states in the experiment, namely the one corresponding to the energetically lowest final channel after the CT reaction N_2 $(X^1\Sigma_g) + Rb^+$ $(4p^6)$ $(^1S_0)$. An accurate description of the atom / ion interaction forces allows for a simple modeling of the RA mechanism, utilising the most significant paths for relative approaches between the partners, namely the collinear ($\Theta_{N_2^+-Rb} = 0°$) configuration and the T - shaped ($\Theta_{N_2^+-Rb} = 90°$) configuration. This advantage stems from the smooth evolving differences in the well depths for both systems over the change of the angular variable $\Theta_{N_2^+-Rb}$ from 0° to 90°. RA probabilities and cross sections were obtained from these two extreme points by angular averaging over a polynomial expansion of the 1d results (see section 5.2.1). Different anisotropic features of the final PESs seem to play a significant role when calculating the transition moment matrix elements for the two dissipative paths. The contribution of the T - shaped and linear orientations can contribute to the 'vibrational' process final state. Under the experimental conditions given in Ref. [4], the presented calculations following a fairly simple picture of the physical process considered, but based on a structural data obtained from realistically accurate *ab initio* methods, reveal the 'vibrational' RA molecular ion loss process to be comparatively negligible with a rate coefficient of maximal $2 \times 10^{-21}\,cm^3\,s^{-1}$. The 'vibronic' process is exclusively characterised by the interaction potential corresponding to the collinear configuration. The new partners in the complex would now be the N_2 $(X^1\Sigma_g)$ neutral molecule and the ionised rubidium atom Rb^+ $(4p^6)$ $(^1S_0)$ emanated from the charge - transfer reaction in the trap. With an extended energy gap of 11.71 eV, the RA cross section will be enhanced due to the ω^3 scaling factor of the emission rates. However, through the relevant

dipole moment, the size of the overlap integrals between the initial continuum states and the final bound states is small. This is due to the final charge - transfer potential behaves in the opposite way from the initial channel potential, since now the deepest well appears for the collinear geometry of the interaction while the T - shaped potential has the shallowest well. It was found that for the high contributing collinear R_8 branch of the rovibrational spectra (for details see [103] section 3), the squares of the overlap integrals for the vibronic RA process are nine orders of magnitude lower than the ones corresponding to the 'vibrational' RA process. Including the photon energy factor in this results turns the tables and at the end the final associative rates for the 'vibronic' process were about six orders of magnitude larger than the 'vibrational' ones. Even though the process in the experiment discussed in Ref. [4] and in this work show trap loss mechanisms at a rate coefficient around $\approx 1.6 \times 10^{-9}\,\mathrm{cm^3\,s^{-1}}$, which is much faster than the RA rate coefficients at $\approx 1.15 \times 10^{-14}\,\mathrm{cm^3\,s^{-1}}$ for the 'vibronic' process, the RA process can occur. Conclusively all RA channels involving any electronically excited state of the product N_2 are considered to have a much smaller cross sections compared to the discussed electronic ground state. The lowest electronic configuration of the reactants also used in [4] and undergoing the lowest CT electronic state of the exothermic products is highly probable to take part in an initial modeling of the RA process in the trap. As the final conclusion, the calculated RA reaction rates are several orders of magnitude smaller than the experimentally measured rate coefficients attributed to non - adiabatic CT, hence for the discussed molecular collision system the nonadiabatic CT dynamics overshadow the radiative processes compared to previous studied atomic systems [27, 30, 38].

6 Charge - transfer (CT) collision experiments with molecular ions

Previous chapters explained the theoretical concepts, the experimental setup, the atom shuttling simulations and explored the rate coefficients for rotational state - changing collisions and radiative association in N_2^+ - Rb theoretically. This chapter discusses collision experiments between the sympathetically cooled molecular ions N_2^+, O_2^+ and N_2H^+ and the stationary Rb atom cloud as well as the shuttling Rb atom cloud. First, the previous work of Hall *et al.* [4] on charge - transfer (CT) collisions between sympathetically cooled molecular N_2^+ and a stationary cold Rb atom cloud will be reviewed. Second, the work of Eberle [8] on the CT collision experiments between O_2^+ and a stationary cold Rb atom cloud is discussed, followed by the theoretical concepts of the electronic structure calculations, the quantum scattering calculation and the classical dynamics calculations. At the time of writing, no theoretical work on the $N_2H^+ + Rb$ experiments was available, hence only the experimental work and the results are presented.

6.1 Previous molecular - ion experiments

Previous experiments with cold molecular ions include $Ca^+ + CH_3F$ at collision energies as low as 2 K with single particle resolution [1], the molecular - anion molecule reaction $NH_2^- + H_2$ [2], studies on changing of the rotational state [110], reaction of trapped $OH^- + Rb$ [56] at relatively high temperatures (200 K) and the previous work of Hall *et al.* [4, 10] on the prototypical system of $N_2^+ + Rb$ and Eberle [8] with his work on $O_2^+ + Rb$. Both the works, of Hall and Eberle were conducted on the present experimental setup with a stationary atom cloud. The molecular orbital diagrams of N_2 and O_2 are presented in Figure 6.1. During ionisation, one electron is taken away from the HOMO leaving N_2^+ in a $^2\Sigma_g^+$ state and O_2^+ in a $^2\Pi_{1/2}^+$ state.

N_2^+ results by Hall *et al.*

In his work [4, 10], Hall measured the rate constant for charge transfer (CT) of $N_2^+ + Rb$ as a function of the average collision energy (see Figure 6.2a) and the rate constant as a function of population of Rb in the $(5p)\ ^2P_{3/2}$ state (see Figure 6.2b). He found the

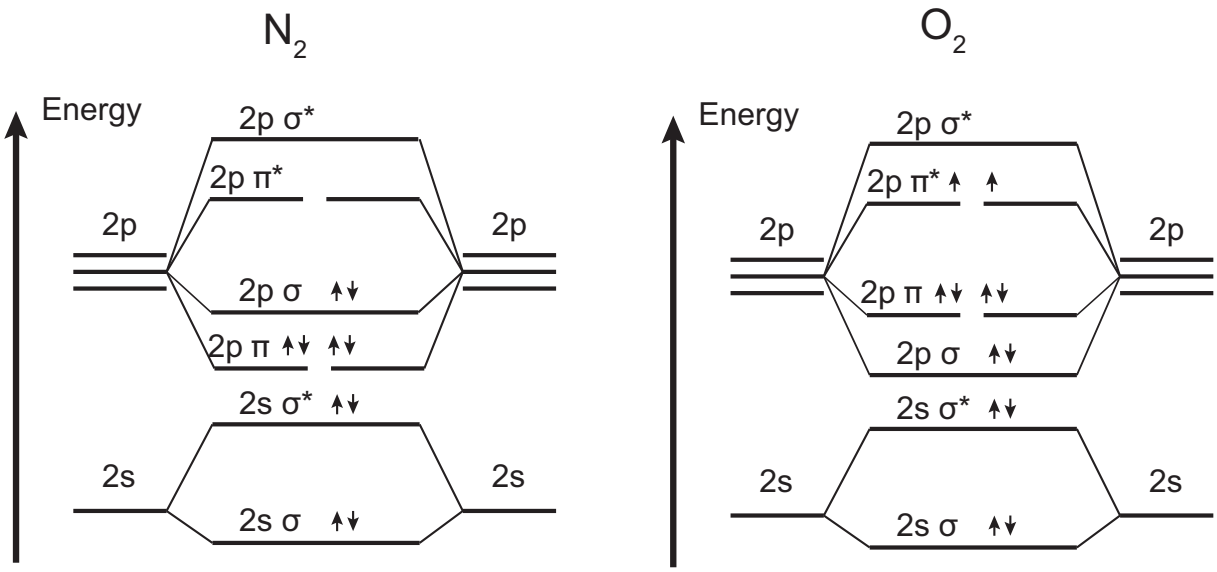

Figure 6.1: Molecular orbital energy diagrams. On the left side for N_2 and on the right side for O_2. From these diagrams the lower ionisation potential for the molecular oxygen can be explained, since the electron will be stripped from an anti - bonding orbital, whereas for molecular nitrogen it will come from a bonding orbital.

channel - averaged rate constant to be $k \approx 2 \times 10^{-9}\,\mathrm{cm^3\,s^{-1}}$, but his measurement with different excited state populations showed an increase of the CT rate constant with the fraction of rubidium atoms in the $(5p)\ ^2P_{3/2}$ state. A fit to this data yielded a rate constant of $k_p = 2.4(13) \times 10^{-8}\,\mathrm{cm^3\,s^{-1}}$ for excited state Rb $^2P_{3/2}$ and an upper bound of $k_s \leq 2 \times 10^{-10}\,\mathrm{cm^3\,s^{-1}}$ for ground state Rb $^2S_{1/2}$. The calculated Langevin rate constant for $N_2^+ + \mathrm{Rb}\ (5s)\ ^2S_{1/2}$ is $k_L^s = 3.5 \times 10^{-9}\,\mathrm{cm^3\,s^{-1}}$ which is more than one order of magnitude larger than the measured upper bound. Hall explained this discrepancy by inefficient charge transfer, in view of the fact that the energetically closest product channel would require a re-organisation of the electron configuration and the very large energy gap between the entrance channel and the exit channel to form neutral N_2 in the C state. For the reactions measured between N_2^+ and Rb atoms in the $(5p)\ ^2P_{3/2}$ state, the rate constant k_p was found to be four times larger than the Langevin rate constant $k_L^p = 6.6 \times 10^{-9}\,\mathrm{cm^3\,s^{-1}}$. This result was rationalised in terms of an extended rate model presented in Figure 6.2c. Often the Langevin rate model constitutes an upper bound for ion - neutral reactions given a charge - induced dipole interaction, thus the rate constant is collision - energy independent. Rb* has an anisotropic charge distribution [111], hence it generates a permanent electric quadrupole moment. The predictions of this model are presented in Figure 6.2c and compared to the experimental data in the inset of the figure. Its agreement with the observed rate coefficients demonstrates the need for an extension of Langevin theory to explain the dynamics in this system.

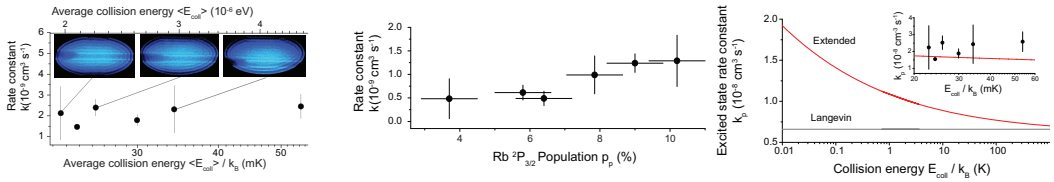

(a) (b) (c)

Figure 6.2: (a) Measured rate constant for $N_2^+ + Rb$ as a function of the average collision energy. Each data point was averaged over three independent measurements, the error bars indicate the statistical error (2σ). The insets show Coulomb crystals corresponding to the data points indicated. (b) Rate constant as a function of excited state population for Rb in the $(5p)\ ^2P_{3/2}$ state. (c) Calculated CT rate constant in the $N_2^+ + Rb$ $(5p)\ ^2P_{3/2}$ channel as a function of collisional energy. The grey line only includes the charge induced - dipole interaction (Langevin theory) and the red line is an extended model also including charge permanent - quadrupole interactions for the calculation of the rate constant. The inset shows the extended model compared to the measured experimental result of (a) scaled to 100 % Rb $(5p)\ ^2P_{3/2}$ population. (These figures are adapted with permission from Ref. [10].)

O_2^+ results by Eberle

Eberle states in his work on O_2^+ - Rb [8] that he expects the reaction behaviour due to the similar long - range part of the potential to be equivalent to $N_2^+ + Rb$. It should be noted that at the time of the submission of his thesis, the theoretical investigation was not finished. The results of his work will be discussed more detailed in section 6.4 and compared with theory and the collision - energy dependent charge - transfer results .

6.2 Theoretical methods for N_2^+ and O_2^+

Adapted from Ref. [112], the following subsection summarises the background on the theoretical calculation methods. The electronic structure calculations and the quantum scattering calculations were performed for N_2^+ and O_2^+ by M. Tomza, while the classical dynamics calculations are confined to N_2^+ and were done by D. Koner and M. Meuwly.

6.2.1 Electronic structure calculations

The electronic structure calculations for the potential energy surfaces (PESs) for the ground and excited electronic states are based on a multireference configuration interaction method restricted to single and double excitations (MRCISD). The starting point for these calculations was the multi - configurational self - consistent field method (MCSCF, see Ref. [113]). The complete active space reference wave functions included all atomic valence orbitals (both binding and antibinding molecular orbitals). Nitrogen and oxygen atoms were described using

the augmented correlation - consistent polarised core - valence quintuple - ζ quality basis sets (aug - cc - pCV5Z) [114]. For Rb, the small - core relativistic energy - consistent pseudo potential ECP28MDF to replace the inner - shells electrons [115] was employed which includes scalar relativistic effects. The remaining electrons were described with the large [14s14p7d6f1g] basis set [116]. The electronic structure calculations were performed with the MOLPRO package of *ab initio* programs [104]. On a 2d grid in Jacobi coordinates (R, Θ) for a fixed N - N distance $r = 2.074$ a.u., corresponding to the equilibrium bond length in N_2^+, *ab initio* energies were calculated for two excited $^3A'$ electronic states of RbN_2^+. Here, R is the distance form the center of mass of N_2 to Rb, r the distance between the two N atoms and Θ the angle between $\vec{r}$ and $\vec{R}$. The lower surface dissociates towards N_2 $(C^3\Pi_u) + Rb^+$ and the upper PES adiabatically correlates with the N_2^+ $(X'^2\Sigma_g^+) + Rb$ $(^2S_{1/2})$ asymptote. For the two coupled $^3A'$ electronic states, 2d analytical PESs were constructed from the *ab initio* energies using the reproducing kernel Hilbert space (RKHS) technique [117, 118]. For the radial dimension (R), a reciprocal power decay kernel was used which smoothly decays to zero $\propto \frac{1}{R^4}$ and gives the correct long - range behaviour for ion - neutral type interactions. For the angular degree of freedom, a Taylor spline kernel was used.

6.2.2 Quantum scattering calculations

The rate constants (non - adiabatic, non - radiative and charge - transfer) were calculated for 1d - cuts through two crossing potential energy surfaces transferred to the diabatic representation. The coupled - channels equations for the nuclear motion were solved using a renormalised Numerov propagator [119] with a step - size doubling as implemented in Ref. [120]. The wave function ratio was propagated to large interatomic separations, where the K and S matrices were extracted by imposing the long - range scattering boundary conditions in terms of Bessel functions. The inelastic rate constants were obtained from the elements of the S matrix summed over relevant partial waves l and thermally averaged.

6.2.3 Quasiclassical - dynamics calculations for N_2^+

A detailed discussion of the quasiclassical - trajectory (QCT) method can be found in Ref. [121] based on Refs. [122, 123]. Utilizing a sixth - order symplectic method, Hamilton's equations of motion were solved with initial conditions for a trajectory sampled by applying a standard Monte Carlo sampling method following [122]. A room - temperature Boltzmann distribution was used to sample the rotational states of N_2^+. As for the impact parameter b, stratified sampling [122] was used. Conservation of total angular momentum and total energy during numerical integration was ensured by employing two time steps (Δt): From the beginning of the trajectory until it reaches $R < 35$ a.u., $\Delta t = 0.6$ fs was constant and for the first time the trajectory reaches $R < 35$ a.u. until the end $\Delta t = 0.05$ fs. Charge transfer rates due to nonadiabatic transitions were calculated within a modified Landau - Zener formalism [124–127],

which depends on the adiabatic potential energies of the states involved in the transition and the time t_c, by applying the trajectory surface hopping (TSH) method [128]. The transition probability from state j to state k was expressed as

$$P_{LZ}^{j\to k} = \exp\left(-\frac{\pi}{2\hbar}\sqrt{\frac{\Delta V_{jk}^a(x(t_c))^3}{\frac{d^2}{dt^2}\Delta V_{jk}^a(x(t_c))}}\right), \tag{6.1}$$

where $\Delta V_{jk}^a(x)$ is the adiabatic energy difference between those states. Transition probabilities were calculated and momentum corrections along different degrees of freedom were applied [129] whenever a local minimum $\Delta V_{jk}^a(x)$ was reached after a successful hop to keep the total energy and angular momentum conserved for a given trajectory. The rate constants at a particular collision energy (E_{coll}) were calculated following

$$k = \sqrt{\frac{2E_{coll}}{\mu}}\pi b_{max}^2 \frac{N_r}{N_{tot}}, \tag{6.2}$$

with μ denoting the reduced mass of the collision system, N_r the number of reactive (charge transfer) trajectories (weighted by stratum statistical weights), N_{tot} the total number of trajectories and b_{max} the maximum impact parameter for which a charge transfer reaction can occur.

6.3 The $N_2^+ + Rb$ system

CT in generally is considered most efficient if it is near resonant, i.e., if the entrance channel and the possible product channels are energetically close and if there is no extensive reorganization of the electron configuration in the molecule [130]. Figure 6.3 illustrates the asymptotic energies of the entrance and the possible product channels of $N_2^+ + Rb$ CT collisions. The two relevant entrance channels are Rb in the electronic ground state $^2S_{1/2}$ and in the first excited state $^2P_{3/2}$ colliding with N_2^+ in the electronic ground state. Possible product channels are Rb^+ ions in the $^1S_0$ ground electronic state and neutral N_2 molecules in a range of electronically excited states, in particular low lying Rydberg states. Judging from the density of possible exit channels energetically close to the $N_2^+ + Rb$ ($^2P_{3/2}$) asymptote it could be expected that the CT rate coefficient should be more efficient. Spearheaded by the work of Hall [4, 91], an extended investigation was conducted by applying the new dynamic mode of the hybrid trap introduced in this work to look closer at collision - energy dependent CT rate coefficients.

6.3.1 Methods

Loading the N_2^+ ions and sympathetically cooling them with the Coulomb crystal was described in section 3.4.2. For the state - dependent rate coefficient measurements, the rubidium atoms in the a stationary MOT were overlapped with the ions. The populations of the $S_{1/2}$ ground state and the $P_{3/2}$ excited state were controlled by the intensity of the atom - cooling laser and

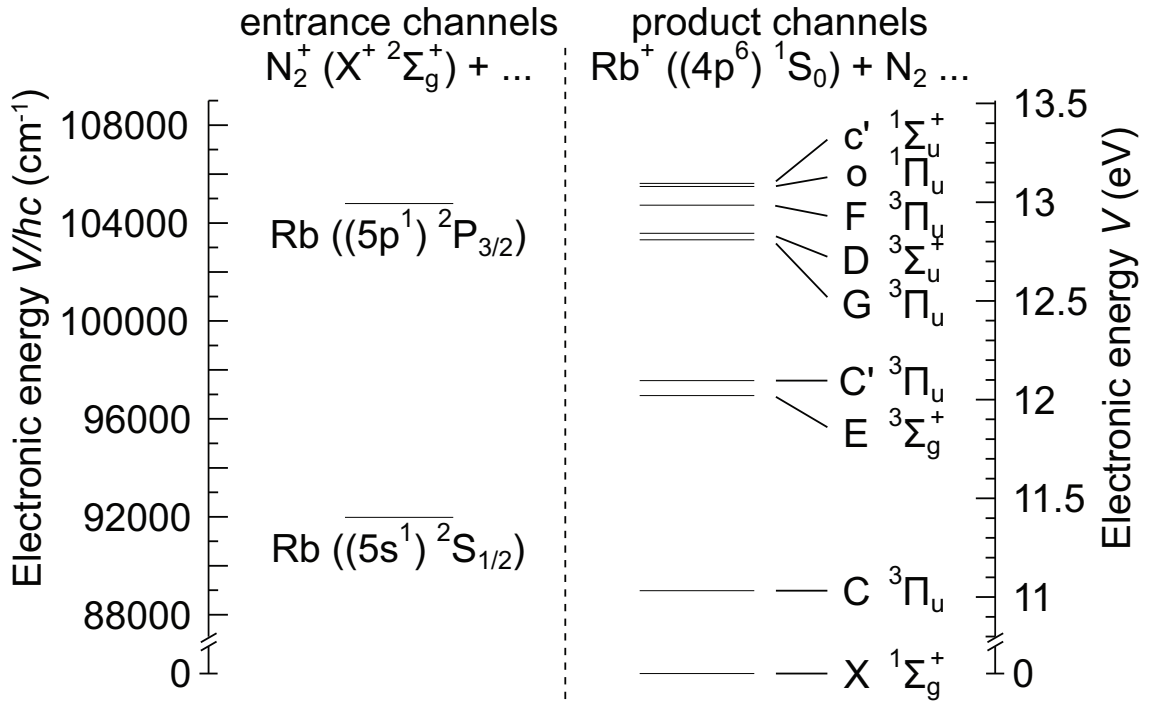

Figure 6.3: Asymptotic energies of the entrance and possible product channels for $N_2^+ + Rb$ favourable charge-transfer (CT) collisions. The molecular ions can undergo CT with Rb in either its $^2S_{1/2}$ ground state or $^2P_{3/2}$ excited state populated by laser cooling in the MOT.

the detuning from the atomic resonance Rb D II. Collision-energy dependent rate coefficient measurements were started by loading an off-center atom cloud not overlapping with the loaded molecular ions. Depending on the experiment, the shuttling parameters were set and the atom cloud started to move. The EMCCD camera was set to take pictures every 5 s until there were no N_2^+ ions left. Additionally to the pictures, all available information was stored in a separate Matlab file (including laser frequencies, laser lock status, etc.). Before and after each measurement, atom-cloud velocities were determined and laser intensities were recorded, especially since for the dark atom shuttling there was no fluorescence of the atoms while interacting with the ions which ensured pure $(5s)\ ^2S_{1/2}$ state collisions. Five different collision energies were chosen to be measured. For each energy and shuttling mode 15 independent measurements were recorded. A measurement run was about 5 min. The data analysis is presented in Appendix A.4 where all formulas and uncertainty calculations can be found.

6.3.2 Charge - transfer (CT) rate coefficients: Results and discussion

State - dependent charge - transfer rate coefficients

In the experiments shown in Figure 6.4a, the population of Rb $(5p)\ ^2P_{3/2}$ was tuned between 7.53(59) % and 12.17(85) % resulting in a linearly increasing rate coefficient k from $2.183(64) \times 10^{-9}\,cm^3\,s^{-1}$ to $2.599(41) \times 10^{-9}\,cm^3\,s^{-1}$. The expected rate coefficients, based on Langevin theory, would be k_p^L=$6.1 \times 10^{-9}\,cm^3\,s^{-1}$ for the $^2P_{3/2}$ state and for the $^2S_{1/2}$ state k_s^L=$3.5 \times 10^{-9}\,cm^3\,s^{-1}$. To proof the model of the extended interaction potential, including the charge - induced dipole and charge - permanent quadrupole interaction, in this experiment, a linear increase following Equation (A.10) must be observed. During fitting both parameters $k_{p,stat}^{exp}$ and $k_{s,stat}^{exp}$ were left unbound and the fit yielded a rate coefficient $k_{p,stat}^{exp}$=$1.7(6) \times 10^{-8}\,cm^3\,s^{-1}$ for the excited state and $k_{s,stat}^{exp}$=$1.6(3) \times 10^{-9}\,cm^3\,s^{-1}$ for the ground state. The upper bound for the rate coefficient measured by Hall for the ground state was $k_s \leq 2 \times 10^{-10}\,cm^3\,s^{-1}$. The new value for k_s is one order of magnitude larger and replaces the upper bound, but surprisingly it is two times slower than the rate coefficient $k_s^L = 3.5 \times 10^{-9}\,cm^3\,s^{-1}$ predicted by Langevin theory.

Collision - energy - dependent charge - transfer rate coefficients

The collision - energy dependent charge - transfer rate coefficient was measured with the moving atom cloud. The two different modes of the moving atom cloud, bright and dark, were used to specifically measure the reaction rate coefficient with rubidium in the $(5p)\ ^2P_{3/2}$ state or the $(5s)\ ^2S_{1/2}$ state, respectively. Figure 6.4b illustrates the state dependent CT rate coefficients as a function of the collision energy. Data for the excited state $(5p)\ ^2P_{3/2}$ are depicted as ▲ and for the the ground state $(5s)\ ^2S_{1/2}$ as ▼. The theoretical Langevin rate coefficients are indicated for the collisions of Rb $^2P_{3/2}$ (solid orange line) and $^2S_{1/2}$ (solid blue line) with N_2^+. The dash - dotted blues line depicts the fit for the Rb $(^2S_{1/2})$ rate coefficient yielding a result of $k_s^{exp} = 1.5(2) \times 10^{-9}\,cm^3\,s^{-1}$. This agrees well with the rate coefficient of the population dependency measurement. The rate coefficient for the Rb $(^2P_{3/2})$ reaction is fitted with a model using an extended interaction potential incorporating the charge - induced dipole and charged - permanent quadrupole interactions (see Appendix A.3).

Specific Q and α values

Rubidium in the excited state has two different polarisabilities as presented in Equation (2.5). The polarisability $\alpha_0 = 127.0(15)\,Å^3$ from Ref. [131] was used. The orange dash - dotted line in Figure 6.4b represents a fit of the data for $N_2^+ + Rb$ $(^2P_{3/2})$ to an extended interaction potential, incorporating the model described in Appendix A.3, yielding a quadrupole moment of $Q = 15.45(1.22)$ a.u for the Rb $(^2P_{3/2})$ state. *Ab initio* calculations at the MRCISD level give

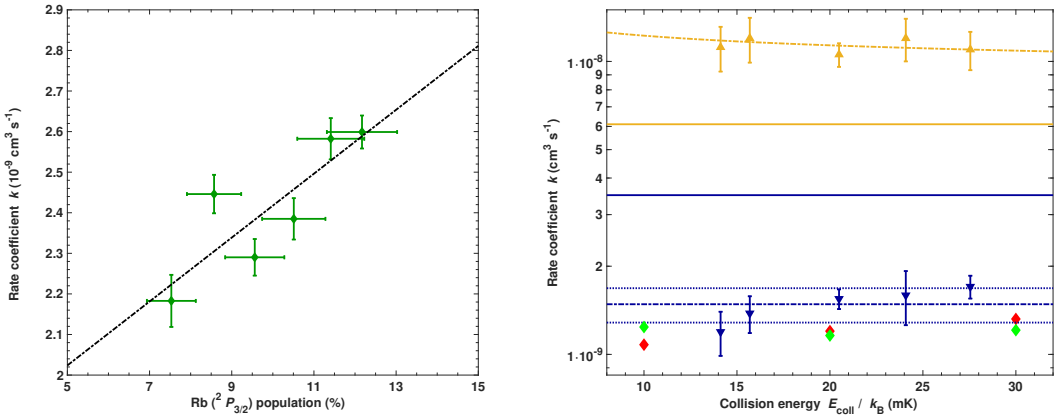

(a) (b)

Figure 6.4: Illustrated are the measured CT rate coefficients for the state - dependent experiments (a) and the collision - energy - dependent measurements (b). (a) Measured CT rate coefficients for N_2^+ are indicated with ● and the black dash-dotted line depicts the fit following Equation (A.10). The fit yields $k_{p,\mathrm{stat}}^{\mathrm{exp}}$=1.7(6) $\times 10^{-8}\,\mathrm{cm^3\,s^{-1}}$ and $k_{s,\mathrm{stat}}^{\mathrm{exp}}$=1.6(3) $\times 10^{-9}\,\mathrm{cm^3\,s^{-1}}$. (b) Collision energy dependent rate coefficients for $N_2^+ + \mathrm{Rb}\ (^2P_{3/2})$ ▲ and for $N_2^+ + \mathrm{Rb}\ (^2S_{1/2})$ ▼. The theoretical Langevin rate coefficients for the reaction of Rb $^2P_{3/2}$ (solid orange line) and $^2S_{1/2}$ (solid blue line) with N_2^+ are k_p^{L}=6.1 $\times 10^{-9}\,\mathrm{cm^3\,s^{-1}}$ and k_s^{L}=3.5 $\times 10^{-9}\,\mathrm{cm^3\,s^{-1}}$. The dash - dotted blues line depicts the fit for the Rb $(^2S_{1/2})$ rate coefficients. The rate coefficient for the Rb $(^2P_{3/2})$ reaction is fitted with a model using an extended interaction potential incorporating the charge - induced dipole and charged - permanent quadrupole interactions (see A.3). Theoretical CT rate coefficients computed by classical trajectory and quantum scattering calculations are indicated in red and green diamonds, respectively.

a value of $Q = 12.9$ a.u.. Using this quadrupole moment at a collision - energy E_{coll}/k_B=20 mK and with an excited state fraction of 11(2) %, a rate coefficient $k_p(N_2)$=1.1(1) $\times 10^{-8}$ cm^3 s^{-1} is obtained for $N_2^+ + Rb$ ($^2P_{3/2}$).

Theoretical potential energy curves

Figure 6.5a shows cuts through the 3d PES of the collision system with the Rb moiety at an infinitely large distance from the molecule. The potential curves of both singlet and triplet electronic states of the N_2 molecule are shown as a function of bond length r. The relevant cationic ground states are illustrated as solid green lines and the cationic curves shifted by the ionisation potential of Rb by solid blue lines. These correspond to the relevant energies of the lowest entrance channel for the CT reaction. The dashed lines indicate the curves obtained by adding the shift by the excitation to the Rb ($^2P_{3/2}$) state. The crossing points indicated by circles between the shifted ionic curves and the neutral curves close to the molecular equilibrium geometry represent opportunities for non - adiabatic transitions (CT). The doublet electron - spin character of the collision partners allow for collisions in either the singlet or the triplet PES. In Figure 6.5b, a cut of the adiabatic PES close to the computed minimum energy path for CT in the singlet channel at a linear collision geometry is shown. An electronic barrier arises from an avoided crossing, asymptotically connecting to the neutral N_2. Low collision energies of the order $\approx 1 \times 10^{-2}$ cm^{-1} prevent possible CT transfer reaction along this coordinate, because they will not be able to overcome the existing barrier with a height exceeding 5000 cm^{-1}. Figure 6.6 shows the cuts of the triplet PES of the collision system for different N_2 - Rb orientation angles Θ along the N_2 - Rb coordinate R. At $\Theta = 0$ (linear geometry, Figure 6.6a), the entrance channel with symmetry $^3\Sigma^+$ intersects with a $^3\Pi$ surface which asymptotically connects to the C $^3\Pi$ state of N_2. For all non - linear geometries (Figures 6.6b, 6.6c, 6.6d), the $^3\Pi$ surface splits into two components, A' and an A''. The entrance channel surface in this symmetry is also A' with which the A' surface undergoes avoided crossings. The non - adiabatic coupling between them, as indicated by the separation of the resulting adiabatic surfaces at crossing points, increases with increasing orientation angle Θ.

Quasiclassical trajectory simulation and quantum dynamics calculations

A quantitative insight into the non - adiabatic dynamics is gained by the quasiclassical trajectory simulations and quantum scattering calculations of the CT. The theoretical details of the employed modified Landau - Zener formalism on the two coupled 2d A' surfaces of Figure 6.6 for modeling the CT are explained in section 6.2. Rate coefficients for collision energies of E_{coll}/k_B = 10, 20 and 30 mK (red diamonds in Figure 6.4b) are calculated from 5000 independent trajectories for 2d - dynamics along the distance R between the center - of - mass of N_2^+ and Rb and the orientation angle Θ with the bond length r hold fixed at of the equilibrium value of N_2^+. Direct (Figure 6.7a) and indirect (Figure 6.7b and 6.7c) reactive CT

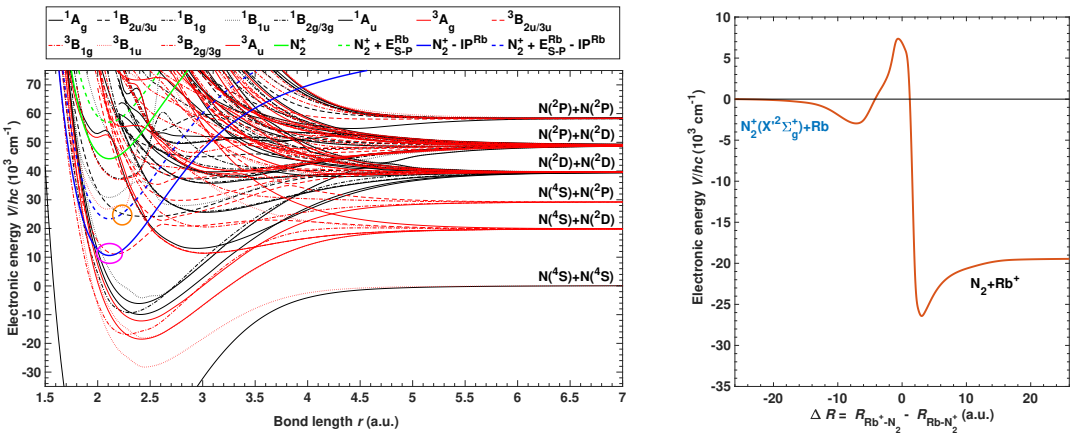

(a) (b)

Figure 6.5: (a) Electronic states for N_2 and N_2^+ as a function of the bond length r. The cationic ground state is depicted as the solid green curve, the cationic curves shifted by the ionisation potential of Rb by the solid blue line. Offsets by the excitation energy of Rb ($^2P_{3/2}$) are illustrated by dashed lines. Circles indicate crossing points for non - adiabatic transitions between the surfaces. (b) Reaction pathways in linear collision geometry. Cuts of the PES along reaction coordinates for charge transfer in the linear collision geometry of the singlet channels of Rb($^2S_{1/2}$) reacting with N_2^+. See text for discussion.

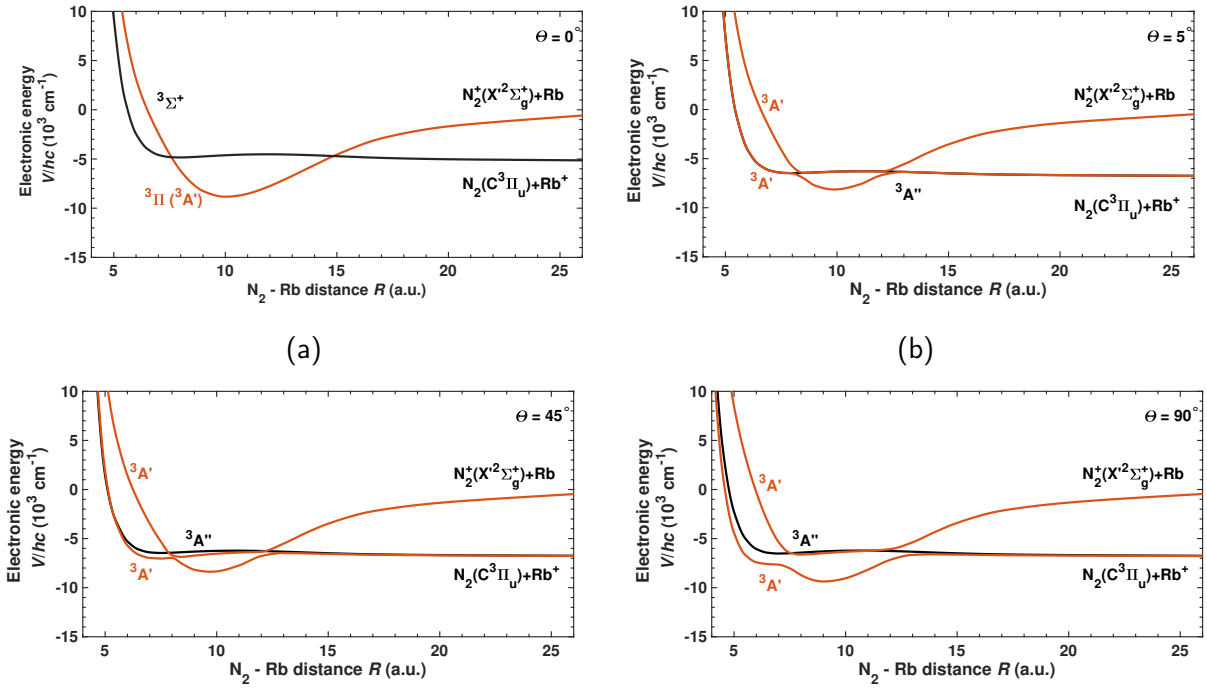

(a) (b)

(c) (d)

Figure 6.6: Cuts of the PES in the triplet channel for CT reactions of Rb ($^2S_{1/2}$) with N_2^+ at different orientation angles θ. R denotes the N_2 - Rb separation coordinate.

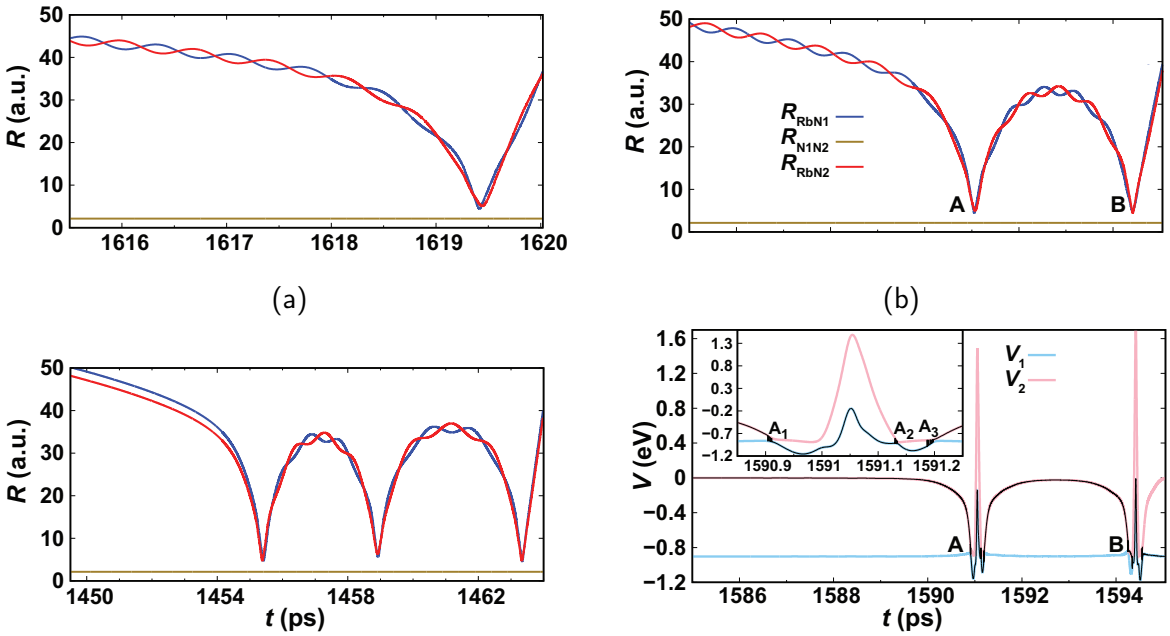

Figure 6.7: Direct and indirect CT trajectories of the quantum dynamics calculation. Trajectories are represented in terms of the N_2 - Rb distance R in dependence of simulation time t with panel (a) presenting a direct trajectory, while panels (b) and (c) show indirect trajectories for multiple collisions. (d) shows the further analysis of the trajectory of (b) representing the change in potential energy as a function of t. The energy path is shown as a black line. Multiple switching between surfaces can be seen in the hopping regions, which is depicted in the inset for the first collision (labeled as 'A').

trajectories were classified according to the collision time defined as the time elapsed between the first and last time a trajectory satisfies a geometrical criterion (sum of the three interatomic distance to be smaller than 35 a.u.). Figure 6.8b shows a scatter plot of collision time as a function of impact parameter at $E_{\mathrm{coll}}/k_{\mathrm{B}} = 20\,\mathrm{mK}$. Out of 5000 computed trajectories 4374 show CT, where 3294 are direct with collision times of $\approx 0.5\,\mathrm{ps}$ and 1080 are indirect. From the 626 ending as $N_2^+ + \mathrm{Rb}$, 67 are flyby or no collision, 513 are direct and 46 are indirect. The indirect trajectory shown in Figure 6.7b is illustrated as projection onto the two PESs in Figure 6.8a. Despite low collision energy, large parts of the configurational space are sampled. Crossings of the trajectory between the two PESs are distributed along all values of Θ and concentrated at $R \approx 8\,\mathrm{a.u.}$ and 12 a.u.. This is expected from the 1d cuts through the PES shown in Figure 6.6. Over the duration of the dynamics, as indicated by the changing colours of the trajectory, multiple recrossings, which are labeled 'A' and 'B', occur in both direct and indirect trajectories between the surfaces. An outward trajectory ending up on the entrance surface after the first collision is intermittently trapped in the deep potential well. The collision energy has been redistributed along other degrees of freedom and dissociation of the complex is very unlikely on the studied timescales. In this case the trajectories recurrently show a pronounced roaming behaviour, i.e., the N_2 moiety is orbited by Rb at large distances several times (see Figure 6.8a). These trajectories may undergo several collisions. In the case where an outward trajectory ends up on the CT (lower) surface after transversing the outer crossing point, it is not able to return anymore due to the repulsive character of the lower PES in this region. The high, albeit not unit, efficiency of CT in this channel is explained by the distinct short-range topology of the two coupled surfaces and it is evidently clear that a long-range Langevin-capture picture cannot satisfy the complex short-range dynamics and its impact on the kinetics as observed in the experiments. To substantiate the insights of the classical dynamics, 1d quantum scattering calculations of the CT were performed at different orientation angles Θ. The quantum results for the CT rate coefficients averaged over all orientation angles Θ are indicated in Figure 6.4b as green diamonds and are in good agreement with both experimental and classical-dynamical results.

6.3.3 Conclusions

The cold CT dynamics of $N_2^+ + \mathrm{Rb}$ were explored in dependence of the excited state Rb $^2P_{3/2}$ population and as a function of collision-energy. Both experiments yield comparable results for the excited CT rate coefficient k_p, with $k_{p,\mathrm{stat}}^{\mathrm{exp}} = 1.7(6) \times 10^{-8}\,\mathrm{cm^3\,s^{-1}}$ for the state-dependent experiments and $k_p^{\mathrm{exp}} = 1.1(1) \times 10^{-8}\,\mathrm{cm^3\,s^{-1}}$ at $E_{\mathrm{coll}}/k_{\mathrm{B}} = 20\,\mathrm{mK}$ for the collision-energy dependent experiments. The experimental results for the reaction with ground state ($^2S_{1/2}$) Rb are $k_{s,\mathrm{stat}}^{\mathrm{exp}} = 1.6(3) \times 10^{-9}\,\mathrm{cm^3\,s^{-1}}$ for the state-dependent experiments and $k_s^{\mathrm{exp}} = 1.5(2) \times 10^{-9}\,\mathrm{cm^3\,s^{-1}}$ for the collision-energy dependent experiments. The results are corroborated by theoretical investigations employing quasiclassical trajectory simulations and

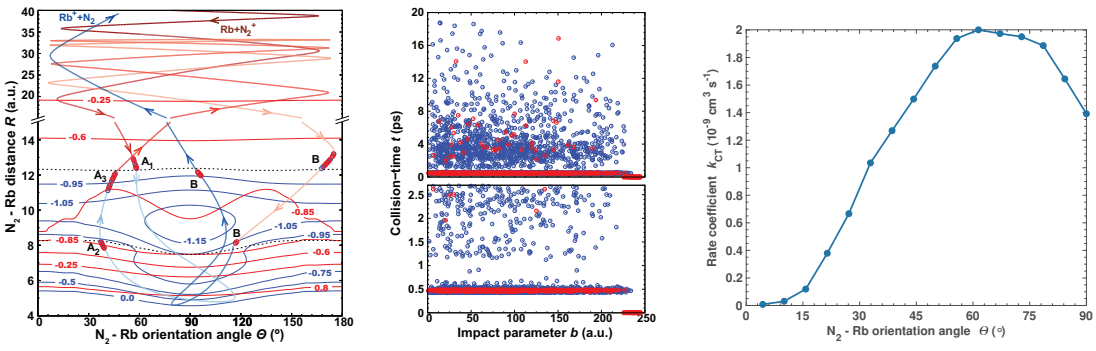

(a) (b) (c)

Figure 6.8: (a) Detailed dynamics of indirect CT trajectories (Figure 6.7b and 6.7d) illustrated as a projection onto the two coupled PESs. The contour diagrams of the two PESs are presented in solid red lines for the upper state and solid blue lines for the lower state and labeled in e V. Avoided crossing regions are depicted as dashed black lines. The trajectory path is shown in thick red and blue lines on the upper and lower surface, respectively. Simulation time progress is shown as a change of colour from light to dark (upper state) and dark to light (lower state) tones. Open circles in red and blue indicate inter-surface hops in regions labeled identical to Figure 6.7b and 6.7d. (b) Collision-time t independence of the impact parameter b at $E_{\text{coll}}/k_{\text{B}} = 20\,\text{mK}$. Blue circles depict CT and non-reactive trajectories are shown as red circles. The bottom panel shows a magnified view of the low-collision-energy region in the upper panel. (c) 1d quantum-scattering rate coefficient as a function of the N_2^+-Rb orientation angle Θ.

quantum dynamics calculations. The good agreement between experimental results and the two different theoretical treatments were presented in Figure 6.4b as red (classical trajectory) and green diamonds (quantum dynamics). From the comparison between theoretical investigation and the experimental results several conclusion can be drawn. First, the CT dynamics can be understood in classical terms. Distinct quantum effects (tunneling, zero - point motion) do not seem to play a major role apart from surface hopping taking the relative heavy masses of the collision partners and the collision energies into consideration. Second, the dynamics are adequately approximated in reduced dimensionality, i.e., Figure 6.8a in 2d and Figure 6.8c in 1d. It needs to be noted that an 1d treatment cannot reveal the roaming - type behaviour, which appears to be important for a fraction of the collisions. Third, in spite of the complex and dense electronic structure in the energy region of the entrance and exit channels (see Figure 6.5a), describing the CT in $N_2^+ + Rb$ ($^2S_{1/2}$) in terms of only two coupled PESs seems sufficient, justified in terms of the strong non - adiabatic couplings which happen around the crossing points between the two surfaces. CT dynamics do not appear to be affected by couplings to other states which show no crossings with the entrance channel in the energy region sampled by the experiments are expected to be considerably weaker.

6.4 The $O_2^+ + Rb$ system

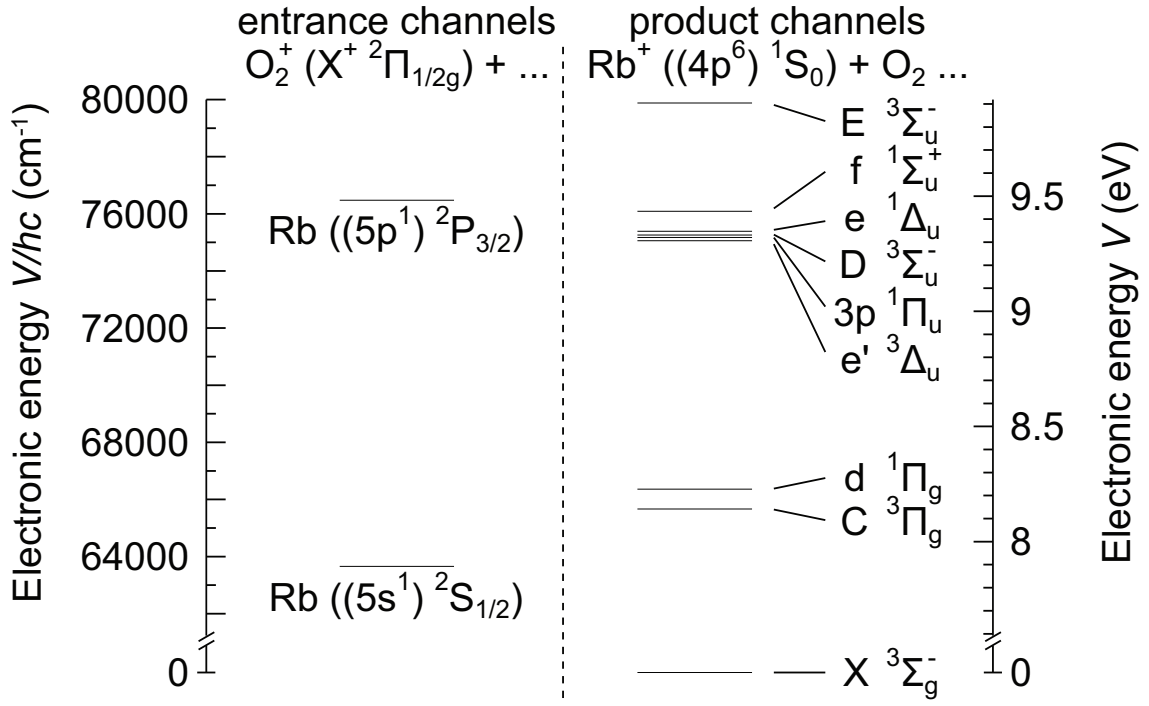

Figure 6.9: Asymptotic energies of the entrance and possible product channels of $O_2^+ + Rb$ favourable charge - transfer (CT) collisions. The molecular ions can undergo CT with Rb in either its $^2S_{1/2}$ ground state or $^2P_{3/2}$ excited state populated by laser cooling in the MOT.

Figure 6.9 illustrates the asymptotic energies of the entrance and near-resonant product channels of $O_2^+ + Rb$ with O_2^+ ions in their electronic ground state colliding with Rb atoms in either the $^2S_{1/2}$ ground or $^2P_{3/2}$ first excited electronic state. Compared to Figure 6.3, the high density of near-resonant product channels suggest a similar CT dynamics with Rb $^2P_{3/2}$ as was seen with $N_2^+ + Rb$ in section 6.3. An insight will be given in the following sections by investigation of the state-dependent CT rate coefficient and the collision-energy dependent CT rate coefficient.

6.4.1 Methods

The loading procedure for the O_2^+ ions was described in section 3.4.2. The experimental method is identical to N_2^+ (see section 6.3).

6.4.2 Charge-transfer (CT) rate coefficients: Results and discussion

State-dependent charge-transfer rate coefficients

In the experiments of Figure 6.10a, the population was tuned in the range of 7.5(9) % to 20.8(16) %. The experimental results are shown as green symbols and do not agree with the solid orange line indicating the hypothetical case of a dominant ion-quadrupole capture in the excited channel. However, the limiting value given by Langevin theory (solid blue line) represents the effective rate coefficient observed better. This implies that both the ground and the excited channels of $O_2^+ + Rb$, show Langevin-type dynamics. The Langevin rate coefficient for $O_2^+ + Rb$ ($^2S_{1/2}$) is $k_s^L = 3.3 \times 10^{-9}\,cm^3\,s^{-1}$ and the fit of a constant function to the data yielded $k_{stat}^{exp} = 2.9(8) \times 10^{-9}\,cm^3\,s^{-1}$ (red dash-dotted line).

Collision-energy-dependent charge-transfer rate coefficients

Figure 6.10b illustrates the collision-energy-dependent CT rate coefficients for the excited channel $^2P_{3/2}$ in ▲ and for the ground channel $^2S_{1/2}$ in ▼. The dash-dotted blue line is a fitted constant function for the reaction with Rb ($^2S_{1/2}$) yielding a CT rate coefficient of $k_s^{exp} = 3.4(1) \times 10^{-9}\,cm^3\,s^{-1}$. For Rb ($^2P_{3/2}$), the prediction for the ion-quadrupole capture limited rate coefficient is depicted as a dash-dotted orange line. The experimental rate coefficients for $O_2^+ + Rb$ ($^2P_{3/2}$) appear substantially smaller than the prediction and even smaller than the corresponding Langevin limit (solid orange line) indicating a pronounced influence of the short-range interactions on the dynamics.

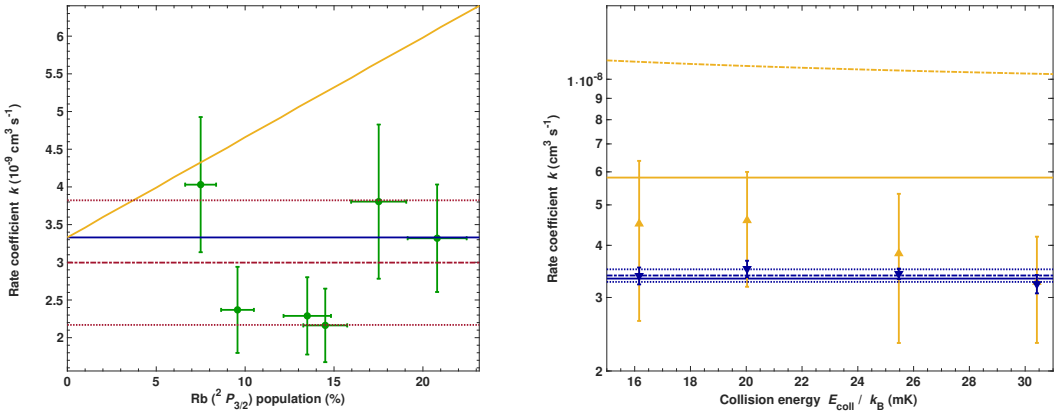

(a) (b)

Figure 6.10: Illustrated are the measured CT rate coefficients for the state-dependent experiments (a) and the collision-energy-dependent measurements (b). (a) Measured CT rate coefficients for O_2^+ depicted in ●. The orange solid line is the predicted rate coefficient as a function of the excited state fraction for an extended interaction potential incorporating the charge-induced dipole and charged-permanent quadrupole interactions. The blue solid line illustrates the theoretical Langevin rate coefficient for $O_2^+ + Rb\ (^2S_{1/2})$ and dash-dotted line the corresponding fit resulting in a rate coefficient of k_{stat}^{exp}=2.9(8) $\times 10^{-9}\,cm^3\,s^{-1}$. (b) Collision-energy-dependent rate coefficients for $O_2^+ + Rb\ (^2P_{3/2})$ ▲ and for $O_2^+ + Rb\ (^2S_{1/2})$ ▼. The theoretical Langevin rate coefficients for the Rb $^2P_{3/2}$ (solid orange line) and $^2S_{1/2}$ (solid blue line) with O_2^+ in **(a)** are $k_p^L = 5.8 \times 10^{-9}\,cm^3\,s^{-1}$ and $k_s^L = 3.3 \times 10^{-9}\,cm^3\,s^{-1}$ respectively. The dash-dotted blue line depicts the fit for the Rb $(^2S_{1/2})$ rate coefficient. The rate coefficients for the Rb $(^2P_{3/2})$ reaction are illustrated with a model using an extended interaction potential incorporating the charge-induced dipole and charged-permanent quadrupole interactions (see Appendix A.3) and the quadrupole value Q obtained from section 6.3.2.

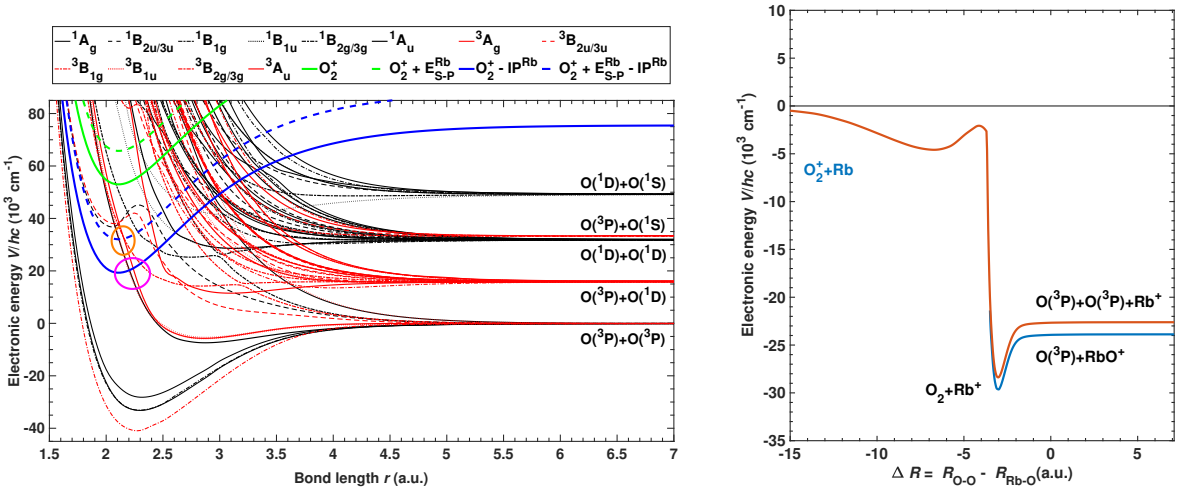

(a) (b)

Figure 6.11: (a) Electronic states for O_2 and O_2^+ as a function of the bond length r. The relevant cationic ground states are depicted in solid green lines, the cationic curves shifted by the ionisation potential of Rb by solid blue lines. Offset by the excitation potential of Rb ($^2P_{3/2}$) are the corresponding curves illustrated by dashed lines. Indicate by circles are the relevant crossing points representing non-adiabatic transitions between the surfaces. (b) Reaction pathways in linear collision geometry. Cuts of the PES along reaction coordinates for charge transfer in the linear collision geometry of the singlet channels of Rb($^2S_{1/2}$) reacting with O_2^+. See text for discussion.

Theoretical potential energy curves

In Figure 6.11a, cuts through the 3d PES for $O_2^+ + Rb$, similar to the ones in Figure 6.5a are shown. The relevant cationic ground states (green) and the cationic curves shifted by the ionisation potential of Rb (blue) are depicted as solid lines. The same curves additionally shifted by the excitation energy to the Rb ($^2P_{3/2}$) are shown as dashed lines. The crossing points between the shifted ionic curves and the neutral curves are marked by circles. These points present opportunities for non - adibatic transitions (CT) and are close to the molecular equilibrium geometry. Collisions on the singlet or the triplet PES are possible due to the double - electron spin character of the collision partners. Figure 6.11b illustrates a cut of the adiabatic PES close to the computed minimum energy path for the CT in the singlet channel at linear collision geometry. Interestingly, compared to N_2^+, the barrier, arising from a crossing with a surface connecting to the $c\ ^1\Sigma_u^-$ state of neutral O_2, is submerged and thus provides no significant bottleneck to CT at the experimental collision energies. In the corresponding triplet reaction channel, a similar curve crossing can be found and is illustrated as the red curve in Figure 6.11a crossing the entrance channel close to the equilibriums geometry. Together with the experimental findings, it can be inferred that the CT rate coefficient near the capture limit dominated by long - range Langevin - type interactions and also the short - range CT probability is near unity in both singlet and triplet collision channels for $O_2^+ + Rb$ ($^2S_{1/2}$).

6.4.3 Conclusions

Cold CT dynamics of $O_2^+ + Rb$ was explored as a function of the Rb ($^2P_{3/2}$) excited state population and of the collision energy. Most interestingly, the results for the state - dependent CT rate coefficient $k_{\text{stat}}^{\text{exp}} = 2.9(8) \times 10^{-9}\,\text{cm}^3\,\text{s}^{-1}$ and the Rb ($^2S_{1/2}$) CT rate coefficient from the collision - energy experiment $k_s^{\text{exp}} = 3.4(1) \times 10^{-9}\,\text{cm}^3\,\text{s}^{-1}$ are both in good agreement with the Langevin - rate coefficient for $O_2^+ + Rb$ ($^2S_{1/2}$) $k_s^{\text{L}} = 3.3 \times 10^{-9}\,\text{cm}^3\,\text{s}^{-1}$. Another surprising feature was revealed in the excited Rb ($^2P_{3/2}$) channel. The experimental results for the rate coefficient did not match the prediction of the ion - quadrupole capture limit (orange dash - dotted line in Figure 6.10b) and even shows a slower rate coefficient than the Langevin limit for this channel. This needs to be rationalised by further theoretical investigation. As presented in Figure 6.11b, the barrier for CT is submerged. Concluding, it can be inferred that the CT rate coefficient is near the capture limit dominated by long - range Langevin - type interactions as well as the short - range CT probability is near unity in both singlet and triplet collision channels for $O_2^+ + Rb$ ($^2S_{1/2}$).

6.5 The $N_2H^+ + Rb$ system

The molecular ion N_2H^+ is very relevant in the astrophysics [132–134] and was studied theoretically in Ref. [135, 136]. In this work however, the investigation on the polyatomic $N_2H^+ + Rb$

collision system is complementary to the first presented study of $N_2^+ + Rb$. First, to verify the measurement of $N_2^+ + Rb$ because due to the nature of the experimental setup the two molecular ions can not be told apart. Second, to extend the state - and collision - energy - dependent experiments to a polyatomic molecular ion. The following subsections will discuss the methods used to efficiently produce N_2H^+ and subsequently the CT rate coefficients.

6.5.1 Methods

Generating N_2H^+ starts by loading N_2^+ into the iontrap as described in section 6.3.1. Additionally, a hydrogen gas bottle with a cold trap was connected to the chamber. The cold trap consist of an extra long coil winded metal tube which is placed in a mixture of dry ice and acetone to freeze out unwanted gas residue before allowing H_2 to enter the chamber through the same leak valve. To ensure N_2H^+ is produced efficiently, hydrogen was leaked in the chamber for 30 s at a backing pressure of 1×10^{-8} mbar. According to Tanarro *et al.* [137], the conversion rate is $k = 2.00 \times 10^{-9}\,cm^3\,s^{-1}$ and it will not undergo any further reaction with neither N_2 nor H_2.

6.5.2 Charge - transfer (CT) rate coefficients: Results and discussion

State - dependent charge - transfer rate coefficients

In Figure 6.12a the state - dependent CT experiments are shown. The population of Rb ($^2P_{3/2}$) was tuned in the range from 7.53(59) % to 12.17(86) %. Green symbols illustrate the experimental results. The solid blue line indicates the Langevin rate coefficient for $N_2H^+ + Rb$ ($^2S_{1/2}$), k_s^L=$2.7 \times 10^{-9}\,cm^3\,s^{-1}$. The dashed - dotted line is a fit of a constant function to the experimental data. The fit yielded a CT rate coefficient $k_{stat}^{exp} = 1.12(14)\,cm^3\,s^{-1}$. In contrast to the N_2^+, there is no dependence on the excited state population. At the time of writing no theoretical investigation is present which would help to understand the underlying mechanics.

Collision - energy - dependent charge - transfer rate coefficients

Figure 6.12b shows the collision - energy dependent CT rate coefficient for $N_2H^+ + Rb$ ($^2P_{3/2}$) in ▲ and for the $N_2H^+ + Rb$ ($^2S_{1/2}$) in ▼. The dash - dotted blue line is a fit of a constant function to the $N_2H^+ + Rb$ ($^2S_{1/2}$) measurements yielding a CT rate coefficient of $k_s^{exp} = 1.6(4) \times 10^{-9}\,cm^3\,s^{-1}$. This result is surprisingly similar to the rate coefficient measured for N_2^+. The rate coefficients for Rb ($^2P_{3/2}$) are similar to the measured rate coefficient for Rb ($^2S_{1/2}$) within the uncertainty given, but far less than the theoretical Langevin rate coefficient k_p^L=$4.8 \times 10^{-9}\,cm^3\,s^{-1}$. Both show a collision - energy dependence with an increasing rate coefficient as the collision - energy increases.

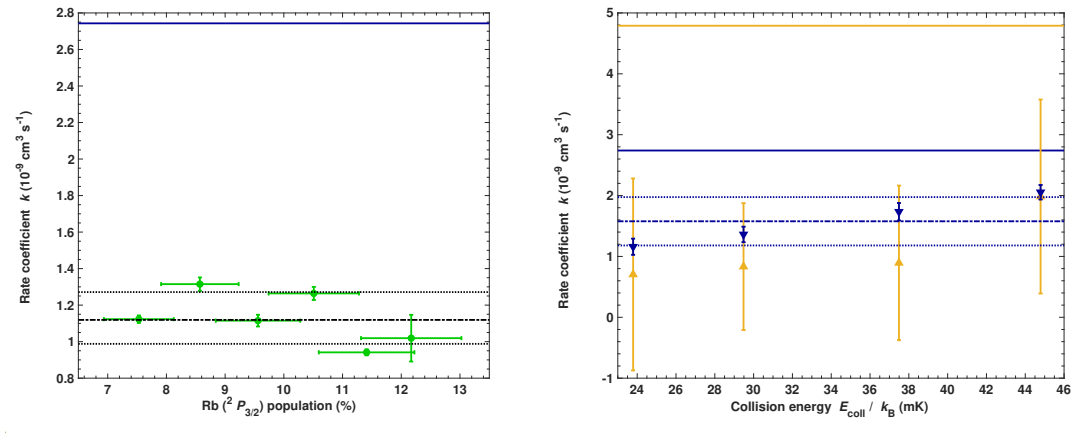

(a) (b)

Figure 6.12: Illustrated are the measured CT rate coefficients for the state-dependent experiments (a) and the collision-energy-dependent measurements (b). (a) Measured state-dependent CT rate coefficient indicated by ●. The dash-dotted line is a fit of a constant function resulting in a rate coefficient of $k_{\text{stat}}^{\text{exp}} = 1.12(14)\,\text{cm}^3\,\text{s}^{-1}$ and the solid blue line indicates the theoretical Langevin rate coefficient for Rb $(^2S_{1/2})$ k_s^{L}=$2.7 \times 10^{-9}\,\text{cm}^3\,\text{s}^{-1}$. (b) Collision-energy dependent rate coefficients for $N_2H^+ + \text{Rb}\ (^2P_{3/2})$ ▲ and for $N_2H^+ + \text{Rb}\ (^2S_{1/2})$ ▼. The theoretical Langevin rate coefficients for the Rb $(^2P_{3/2})$ (solid orange line) and $(^2S_{1/2})$ (solid blue line) with N_2H^+ in **(b)** are k_p^{L}=$4.8 \times 10^{-9}\,\text{cm}^3\,\text{s}^{-1}$ and k_s^{L}=$2.7 \times 10^{-9}\,\text{cm}^3\,\text{s}^{-1}$. The dash-dotted blues line depicts the constant function fit for the Rb $(^2S_{1/2})$ rate coefficients yielding $k_{\text{stat}}^{\text{exp}} = 1.12(14) \times 10^{-9}\,\text{cm}^3\,\text{s}^{-1}$.

6.5.3 Conclusion

The CT dynamics of $N_2H^+ + Rb$ was investigated of the excited state Rb ($^2P_{3/2}$) population and the collision - energy. A fit of a constant function to the measured CT rate coefficient for the state - dependent experiment yielded $k_{stat}^{exp} = 1.12(14)\,cm^3\,s^{-1}$. There is no dependence on the fraction of the Rb ($^2P_{3/2}$) population and it is less than half of the Langevin theory rate coefficient for $N_2H^+ + Rb$ ($^2S_{1/2}$). The Rb ($^2S_{1/2}$) CT rate coefficient obtained in the collision - energy - dependent experiments was $k_s^{exp} = 1.6(4) \times 10^{-9}\,cm^3\,s^{-1}$, showing a similar rate coefficient as for $N_2^+ + Rb$ ($^2S_{1/2}$). The collision - energy - dependent rate coefficient for $N_2H^+ + Rb$ ($^2P_{3/2}$) is equal to the ground state rate coefficient within the uncertainty. In contrast to N_2^+, the $N_2H^+ + Rb$ ($^2P_{3/2}$) does not show a decrease of the rate coefficient following the model of the extended interaction potential. The rate coefficients surprisingly increase as the collision - energy increases. Further theoretical investigations are needed to uncover the dynamics behind this interesting reaction.

7 Conclusion and outlook

This thesis investigated three main topics to extend the work on cold molecuar ion - neutral collisions utilising a newly developed method to accurately control both collision energies [9] and neutral - atom state populations during collisions.

The first topic was the simulation of a shuttling atom cloud with the goal of understanding the influence of different experimental parameters, such as cooling - laser detuning, cooling - laser intensity, pushing - laser intensity, laser - beam radius and magnetic - field gradient on the kinetic - energy spread in dependence of the kinetic energy of the Rb atoms in two different operational modes (bright and dark shuttling). The shuttling atom cloud was simulated with a Monte - Carlo trajectory method. The behaviour of the atom cloud in both experimental modes was investigated for different parameter settings and different initial temperatures $T_{\text{init}} = 163\,\mu\text{K}$ and $1024\,\mu\text{K}$. Generally, all bright - atom simulations show a higher kinetic energy in contrast to the dark - atom simulations. Variation of the cooling - laser detuning results in a difference of the overall kinetic - energy spread which is smaller for an initially colder atom cloud. Different beam radii mainly influence the maximum achievable kinetic - energy and have an influence on the kinetic - energy spread. The variation of the cooling laser intensity impacts the atom cloud only during the pushing period. Magnetic - field - gradient changes did not influence either the resulting kinetic - energy spread or the maximum achievable kinetic energy of the atoms.

The second topic was the theoretical investigation of elastic and state - changing collisions of $N_2^+ + \text{Rb}$ in dependence of the collision energy and the modeling of ion losses from radiative - association (RA) paths [103]. The main goal was to understand the contribution of these process in the overall reaction dynamics. The rotational state - changing collisions were discussed at low collision energies in the mK regime. They were computed with the ASPIN [99] code, and yielded rate coefficients in the range of $0.5 \times 10^{-11}\,\text{cm}^3\,\text{s}^{-1}$ to $2.5 \times 10^{-11}\,\text{cm}^3\,\text{s}^{-1}$ for collision energies up to 70 mK for the inelastic processes and $0.5 \times 10^{-10}\,\text{cm}^3\,\text{s}^{-1}$ to $2.5 \times 10^{-10}\,\text{cm}^3\,\text{s}^{-1}$ for the elastic processes, respectively. Both dynamics are overshadowed in the experiment by the two to three orders of magnitude larger CT rates. The modeling of ion losses from radiative association paths [103] presents a similar picture in terms of detectability in the experiment. The study presented concludes that the calculated RA reaction rates are several order of magnitude smaller than the experimentally measured rate coefficients attributed to non - adiabatic

CT.

The final part of the thesis presented a experimental and theoretical investigation of long - range vs. short - range effects in cold molecular ion - neutral collisions via charge exchange of Rb with N_2^+ and O_2^+ [112] and additionally the experimental results of a polyatomic molecular - ion study, $N_2H^+ + Rb$, in this setup.

The cold CT dynamics of $N_2^+ + Rb$ was studied as a function of the excited Rb $^2P_{3/2}$ population and the collision ,energy. The CT rate coefficient for the excited Rb $^2P_{3/2}$ population, obtained in the state - dependent experiment, is $k_{p,\text{stat}}^{\text{exp}} = 1.7(6) \times 10^{-8}\,\text{cm}^3\,\text{s}^{-1}$ and in the collision - energy dependent experiment is $k_p^{\text{exp}} = 1.1(1) \times 10^{-8}\,\text{cm}^3\,\text{s}^{-1}$ at $E_{\text{coll}} = 20\,\text{mK}$. The respective ground state Rb ($^2S_{1/2}$) CT rate coefficients measured were $k_{s,\text{stat}}^{\text{exp}} = 1.6(3) \times 10^{-9}\,\text{cm}^3\,\text{s}^{-1}$ for the state - dependent experiment and $k_s^{\text{exp}} = 1.5(2) \times 10^{-9}\,\text{cm}^3\,\text{s}^{-1}$ for the collision - energy dependent experiment. The good agreement between the experiment and the theoretical calculations of the CT using both classical and quantum approaches was achieved. Three concluding remarks can be drawn about this study. First, the CT dynamics can be understood in classical terms. Second, the dynamics are adequately approximated in reduced dimensionality. Third, describing the CT in $N_2^+ + Rb$ ($^2S_{1/2}$) in terms of only two coupled PESs seems sufficient, justified in terms of the strong non - adiabatic couplings which happen around the crossing points between the two surfaces.

The cold CT dynamics of $O_2^+ + Rb$ showed CT rate coefficients $k_{\text{stat}}^{\text{exp}} = 2.9(8) \times 10^{-9}\,\text{cm}^3\,\text{s}^{-1}$ in the state - dependent experiment and $k_s^{\text{exp}} = 3.4(1) \times 10^{-9}\,\text{cm}^3\,\text{s}^{-1}$ for the collision - energy measurement. Most interestingly, both are in good agreement with the Langevin - rate coefficient for $O_2^+ + Rb$ ($^2S_{1/2}$) $k_s^{\text{L}} = 3.3 \times 10^{-9}\,\text{cm}^3\,\text{s}^{-1}$. Surprisingly, the excited Rb ($^2P_{3/2}$) collision - energy dependent experimental results did not match the prediction of an ion - quadrupole capture calculation and even shows a slower rate coefficient than the Langevin limit for this channel. It can be inferred that the CT rate coefficient is near capture - limited dominated by long - range Langevin - type interaction as well as the short - range CT probability is near unity in both singlet and triplet collision channels for $O_2^+ + Rb$ ($^2S_{1/2}$).

The cold CT dynamics of $N_2H^+ + Rb$ exhibited a CT rate coefficient for the state - dependent experiment $k_{\text{stat}}^{\text{exp}} = 1.12(14) \times 10^{-9}\,\text{cm}^3\,\text{s}^{-1}$ and for the collision - energy dependent experiment $k_s^{\text{exp}} = 1.6(4) \times 10^{-9}\,\text{cm}^3\,\text{s}^{-1}$. The excited - state rate coefficient is equal within the uncertainty. The rate coefficients did not show any ion - quadrupole capture - limited behaviour, but interestingly a slight increase in the rate coefficient with increasing collision - energy. An additionally interesting feature is the similarity to the rate coefficients seen in the $N_2^+ + Rb$ ($^2S_{1/2}$) experiment. At the time of writing there was no theoretical investigation present.

The results presented in this thesis showed the intriguing CT collision dynamics in the low - energy regime for different molecular ions resolved by precisely tuning the collision - energy. Future experiments could take advantage from new experimental setups like discussed in the work of Rouse [59]. There is still the open question of the theoretical investigation for the $N_2H^+ + Rb$ experiment for an in - depth coverage of the dynamics and have a proper compar-

ison to the already thoroughly evaluated dynamics in $N_2^+ + Rb$.
A clear direction for the future of molecular ion - neutral hybrid experiments to dive further in the complexity of the already uncovered processes is the previously discussed setup of an ion - atom hybrid chip trap in the work of Rouse [59]. Combined with the capability of state - selective ionisation of molecular ions and the very narrow kinetic energy distribution of a much colder atom sample (BEC) would greatly improve the insight into collision studies at very low temperatures. This is experimental challenging path would be very intriguing and would be beneficial to test the resonances uncovered in the theoretical study of chapter 5 and for atomic ion - neutral interactions presented in the work of Da Silva [38].

A Programming

In the following chapter of the appendix, all programs written for this work are discussed. Codes are written in FORTRAN 77 and 95, python, LabVIEW and MATLAB. All code is available on request from the author.

A.1 Time of flight

Analysing the time-of-flight profiles from the experiment was done with a python script. The experimental data is saved to a text file. The file name inherits information about some shuttling parameters, which are extracted and used by the program to generate filenames and calculate the actual pushbeam power. The file name is structured as follows:

- 'Holdoff time' in ms, which is the time the atom cloud spends being cooled down at the off-center positions.
- 'Pushbeam duration' in µs, which is the duration accelerating the atom cloud.
- 'Freeflight time' in µs,duration of which the atoms travel with or without transversal confinement
- 'hour', 'minute' and 'second' when the file was recorded.
- 'pbpNumberofPushbeamPowerinPercent', which gives the power of the push beams used for this specific file.

To ensure good results during analysis, enough measurements (a minimum of 15 measurements is recommended) must be made, background noise must be low (turning off the lab lights is recommended), correct trigger settings have to be ensured and the MOT temperature should be monitored. This filename is created by the LabVIEW program used to measure the time-of-filght traces and should be kept in order to keep a smooth naming convention.

A brief overview of the program and its functions: After importing all libraries, defining all variables and setting all functions, the main loop starts. In the main loop, the program first reads the folder structure and browses through the folder to find all '.txt' files to count them. It

will print the number, so it can be cross checked, if it is the right number of files. Then it starts opening one file after another to read the file content and process it. Each individual file, after reading the file content, gets evaluated and one can choose if a smoothing should be applied or not. The fitting function and the initial fitting guesses are created and the first figures are already finished in a background process including peak-detection, raw data analysis and fitting itself. Afterwards, the fitted data gets fed into a matrix for further processing. In this matrix, it gets sorted according to which peaks belongs where and in ascending order, dependent on the first column, keeping the rows together so the measurements do not get mixed up into each other. From the matrix the peaks for the calculation are extracted. Velocities are calculated. Afterwards, figures and PDFs get created and saved to a specific folder inside the measurement data folder. PDFs include all necessary information about each peak and the calculated velocities.

A.2 Simulation analysis

A.2.1 Atom cloud simulation

To extract the data of atom cloud simulations, a specific set of programs has been written in python. The first part contains the previously discussed TOFTrace time-of-flight analysis software to recreate and compare the PMT traces of the simulation with the ones from the actual experiment. The second part is an additional program, with the name of 'histograms_autofile_for_Thesis.py', is used to extract the information from the files carrying the information for the kinetic energy. It reads the file data and fits a Gaussian function. The center of the Gaussian is the actual kinetic energy and the σ of the Gaussian is the kinetic energy resolution of the simulation. Thirdly, there is a small program which compares the simulation results to the experimental data. Both time-of-flight trace programs write their final analysed data in an extra text file.

Inputfile

Example for an atom simulation inputfile:
XXXXXXXXXXXXXXXXXXXXXXXXXXXXXX
Input Variables
XXXXXXXXXXXXXXXXXXXXXXXXXXXXXX
veq1026_0.6_db9.167_163uK.dat . . . equilibrated atom cloud datafile name
5D-9 . . . X Axis Power in mW
5D-9 . . . Y Axis Power in mW
5D-9 . . . Z Axis Power in mW
3.7D3 . . . X Axis 1/e Laser Beam Radius in mm
3.7D3 . . . Y Axis 1/e Laser Beam Radius in mm

3.7D3 . . . Z Axis 1/e Laser Beam Radius in mm
9.2D-17 . . . Saturation Intensity Is in W/m$\hat{2}$
38.11711D0 . . . Natural Linewidth Gamma in 2*Pi*MHz
20000 . . . Atomnumber
2D0 . . . Cooling Detuning in Mhz
500D0 . . . t X Axis Cooling and Pushing Laser off in us
175D0 . . . t Push Beam Pulse duration in us
0D0 . . . Pushing Detuning
1D0 . . . Integration Timestep
XXXXXXXXXXXXXXXXXXXXXXXXXXXXXX
44D3 . . . Magnetic Coil Radius in mm
56D3 . . . Magnetic Coil distance in mm
121 . . . Number of Windings
9.167D-14 . . . Magnetic Field Gradient 1/2 in Gauss
XXXXXXXXXXXXXXXXXXXXXXXXXXXXXX
50 . . . Single Slit beginning in um
-50 . . . Single Slit ending in um
443.41D0 . . . Double Slit beginning Slit 1 in um
362.79D0 . . . Double Slit ending Slit 1 in um
-362.79D0 . . . Double Slit beginning Slit 2 in um
-443.41D0 . . . Double Slit ending Slit 2 in um
XXXXXXXXXXXXXXXXXXXXXXXXXXXXXX

A.2.2 Collision simulation

The calculations discussed in chapter 5 utilise two different codes. First the VLAMBDA code and secondly the ASPIN code. Both codes were acquired from Prof. Gianturco. Detailed information on the ASPIN code can be found in Ref. [99]. All code is programmed in Fortran 77, but should be compiled with an ifort compiler.

VLAMBDA

The VLAMBDA code loads the PES surface data and prepares it to be used for calculation with the ASPIN code. There are two small codes in the folder. First one is 'xcolctor_data.f90'. This code reads the information of the PES and generates two files, namely 'r.dat' and 'pot.dat'. There are two variables which have to be changed according to the PES. One is 'NR' which denotes the number of radial points in the PES and the other one is 'NT' setting the numbers of angles. After acquiring these two files, the VLAMBDA code can be run. The VLAMBDA code asks for some input parameters to start its calculation. First it will ask for the number

of lines in the 'pot.dat' file, then it will ask for the number of lines in the 'r.dat' file. The third question is about the step size between the angles. Fourth, it asks if the molecule is homonuclear or heteronuclear. Then the number of lambdas has to be specified and finally the number of points which one wants each lambda to be fitted in (e.g. 1000). The output file will produce 'V_l_FITTED_A.dat' and 'V_l_FITTED_P.dat'. V_l_FITTED_A.dat' is modified for ASPIN input and 'V_l_FITTED_P.dat' is modified for the phyton plotting program. The 'V_l_FITTED_P.dat' can be analysed with the code, which can be found on the group server under 'ASPIN_Vlambda' inside a folder named 'N2'. There is the necessary software to analyse the VLAMBDA file. The progam description is in the file and the program will ask for the necessary files. The original *ab initio* potential has to be in a folder called 'abinitio' inside the folder, which includes 'V_l_FITTED_P.dat'.

ASPIN

On the group server under 'ASPIN_Vlambda' the original, already compiled files for the studix cluster are uploaded in the 'ASPIN' folder. Additionally, the file for submitting to the cluster is called 'jobsumitserver.sh', which will submit the preconfigured script file for ASPIN and set the library paths correctly for the 'Lapack.f90'. The ASPIN code itself needs an input file folder and an output file folder. In the input folder the 'V_l_FITTED_A.dat' has to be placed, but renamed to 'V_l_FITTED.dat'. To understand the ASPIN code, it is suggested to read Ref. [99] very carfully. Inputfiles 'setup' is self explanatory by browsing through the included input script in the 'ASPIN' folder. After submission of the ASPIN calculation to the server, one will be alerted by an email after it has finished, if this option is set in the submission script. After completing a calculation run, the output files can be prepared for evaluation with the 'aspin_output_analysis.py' from the folder 'N2'. This program generates a text file, which can be read either by 'parapifa.py' for odd rotational states or by 'parapifa2.py' for even rotational states. Both programs will calculate and print different graphs for elastic and inelastic cross-sections and rates. There is also a program included in a folder called 'CodeForRateCoeff'. This program was also acquired from Prof. Gianturco. To use this program please contact Prof. GIanturco himself.

A.3 Extended interaction potential fitting routine

The following section explains the fitting routine, which was used to fit the extended interaction potential discussed in section 2.1.1. For this purpose, a matlab script was developed. Firstly the effective potential need to be defined:

$$V_{\text{eff}} = -\frac{C_4}{R^4} + \frac{C_3}{R^3} + \frac{E_{\text{T}} b^2}{R^2}. \tag{A.1}$$

For C_3 and C_4, the definitions from Equation (2.13) (C_3) and from (2.5) (C_4) will be used. The maximum impact parameter b_{max} is calculated as follows:

$$\left.\frac{\partial V_{\text{eff}}}{\partial R}\right|_{R=R_{\text{max}}} = \frac{4C_4}{R^5} - \frac{3C_3}{R^4} - \frac{2E_{\text{T}}b^2}{R^3} = 0, \tag{A.2}$$

$$R_{\text{max}} = \frac{-3C_3 \pm \sqrt{(-3C_3)^2 + 32E_{\text{T}}b^2C_4}}{4E_{\text{T}}b^2}, \tag{A.3}$$

$$0 = E_{\text{T}}(R_{\text{max}}^4) - E_{\text{T}}b_{max}^2(R_{\text{max}}^2) - C_3R_{\text{max}} + C_4, \tag{A.4}$$

$$k = \pi b_{max}^2\sqrt{\frac{2E}{\mu}}. \tag{A.5}$$

Using Equation (A.3) with Equation (A.4) the rate coefficient with Equation (A.5) is calculated. This whole calculation is consistent with the quadrupole moment used for the theoretical calculation by our theory collaborator Michał Tomza, which is defined as:

$$\Theta_0^{(2)} = -\frac{e}{2}\sum_j (3z_j^2 - r_j^2) \tag{A.6}$$

$$\Theta(\gamma, J) = \langle \gamma JJ|\Theta_0^{(2)}|\gamma JJ\rangle \tag{A.7}$$

Equation(A.6) is equal to Equation (27) in Ref. [138] and Equation (A.7) is equal to Equation (30) in Ref. [138] and defined by Angel *et al.* [139].

The used fitting routine is as follows:

```
clear Qval
clear Aval
x = E_N2*kb/10^3
y = N2_all_mean_Dens_O2_calc.Mean_e
yerr = N2_all_mean_Dens_O2_calc.Std_e
ffun = @(qfit,x) TSCoFu(qfit,1.602,x,varsN2_v2);
% ffun = @(qfit,x) FSCoFu(qfit,1.602,x,varsN2_v2);
% define the fit type and fitting options:
ft = fittype(ffun,'independent','x','dependent','y');
opts = fitoptions('Method','NonlinearLeastSquares','Robust','Bisquare');
opts.Display = 'iter';
opts.TolX=1e-23;
opts.TolFun=1.0e-18;
% opts.Lower = [1e-3 1e-3];
% opts.Upper = [3e3 3e3];
% opts.StartPoint = [2.2 1.6109];
opts.Lower = [1e-3];
opts.Upper = [3e3];
opts.StartPoint = [2.2];
% fit (x,y must be column vectors):
[fr, gof,output] = fit(x,y,ft,opts)

% extract the confidence intervals (0.68 - 1 sigma)
err=confint(fr,0.68);
err=(err(2,:)-err(1,:))/2;
Qval = fr.qfit;
%Aval = fr.afit;
%tval = fr.tfit;
% plot data and fit:
figure;
p=plot(x,y,'o'); % plot data
hold on;
plot(x,ffun(fr.qfit,x),'-','linewidth',2,'color',get(p,'color')); % plot fit
% plot(x,ffun(fr.qfit,fr.afit,x),'-','linewidth',2,'color',get(p,'color')); % plot fit
% Fitting Data For Plotting
% N2sim = CModel(fr.qfit*10^(-39),1.602*10^(-38),EN2sim*kb/10^3,[rmN2,q,e0,Angs]);
% N2simUpper = CModel((fr.qfit+err(1,1))*10^(-39),(fr.afit+err(1,2))*10^(-38),EN2sim*kb/10^3,[rmN2,q,e0,
    Angs])
% N2simLower = CModel((fr.qfit-err(1,1))*10^(-39),(fr.afit-err(1,2))*10^(-38),EN2sim*kb/10^3,[rmN2,q,e0,
    Angs])

% O2sim = CModel(fr.qfit*10^(-39),1.602*10^(-38),EO2sim*kb/10^3,[rmO2,q,e0,Angs]);
% O2simUpper = CModel((fr.qfit+err(1,1))*10^(-39),(fr.afit+err(1,2))*10^(-38),EO2sim*kb/10^3,[rmO2,q,e0,
    Angs])
% O2simLower = CModel((fr.qfit-err(1,1))*10^(-39),(fr.afit-err(1,2))*10^(-38),EO2sim*kb/10^3,[rmO2,q,e0,
    Angs])

% N2Hsim = CModel(fr.qfit*10^(-39),1.602*10^(-38),EN2Hsim*kb/10^3,[rmN2H,q,e0,Angs]);
% N2HsimUpper = CModel((fr.qfit+err(1,1))*10^(-39),(fr.afit+err(1,2))*10^(-38),EN2Hsim*kb/10^3,[rmN2H,q,e0,
    Angs])
% N2HsimLower = CModel((fr.qfit-err(1,1))*10^(-39),(fr.afit-err(1,2))*10^(-38),EN2Hsim*kb/10^3,[rmN2H,q,e0,
    Angs])
```

The used function TSCoFu is:

```
function rv = TSCoFu(qtest,atest,xdata,vars)
mu = vars(1);
q = vars(2);
e0 = vars(3);
Angs = vars(4);
a0 = vars(5);
Qval = -1*qtest*q/2*2/5*a0^2*(q/(4*pi*e0));
alphaval = 1/2*(atest*1e-38)*(q/(4*pi*e0))^2;

for i = 1:1:length(xdata)
        xda = xdata(i,1);
        syms bmaxSq
        R=((-3)*Qval*Angs^5+sqrt(((-3)*Qval*Angs^5)^2+32*xda*Angs^2*sqrt(bmaxSq)^2*Angs^2*alphaval*Angs^6))
            ./(4*xda*Angs^2*sqrt(bmaxSq)^2*Angs^2);
        cb = solve(xda*Angs^2.*(R).^4-xda*Angs^2*sqrt(bmaxSq)^2*Angs^2.*(R).^2-Qval*Angs^5.*(R)+alphaval*
            Angs^6 == 0, bmaxSq);
        c_b = sqrt(cb);
        c_br = vpa(c_b);
        bmax1 = c_br(c_br == real(c_br));
        bmax = bmax1(find(abs(bmax1)>0));
        cm(i,1) = vpa(pi.*bmax.^2.*sqrt(2.*xda/mu)*10^6);
        rv = double(cm);
end
```

A.4 Data analysis and uncertainty calculation

In this section, the data analysis and the error calculation for the rate coefficient measurements with the moving atom cloud will be discussed. First, all necessary steps and calculations to acquire the rate coefficients will be listed and subsequently their uncertainties.

A.4.1 Data analysis for the rate coefficient measurements

Pseudo - first - order $k_{\mathbf{pfo,A}}$ and second - order $k_{\mathbf{A}}$ rate coefficients

Calculating the pseudo - first order rate coefficient (k_{pfo}) is done by determining the length of the string of the molecular ions $L_{\mathrm{A},t}$, where A is the ion species, in dependence of the reaction time t and plotting $\ln(L_{\mathrm{A},t}/L_{\mathrm{A},0})$ as a function of time t. The gradient of the resulting straight line is -$k_{x,\mathrm{pfo,A}}$ (x: denotes state of the atoms, A: denotes the ion species). Step by Step Instructions for the pseudo - first - order coefficient:

1 Load crystal images into LabVIEW analysis software Crystalfitter_v2.vi.

2 Set boundary condition and measure molecular ion string length.

3 Paste information into table for calculation of $\ln(L_{\mathrm{A},t}/L_{\mathrm{A},0})$, plotting and fitting with linear regression model.

4 Obtain $k_{x,\mathrm{pfo,A}}$ and the standard deviation of the fit for each measurement.

5 Repeat for each measurement.

Now the $k_{x,\mathrm{pfo,A}}$ can be used to calculate the second - order rate coefficient $k_{x,\mathrm{A}}$.

$$k_{x,\mathrm{A}} = \frac{k_{\mathrm{pfo,A}}}{n_{\mathrm{avg}} \cdot f_{x,\mathrm{overlap,A}}}. \tag{A.8}$$

In Equation (A.8), $k_{x,\mathrm{A}}$ is the second - order rate coefficient for the atoms in state x and the ion species A, $k_{x,\mathrm{pfo,A}}$ is the pseudo - first - order rate coefficient, $\mathrm{n_{avg}}$ is the average density of the atom cloud and $f_{x,\mathrm{overlap,A}}$ is the overlap factor for the atom cloud with the molecular ions. The density of the atom cloud was inferred from the $O_2^+ + \mathrm{Rb}(^2S_{1/2})$ measurement as follows:

1 The theoretical second - order rate coefficient for $O_2^+ + \mathrm{Rb}(^2S_{1/2})$ (Langevin rate coefficient) was calculated.

2 The pseudo - first order rate and the overlap factor are known.

3 Rearranging Equation (A.8) to calculate the atom density n_{avg}

Second-order rate coefficient k for the stationary hybrid trap measurement

Equation (A.9) is used to calculate the second-order rate coefficient dependent on the excited state fraction discussed in Chapter 6. $k_{x,\mathrm{pfo}}$ is the pseudo - first order rate coefficient measured for the molecular ion x, $n_{\mathrm{avg,stat}}$ is the average density of the stationary atom cloud (see section 3.2.2) and f_{o} is the overlap factor between ions and atoms as calculated in A.5. Firstly the population following Equation (A.13) for p_p and Equation (A.12) for p_s. Secondly, Equation (A.10) is used to fit the measurement of the stationary MOT with the molecular ions, leaving $k_{s,\mathrm{stat}}$ and $k_{p,\mathrm{stat}}$ as free parameters to be determined by the linear least-square fit.

$$k_{\mathrm{stat}} = \frac{k_{x,\mathrm{pfo}}}{n_{\mathrm{avg,stat}} f_{\mathrm{o}}} \tag{A.9}$$

$$k_{\mathrm{stat,fit}} = \frac{1}{2}\left(k_{s,\mathrm{stat}}(1+p_s) + k_{\mathrm{p,stat}} p_p\right) \tag{A.10}$$

$$\rho_{\mathrm{p}} = \frac{S_0}{2} \cdot \frac{1}{1 + S_0 + \left(\frac{2\delta}{\Gamma}\right)^2} \tag{A.11}$$

$$p_p = \rho_{\mathrm{p}} * 100 \tag{A.12}$$

$$p_s = 1 - p_p \tag{A.13}$$

Calculating rate coefficients of N_2^+ / O_2^+ + Rb in either the $^2P_{3/2}$ or the $^2S_{1/2}$ state

The second - order rate coefficient equation combining both Rb - states is as follows:

$$k = (k_s p_s + k_p p_p), \tag{A.14}$$

where k_s is the second - order rate coefficient for Rb($^2S_{1/2}$) with the population of atoms in the $^2S_{1/2}$ state denoted as p_s and k_p being the second - order rate coefficient for Rb($^2P_{3/2}$) with the population of atoms in the $^2P_{3/2}$ state denoted as p_p. Measured data from the experiment where Rb is in the $^2S_{1/2}$ state is pure ($p_s = 1$) and hence the second - order rate coefficient can easily be calculated with:

$$k_{s,\mathrm{A}} = \frac{k_{s,\mathrm{pfo,A}}}{n_{\mathrm{avg}} \cdot f_{s,\mathrm{overlap,A}}}. \tag{A.15}$$

For the second - order rate coefficient with Rb($^2P_{3/2}$), the measurement only provides a mix of the two states of Rb. The population of the atoms in $^2P_{3/2}$ is dependent mainly on the laser power and the detuning of the cooling lasers for the atoms. In order to calculate the second - order rate coefficient for the Rb($^2P_{3/2}$) channel the following formula is needed:

$$k_p = \frac{k - k_s p_s}{p_p}, \tag{A.16}$$

where:

- k_s: second - order rate coefficient for Rb($^2S_{1/2}$)
- k_p: second - order rate coefficient for Rb($^2P_{3/2}$)
- k: second - order rate coefficient for Rb($^2P_{3/2}$) + Rb($^2S_{1/2}$)
- p_s: Population of atoms in Rb($^2S_{1/2}$)
- p_p: Population of atoms in Rb($^2P_{3/2}$)
- S_0: On resonance Saturation intensity parameter for Rb
- Γ: Natural linewidth of Rb cooling transition
- δ: Detuning from resonance for Rb cooling

Calculation of the overlapfactor $f_{x,\ \mathbf{overlap,A}}$

The factor in the interaction region between the molecular ions and the atom cloud, $f_{x,\mathrm{overlap,A}}$ is calculated.

$$f_{x,\mathrm{overlap,A}} = t^{'} \cdot sc, \tag{A.17}$$

where:

- $t^{'}$: average interaction time of the atom cloud with the molecular ions
- sc: shuttlingcycle (shuttling repetitions)

Effective Power P_0

Effective power P_0 is calculated as

$$P_0 = \frac{P_{y+} \cdot L_{\mathrm{VP}} + P_{y-} \cdot L_{\mathrm{VP}} + P_{z+} \cdot L_{\mathrm{VP}} + P_{z-} \cdot L_{\mathrm{VP}}}{0.986}, \tag{A.18}$$

where $P_{y+,y-,z+,z-}$ are the laser powers on the respective beam and L_{VP} is the loss due to the chamber viewports. The factor 0.986 corrects for the finite size of the aperture of the power head used to measure the laser powers. It is calculated by dividing a 2d - Gaussian integrated with the boundaries of the finite size of the aperture of the power head by a 2d - Gaussian integrated to infinity.

Intensity I

Intensity I is calculated as

$$I = \frac{2P_0}{\pi\omega_{780}^2}, \tag{A.19}$$

where P_0 is the effective power and ω_{780} the $1/e^2$ radius of the laser beam.

Saturation Paramter S_0

Saturation parameter S_0 is calculated as

$$S_0 = \frac{I}{I_S}, \tag{A.20}$$

where I_S is the saturation intensity. ($I_S = 9.2 \pm 1.7$ mW·cm^{-2}, Ref. [94]).

A.4.2 Uncertainties

Pseudo - first order The uncertainty of the pseudo first order is given by the standard deviation of the linear regression fit. This results in $k_{x,\mathrm{pfo,A}} \pm \sigma_{k_{x,\mathrm{pfo,A}}}$. For all measured reactions it is around 10 %.

MOT Density

Overlap factor The error estimation of $f_{x,\mathrm{overlap,A}}$ is determined by the standard deviation of the average interaction time $t^{'}$ multiplied with sc and calculates to be around 11.5 % for each measurement.

Second - order rate coefficient for the Rb($^2S_{1/2}$) measurements

The uncertainty of the second - order rate coefficient k_s was calculated as follows:

$$\sigma_{k_s} = \sqrt{\left(\frac{1}{n_{\mathrm{avg}} \cdot f_{s,\mathrm{overlap,A}}} \cdot \sigma_{k_{s,\mathrm{pfo,A}}}\right)^2 + \left(\frac{k_{s,\mathrm{pfo,A}}}{n_{\mathrm{avg}}^2 \cdot f_{s,\mathrm{overlap,A}}} \cdot \sigma_{n_{\mathrm{avg}}}\right)^2 + \ldots} \overline{\ldots + \left(\frac{k_{s,\mathrm{pfo,A}}}{n_{\mathrm{avg}} \cdot f_{s,\mathrm{overlap,A}}^2} \cdot \sigma_{f_{s,\mathrm{overlap,A}}}\right)^2}. \tag{A.21}$$

Second - order rate coefficient for the Rb($^2P_{3/2}$) measurements

The uncertainty of the second - order rate coefficient k was calculated as follows:

$$\sigma_k = \sqrt{\left(\frac{1}{n_{\mathrm{avg}} \cdot f_{\mathrm{overlap}}} \cdot \sigma_{k_{\mathrm{pfo,A}}}\right)^2 + \left(\frac{k_{\mathrm{pfo,A}}}{n_{\mathrm{avg}}^2 \cdot f_{\mathrm{overlap}}} \cdot \sigma_{n_{\mathrm{avg}}}\right)^2 \ldots} \overline{\ldots + \left(\frac{k_{\mathrm{pfo,A}}}{n_{\mathrm{avg}} \cdot f_{\mathrm{overlap}}^2} \cdot \sigma_{f_{\mathrm{overlap}}}\right)^2}, \tag{A.22}$$

now followed by calculating the uncertainty of second - order rate coefficient for the Rb($^2P_{3/2}$) measurements:

$$\sigma_{k_p} = \sqrt{\left(\frac{1}{p_p} \cdot \sigma_k\right)^2 + \left(\frac{p_s}{p_p} \cdot \sigma_{k_s}\right)^2 + \left(\frac{k_s}{p_p}\sigma_{p_s}\right)^2 + \left(\frac{k - k_s p_s}{p_{\mathrm{p}}^2}\sigma_{p_p}\right)^2}. \tag{A.23}$$

Effective Power P_0 The uncertainty in effective power $\sigma_{P_0}$was estimated as

$$\sigma_{P_0} = \sqrt{\left(\frac{L_{\mathrm{VP}}}{0.986}\right)^2 \left(\sigma^2_{P_{y+}} + \sigma^2_{P_{y-}} + \sigma^2_{P_{z+}} + \sigma^2_{P_{z-}}\right) \left(\frac{P_{y+} + P_{y-} + P_{z+} + P_{z-}}{0.986}\right)^2 \sigma^2_{L_{\mathrm{VP}}}}. \quad \text{(A.24)}$$

Intensity I The uncertainty in the intensity σ_I was estimated as

$$\sigma_I = \sqrt{\left(\frac{2}{\pi\omega^2_{780}} \cdot \sigma_{P_0}\right)^2 + \left(\frac{4P_0}{\pi\omega^3_{780}}\sigma_{\omega_{780}}\right)^2}. \quad \text{(A.25)}$$

Saturation Parameter S_0 The uncertainty in Saturation parameter σ_{S_0} was estimated as

$$\sigma_{S_0} = \sqrt{\left(\frac{1}{I_{\mathrm{S}}} \cdot \sigma_I\right)^2 \left(\frac{I}{{I_{\mathrm{S}}}^2} \cdot \sigma_{I_S}\right)^2}. \quad \text{(A.26)}$$

Excited population The uncertainty of the excited population p_p was calculated following

$$\sigma_{p_p} = \sqrt{\left(\frac{4\delta^2\Gamma^2 + \Gamma^4}{2\left(4\delta^2 + \Gamma^2\left(1 + S_0\right)\right)^2} \cdot \sigma_{S_0}\right)^2 + \left(-\frac{4\delta S_0}{\Gamma^2\left(1 + S_0 + \left(\frac{2\delta}{\Gamma}\right)^2\right)}\sigma_\delta\right)^2} \cdot 100. \quad \text{(A.27)}$$

Calculating overall uncertainties

The overall uncertainty was calculated following:

$$\sigma_{k_{p,\mathrm{all}}} = \frac{\sqrt{\sum_{n=0}^{N} \sigma^2_{k_p}}}{N}, \quad \text{(A.28)}$$

$$\sigma_{k_{s,\mathrm{all}}} = \frac{\sqrt{\sum_{n=0}^{N} \sigma^2_{k_s}}}{N}. \quad \text{(A.29)}$$

N is the number of measurements analysed.

A.4.3 Results for the uncertainty estimation

In this section, the relationship between the results of the measurement and of the uncertainty calculations will be discussed. Before closer looking on the detailed cases, an overall error budget is estimated.

Table A.1: Uncertainty estimation

Variable	Value	Uncertainty	Unit
$k_{pfo,x,A}$	$0.01 \ldots 0.005$	$8 \cdot 10^{-5} \ldots 8 \cdot 10^{-4}$	
k	$1 \cdot 10^{-9} \ldots 1 \cdot 10^{-8}$	$1 \cdot 10^{-10} \ldots 1 \cdot 10^{-9}$	cm^3s^{-1}
k_p	$1 \cdot 10^{-9} \ldots 1 \cdot 10^{-8}$	$1 \cdot 10^{-10} \ldots 1 \cdot 10^{-9}$	cm^3s^{-1}
p_p	11.71	1.6	%
p_s	88.29	1.6	%
$f_{overlap}$	$\sim 1.5 \cdot 10^{-2}$	$\sim 1.7 \cdot 10^{-3}$	
n_{avg}	$2.8 \cdot 10^8$	$1.6 \cdot 10^7$	cm^{-3}

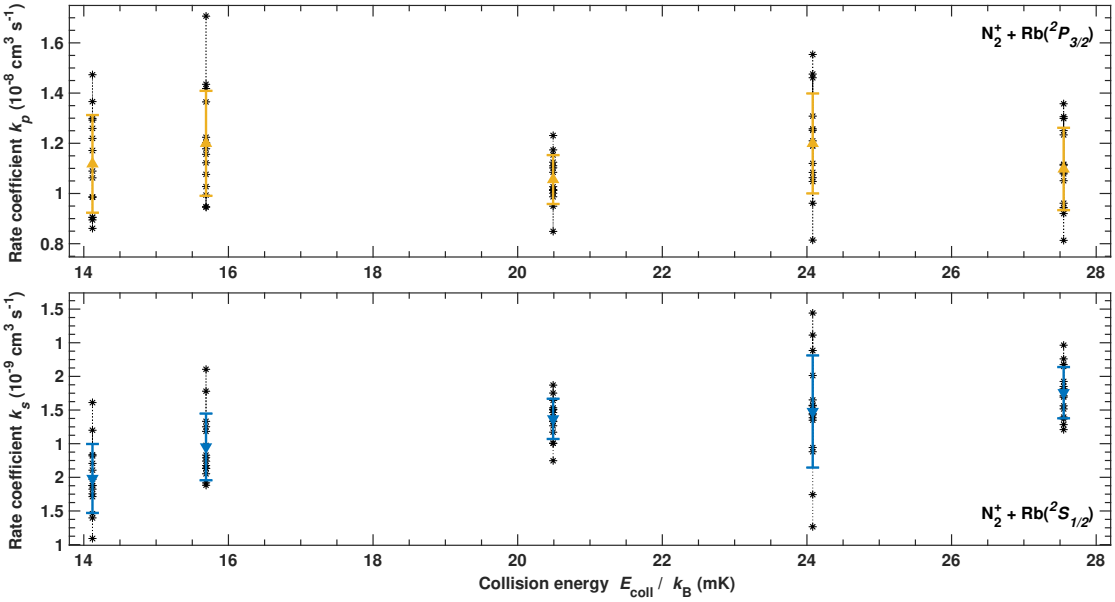

Figure A.4.1: Comparison of the single measured rate coefficients to the mean value $\overline{k_p}$ in the upper panel and in the lower panel the comparison of the single measured rate coefficients to the mean value $\overline{k_s}$ for N_2^+

$N_2^+ + Rb$

Following equations (A.8), (A.12), (A.13), (A.15) and (A.16), the second - order rate coefficients of $N_2^+ + Rb(^2S_{1/2})$ and $N_2^+ + Rb(^2P_{3/2})$ were calculated and are shown in Figure A.4.1 as *. The mean value of the second - order rate coefficients related to the single measurements are displayed in orange for $N_2^+ + Rb(^2P_{3/2})$ and in blue for $N_2^+ + Rb(^2S_{1/2})$. The error bars presented in Figure A.4.1 are the calculated uncertainties as the standard deviation for $N_2^+ + Rb(^2P_{3/2})$ and for the $N_2^+ + Rb(^2S_{1/2})$, respectively.

$O_2^+ + Rb$

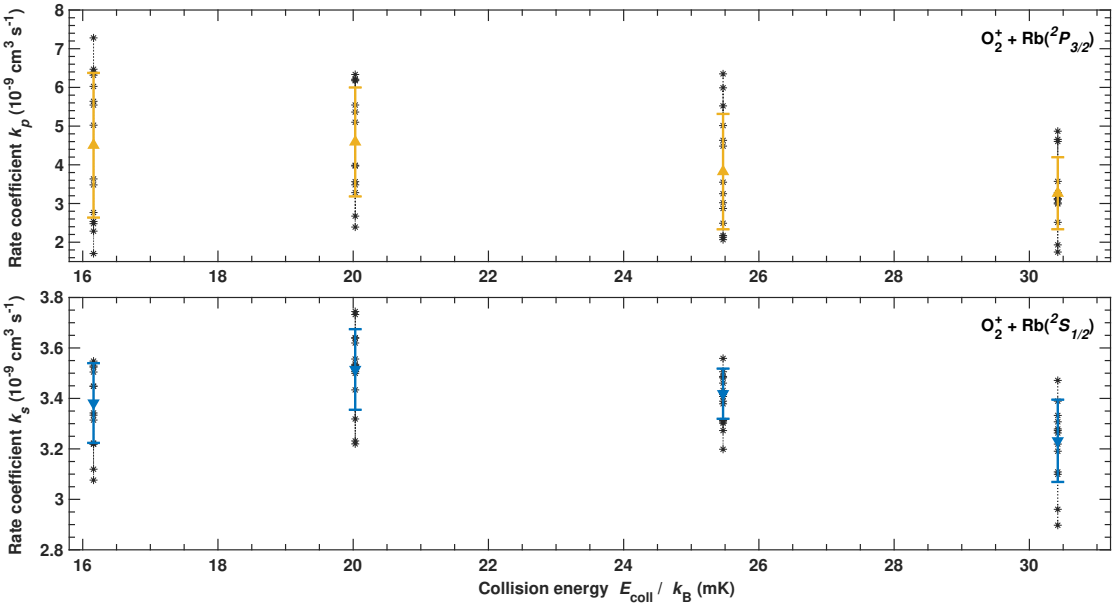

Figure A.4.2: Comparison of the single measured rate coefficients to the mean value $\overline{k_p}$ in the upper panel and in the lower panel the comparison of the single measured rate coefficients to the mean value $\overline{k_s}$ for O_2^+

Following equations (A.8), (A.12), (A.13), (A.15) and (A.16), the second - order rate coefficient of $O_2^+ + Rb(^2S_{1/2})$ and $O_2^+ + Rb(^2P_{3/2})$ were calculated and are shown in Figure A.4.2 as *. The mean value of the second - order rate coefficients related to the single measurements are displayed in orange for $O_2^+ + Rb(^2P_{3/2})$ and in blue for $O_2^+ + Rb(^2S_{1/2})$. The error bars presented in Figure A.4.2 are the calculated uncertainties from as the standard deviation for $O_2^+ + Rb(^2P_{3/2})$ and for the $O_2^+ + Rb(^2S_{1/2})$, respectively.

$N_2H^+ + Rb$

Following equations (A.8), (A.12), (A.13), (A.15) and (A.16), the second - order rate coefficient of $N_2H^+ + Rb(^2S_{1/2})$ and $N_2H^+ + Rb(^2P_{3/2})$ were calculated and are shown in Figure A.4.1 as *. The mean value of the second - order rate coefficients related to the single

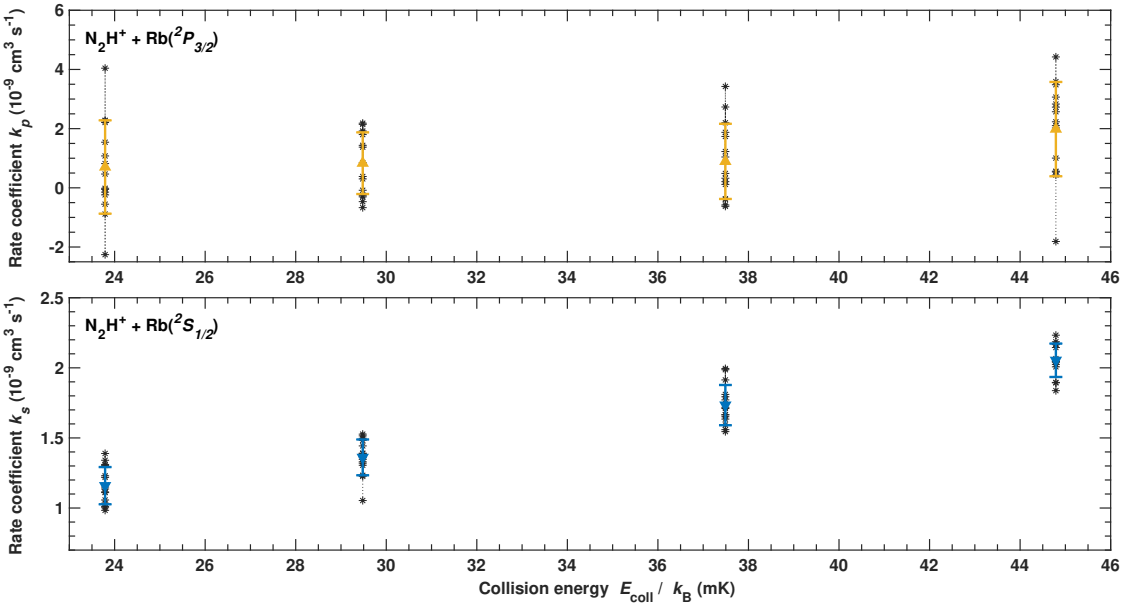

Figure A.4.3: Comparison of the single measured rate coefficients to the mean value $\overline{k_p}$ in the upper panel and in the lower panel the comparison of the single measured rate coefficients to the mean value $\overline{k_s}$ for N_2H^+

measurements are displayed in orange for $N_2H^+ + Rb(^2P_{3/2})$ and in blue for $N_2H^+ + Rb(^2S_{1/2})$. The error bars presented in Figure A.4.3 are the calculated uncertainties as the standard deviation for $N_2H^+ + Rb(^2P_{3/2})$ and for the $N_2H^+ + Rb(^2S_{1/2})$, respectively.

A.5 Overlap factor

To calculate the overlap factor for the molecular ion string with the atom cloud, a Fortran 95 program was written adapted from the initial program presented in the master thesis of Eberle [140]. It is located in the group software in folder 'OverlapProgramFortran'. In the folder three programs can be found. One to calculate the overlap of a stationary atom cloud with the Coulomb crystal, one to calculate the overlap with a moving atom cloud and a third on which calculates the overlap of a moving atom cloud with a string of molecular ions. The stationary mode of the program was verified with the initial program of Eberle and confirmed with the same results for the same input parameters. The idea behind the moving atom cloud overlap factor calculations is to move the Coulomb crystal through the atom cloud instead. The Coulomb crystal is moved along a line in a 45° angle. At evenly spaced points along the moving direction, the program calculates the density ratio, which is then used to calculate the interaction time t' at each point. The interaction time per grid unit is calculated from the grid spacing and the average velocity of the atom cloud, which is then multiplied with the density ratio from the overlap code. This is then further accumulated to the over all interaction time t' of the atom cloud with the Coulomb crystal. t' is then multiplied with the shuttling cycle sc

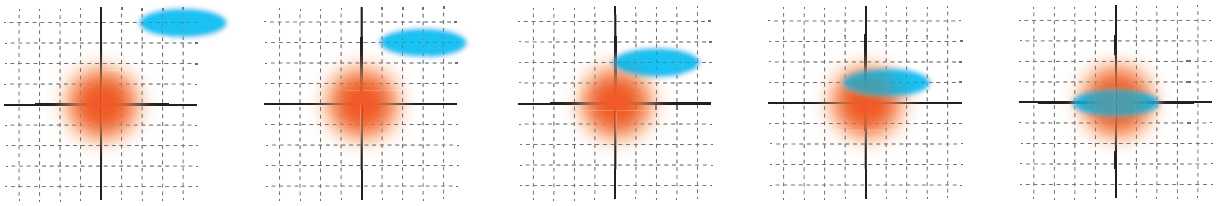

Figure A.5.1: Illustration of a calculation sequence of the Coulomb crystal moving through the atom cloud on a specific grid size. The Coulomb crystal moves diagonally through the atom cloud and the density ratio is calculated. It is sufficient to calculate on half of the process to the center and multiply the positive off-center with two to gain the missing information.

to yield the overlap factor for between the atom cloud and the Coulomb crystal or the string of molecular ions.

A.6 Population of Rb in the $(5s)^2P_{3/2}$ state

This is a small Fortran 95 program to calculate the population of Rb in the (5s) $^2P_{3/2}$ during the bright shuttling free flight period of the experiment and for the stationary atom cloud. The software can be found on the group software server under 'Rb population calculator'. To run the calculation, the input file must be adjusted accordingly. It can be run on the server with: './valuesfull.o -i inputvaluesfull.txt'. In the input file following parameters can be set:

- Power, radius, detuning of the cooling laser beams
- all magnetic coil parameters
- saturation intensity, natural linewidth and all errors off all parameters

Additionally, the population according to Hall [10] is calculated as a base information. The program then calculates the the population following equations (A.19), (A.20), (A.12) and (A.13). After completion of the calculation the output will show all information needed labelled accordingly including all errors.

A.7 Laser shutter and Oven controller

Ovens and laser shutters are controlled by an Arduino Nano v3. It controls the two laser shutters for the 355 nm and both dye lasers and all ovens for the experiment. The program running on the Arduino includes the 'Servo.h' library. Firstly, all ports and pins are configured. In the next part the functions for all the serial events are set. These functions are addressed by the LabVIEW control. The Arduino reads the serial input coming from the control program and runs the specific case in the program. The program can be found on the program

backup in 'pc-swsrv1.chemie.unibas.ch:/home/data/Alexander/ArduinoCode/'. The program 'LaserOven_v2.ino' can be flashed on an Arduino Nano v3. Afterwards the right pins must be connected. Pin description can be found in the program itself.

A.8 Polarisation stabilisation

The program was coded with the Arduino coding environment. The AccelStepper.h library and the PCD8544.h library are included in the Stepper_Motor_HWP_v6.0.zip file, which can be found on the 'pc-swsrv1.chemie.unibas.ch:/home/data/Alexander/ArduinoCode'. For detailed information on the AccelStepper.h library please visit AccelStepper Library: http://www.airspayce.com/mikem/arduino/AccelStepper/index.html. The program is divided into the following sections:

a Libraries: loading libraries to control motor and display

b Constants: defining constants for the program and assign pins of the Arduino

c setup: set pin modes, display values and motor speed

d Main Loop: actual controller program

e Functions: defining all function loops

Commentary can be found in the source code. Program should be flashed to an Arduino Nano v3. Wiring diagram and electronics information follow in B.1.

B Electronics

B.1 Polarisation stabilisation

In this section the hardware, the general setup and the alignment of the polariser device for the motorised $\lambda/2$ wave-plate polarisation stabilisation is explained. The whole device is an in-house construction.The device was built with the help of Dr. Anatoly Johnson (programming) and HTL Ing. Georg Holderied (electronics).

B.1.1 How polarization fluctuations are introduced in the experiment

Laser polarisation

The polarisation of the Toptica DL 100 diode laser system (DL) is, under normal circumstances, elliptical. It is turned into a linear polarization by the optical isolators before the output of the laser. There are additional optical isolators to prevent back reflection of laser light from the tapered amplifier (TA) into the DL and also block the laser light emitted by the TA to enter the DL. At the output of the tapered amplifier is also an optical isolator, hence the polarization is fixed and there is only one which can pass through them.

Fibre coupling

To guide the outgoing linear polarised beam of the TA into a PM-SMF (polarisation maintaining single-mode fibre), the TA out-coupler is used. Usually the alignment of the PM-SMF needs to be chosen very carefully because in the construction of the PM fibres stress applying parts are used forcing the light wave to follow a linear polarized path. Birefringence is created in the fibre by those parts which break its circular symmetry and therefore introduce two principal transmission axes. (For additional reading please visit following webpage: https://www.rp-photonics.com/polarization_maintaining_fibers.html)
To couple linearly polarised light into the fibre and make use of the advantage of a polarization maintaining fibre, it should be either coupled into the slow axes or the fast axes. The better the incident light is matched to one of the two axis the higher the polarization extinction ratio

(PER) and thus the polarization is maintained. Generally speaking the PER is calculated as follows:

$$\mathrm{PER} = 10 \log_{10} \frac{P_y}{P_x}, \tag{B.1}$$

where P_x is the optical power of the wanted polarization and P_y is the optical power of the unwanted polarization. Meaning $-30\,\mathrm{dB}$ compares to a ratio of 1000:1 and $-20\,\mathrm{dB}$ to a ratio of 100:1.

In the case of the fixed fibre coupler on the TA, the variation of the angle in which the fibre key, thus the polarization, is aligned to the incident polarization is very coarse and difficult to handle. This introduces already a polarisation mismatch. The high optical power of 1.2 W burns the fibre tip over time and light is leaking into the cladding of the fibre and hence introducing additional polarisation fluctuations.

B.1.2 Construction

The setup of the device consists of a $\lambda/2$ wave-plate mounted on a rotational mount (see Figure B.1.4a), a combination of a rotational mount with a Newport mirror stepper motor (bipolar) (see Figure B.1.4b). The rotational mount was modified by the mechanics workshop to turn the $\lambda/2$ wave-plate at a range of $\pm 6^\circ$ degree. Within this range the rotation of the polarisation outcoupled from the fibre is compensated. The internal setup of the controller box is a combination of the three parts: First, the photodiode readout, which converts the

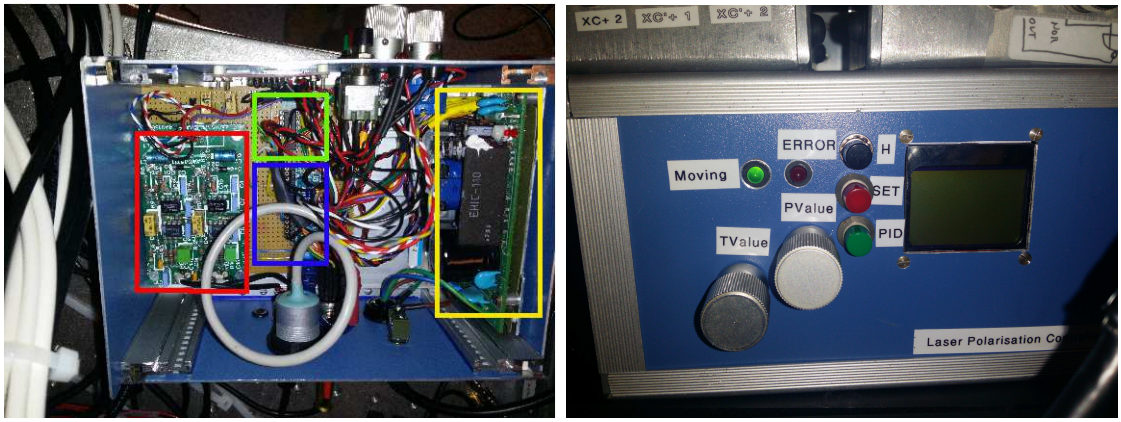

(a) (b)

Figure B.1.1: In the left figure the internal setup is shown and in the right figure the front plate of the polarisation device. (a) The red square is the photodiode readout pcb. The green square is the motor driver chip. The blue square the Arduino chip and the yellow square is the power supply unit. (b) 'H' stands for home. 'SET' for setup and 'PID' for active regulation. The red led indicates an error and the green led operation. 'TValue' stands for the maximum difference between the two photodiodes before the controller reacts and moves the polarisation and the PValue is the speed how fast the polarisation will be turned.

photodiode voltage in a readable voltage for the controller. Second, the motor driver chip with an external power supply to ensure that the stepper motor has enough power to turn the rotational mount. Third the Arduino chip to compare the input of the photodiodes, take the right actions and provide a readout at the Nokia display and a USB port to adjust and control the whole setup. In Figure B.1.1a, the internal setup is shown. Marked in red is the photodiode controller, the motor controller is marked in green, the arduino is marked in blue and the power supply is marked in yellow. Figure B.1.1b shows the front plate with the controls. 'H' stands for home. 'SET' for setup and 'PID' for active regulation. The red led indicates an error and the green led operation. 'TValue' stands for the maximum difference between the two photodiodes before the controller reacts and moves the polarisation and the PValue is the speed how fast the polarisation will be turned. A more detailed information of the control values and the program structure can be found in section A.8.

B.1.3 Photodiodes

The whole photodiode setup came from an old laser system and was built in house by Georg Holderied. This setup was implemented in the same configuration as it was found, except changing the length of the photodiode cable and adjusting the two potentiometer numbered 1 and 2 to limit the voltage send to the Arduino inputs, when the photodiodes saturate. More information on the photodiode pcb was not necessary and therefore not obtained. To get detailed information it is recommended to ask Georg Holderied for advice.

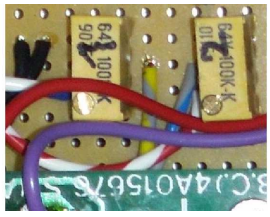

Figure B.1.2: Potentiometers 1 and 2

Motor controller, stepper motor and rotational mount

To address the NSA12 stepper motor, a motor controller is used. This controller consists, according to Figure B.1.3a, of one L293B microchip and 8x 1N4148 diodes, four for each motor. These diodes simple shield the motor against overload during switching on, off or rotation directions. In order to keep it easily understandable, the colour coding for the connection to the arduino and to the motor from the L293B was kept according to the NSA12 data sheet. To secure the motor from damaging itself, the negative pull-up circuit suggested in the data sheet was implemented and additionally after switching on the motor it will go to the home position by itself to aquire a zero position for its operations. Also the maximum step count is limited by the software and therefore the motor should not be able to run into the hardware stop build in.

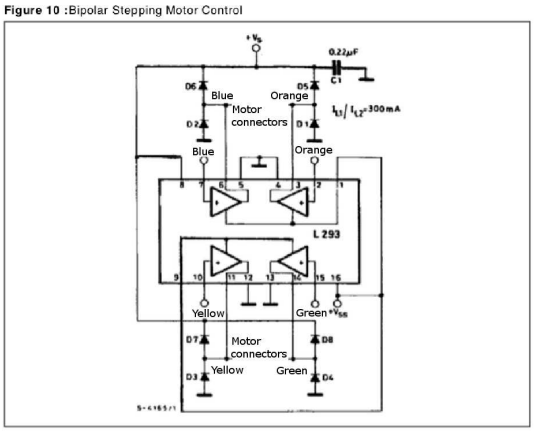

(a)

Wire Color	Signal	Wire Size
White	Homing Signal	28 AWG
Green	Phase A+	28 AWG
Red	+5 V	28 AWG
Orange	Phase B-	28 AWG
Blue	Phase B+	28 AWG
Yellow	Phase A-	28 AWG
Black	GND (0 V)	28 AWG
Brown	Not user	28 AWG

(b)

Figure B.1.3: Wiring plan for the L293B motor - driver to control the bipolar NSA12 stepper - motor from Newport and internal wiring of the steppermotor itself

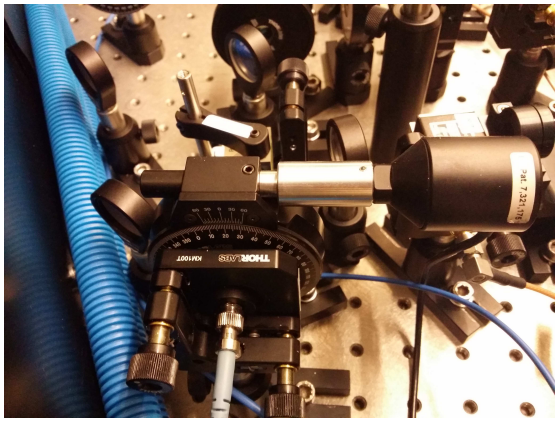

(a)

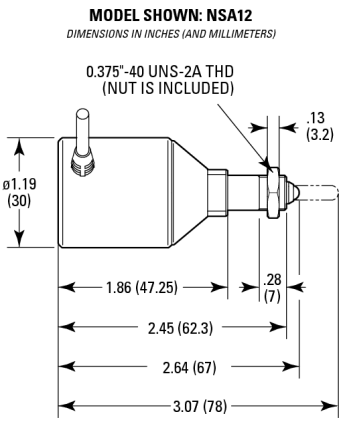

(b)

Figure B.1.4: In - house rotational mount for $\lambda/2$ wave - plate

Arduino and Nokia Display

The working brain of the polarisation device is a Arduino Nano v3 in combination with a Nokia display. In Figure B.1.5a, the pin layout of the Arduino is listed. The polariser device is wired as shown in the following tables.

Table B.1: Wiring table for Nokia 5110 Display

Arduino Pin	Nokia Display	Description
D2	GND	Ground
D3	RST	LCD Reset
D4	CE	LCD Chip Select
D5	D/C	Data Command Select
D6	DIN	Serial Data Out
D7	CLK	Serial Clock Out
D13	Light	Backlight Display
3V3	VCC	Power Supply

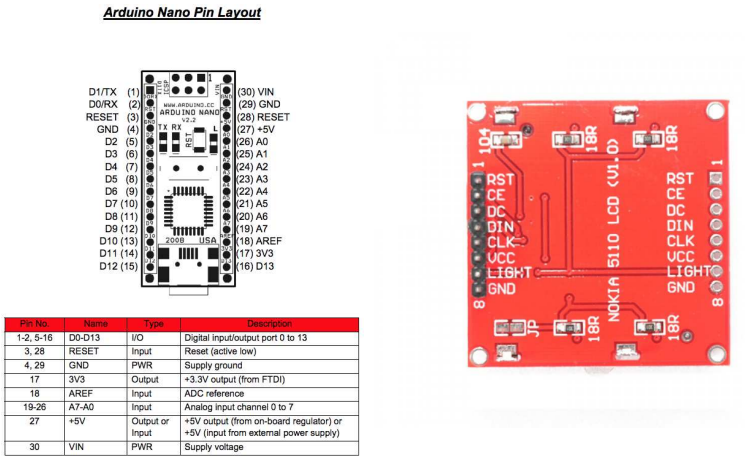

(a) (b)

Figure B.1.5: The left figure shows the pin layout of the Arduino Nano v3 and the right figure shows the pin layout of the Nokia display

B.1.4 Setup

To achieve the best control over the polarisation fluctuation of the setup, the $\lambda/2$ wave-plate is placed right after the fibre, which is directly connected to the BoosTA. The control beams are then decoupled directly after the first polarizing beam splitter cube. This is done by two beam samplers from Thorlabs. The two beams are directed to the photodiodes individually. Before the two beams enter the photodiodes, they pass through a linear polariser and a laser

Table B.2: Wiring table for LEDs, Potentiometer, Buttons, Motor

Arduino Pin	Description
GND	Ground
A0	PhotoDiode 1
A1	PhotoDiode 2
A2	Motor Moves LED
A3	Home Button
A4	PID Button
A5	SET Button
A6	TValue Pot
A7	PValue Pot
D2	Stepper Motor End Position Switch
D12	Error LED
D8	Motor Pin
D9	Motor Pin
D10	Motor Pin
D11	Motor Pin

bandpass filter from Thorlabs which filters almost every wavelength except 780 nm. This linewidth filter ensures that the photodiodes are not disturbed by any other light in the lab. Vigorous tests with laser pointer at other wavelengths and very bright flash lamps directed on the photodiodes were conducted and led to the conclusion that the system is stable enough for the daily lab use. It is more likely that the laser falls out of lock before wandering off in terms of polarisation and introduce power fluctuations.

B.1.5 Adjusting

Since both laser beams are not to be equally distributed from the beginning, the whole adjustment procedure is as follows:

1 loosen the silver screw on the rotational mount to make the $\lambda/2$ wave - plate turn freely

2 push the H button on the polarisation device and wait for the display to say: Motor in 0 Position

3 push the SET button and wait for the setup screen

4 measure with the power meter the input power of the YZ laser beam in front of the beam input coupler and adjust the power according to your needs with the $\lambda/2$ wave - plate

5 set PValue and TValue to 0 with the two potentiometers

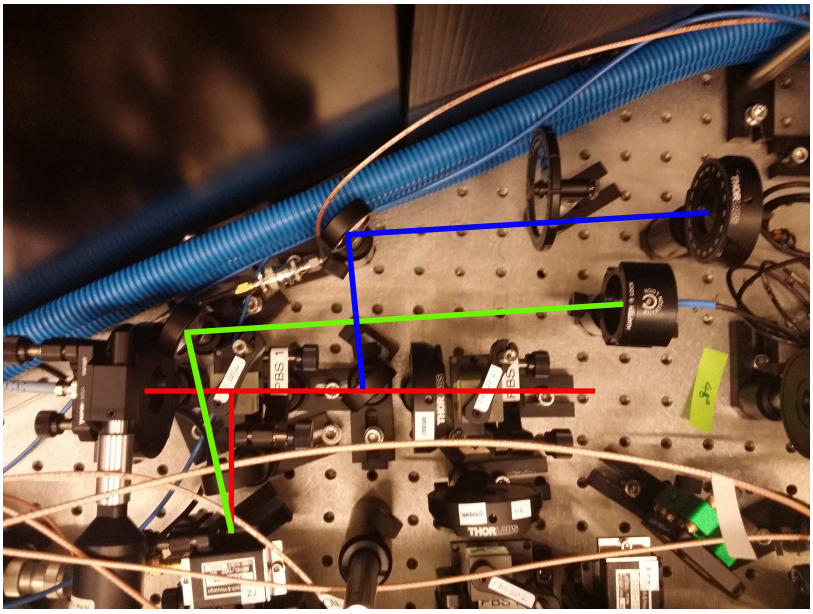

Figure B.1.6: Laser beam setup to operate the photodiodes. Colour code: Red - laser beam for experiment, Green - laser beam for PD1 and Blue - laser beam for PD2

6 turn the rotational mount of the photodiode (PD1 at the moment), which shows the power of the beam going to YZ, to a value between 100-500

7 tighten the silver screw on the rotational mount of the $\lambda/2$ wave - plate

8 turn the rotational mount of the photodiode (PD2 at the moment), which shows the power of the beam going to X, to a value that the PD1-PD2 on the display shows 0 (or very close like 1 to 5)

9 both photodiodes adjusted and PD1-PD2 on the display shows a value from 0 to ± 5 push the PID button

10 from experience: if the setup procedure is correctly done set the PValue to -2 and the TValue to 2

11 check if the motor is moving and the $\lambda/2$ wave - plate is turning and look at the display to check to which values the motor position is moving.

12 if everything is correct it should stabilize and the green led should blink when the motor is moving. well done polarisation is stable now

13 if the red led is on constantly then the motor has run into a final position and everything is stuck. Please start again from point 1

B.1.6 Troubleshooting

> ***Have you tried forcing an unexpected reboot? See the driver hooks a function by patching the system call table, so it's not safe to unload it unless another thread's about to jump in there and do its stuff, and you don't want to end up in the middle of invalid memory!***
>
> (Maurice Moss, IT Crowd)

in other words: *Have you tried turning it off and on again.*

B.2 Oven controller, laser shutters

Oven controllers were built by HTL Ing. Georg Holderied. Using pre-existing AC oven power supplies. At the back of each power supply, a BNC input was attached to a standard semiconducter relay. These trigger at a given input voltage between 3 V to 32 V. This allows the 5 V of the Arduino to turn the voltage output of the Variac on or off. An additional switch was connected to choose between manual and remote control of the power supplies. Laser shutters are simple 'SG90' servo motors with laser shielding material attached to their end. The servo controller is programmed to move to the 'close' position in case of power failure to ensure laser safety.

Bibliography

[1] Willitsch, S., Bell, M. T., Gingell, A. D., Procter, S. R. & Softley, T. P. *Phys. Rev. Lett.* **100**, 043203 (2008).

[2] Otto, R., Mikosch, J., Trippel, S., Weidemüller, M. & Wester, R. *Phys. Rev. Lett.* **101**, 063201 (2008).

[3] Allmendinger, P., Deiglmayr, J., Höveler, K., Schullian, O. & Merkt, F. *J. Chem. Phys* **145**, 244316 (2016).

[4] Hall, F. & Willitsch, S. *Phys. Rev. Lett.* **109**, 233202 (2012).

[5] Rellergert, W. G. *et al. Nature* **495**, 490 (2013).

[6] Puri, P. *et al. Science* **357**, 1370 (2017).

[7] Puri, P. *et al. Nat. Chem.* **11**, 615 (2019).

[8] Eberle, P. Ph.D. thesis, University of Basel (2018).

[9] Eberle, P., Dörfler, A. D., von Planta, C., Ravi, K. & Willitsch, S. *Chemphyschem* **17**, 3769–3775 (2016).

[10] Hall, F. Ph.D. thesis, University of Basel (2013).

[11] Henson, A. B., Gersten, S., Shagam, Y., Narevicius, J. & Narevicius, E. *Science* **338**, 234 (2012).

[12] Metcalf, H. J. & van der Straten, P. *Laser Cooling and Trapping* (Springer, New York, 1999).

[13] Shuman, E., Barry, J., Glenn, D. & DeMille, D. *Phys. Rev. Lett.* **103**, 223001 (2009).

[14] Kozyryev, I. *et al. Phys. Rev. Lett.* **118**, 173201 (2017).

[15] Bergeman, T., Erez, G. & Metcalf, H. J. *Phys. Rev. A* **35**, 1535 (1987).

[16] Grimm, R., Weidemüller, M. & Ovchinnikov, Y. B. Optical dipole traps for neutral atoms. In *Advances in Atomic, Molecular, and Optical Physics*, vol. 42, 95–170 (Elsevier, 2000).

[17] Raab, E. L., Prentiss, M., Cable, A., Chu, S. & Pritchard, D. E. *Phys. Rev. Lett.* **59**, 2631 (1987).

[18] Schmidt, J. *et al. Phys. Rev. X* **8**, 021028 (2018).

[19] Major, F. G., Gheorghe, V. N. & Werth, G. *Charged Particle Traps* (Springer, Berlin and Heidelberg, 2005).

[20] Paul, W., Osberghaus, O. & Fischer, E. (VS Verlag für Sozialwissenschaften, 1958).

[21] Willitsch, S. *Int. Rev. Phys. Chem.* **31**, 175–199 (2012).

[22] Willitsch, S. *Proc. Int. Sch. Phys. Enrico Fermi* **189**, 255 (2015).

[23] Willitsch, S. *Adv. Chem. Phys.* **162**, 307 (2017).

[24] Sias, C. & Köhl, M. *Quantum Gas Experiments*, 267 (World Scientific Publishing, Singapore, 2014).

[25] Härter, A. & Hecker Denschlag, J. *Contemp. Phys.* **55**, 33 (2014).

[26] Tomza, M. *et al. Rev. Mod. Phys.* **91**, 035001 (2019).

[27] Hall, F. H. J., Aymar, M., Bouloufa-Maafa, N., Dulieu, O. & Willitsch, S. *Phys. Rev. Lett.* **107**, 243202 (2011).

[28] Rellergert, W. G. *et al. Phys. Rev. Lett.* **107**, 243201 (2011).

[29] Schmid, S., Härter, A. & Hecker Denschlag, J. *Phys. Rev. Lett.* **105**, 133202 (2010).

[30] Hall, F. H. J., Aymar, M., Raoult, M., Dulieu, O. & Willitsch, S. *Mol. Phys.* **111**, 1683–1690 (2013).

[31] Joger, J. *et al. Phys. Rev. A* **96**, 030703 (2017).

[32] Zipkes, C., Palzer, S., Sias, C. & Köhl, M. *Nature* **464**, 388 (2010).

[33] Haze, S., Sasakawa, M., Saito, R., Nakai, R. & Mukaiyama, T. *Phys. Rev. Lett.* **120**, 043401 (2018).

[34] Krükow, A. *et al. Phys. Rev. Lett.* **116**, 193201 (2016).

[35] Sikorsky, T., Meir, Z., Ben-shlomi, R., Akerman, N. & Ozeri, R. *Nat. commun.* **9**, 920 (2018).

[36] Meir, Z. *et al. Phys. Rev. Lett.* **117**, 243401 (2016).

[37] Rouse, I. & Willitsch, S. *Phys. Rev. Lett.* **118**, 143401 (2017).

[38] da Silva jr., H., Raoult, M., Aymar, M. & Dulieu, O. *New J. Phys.* **17**, 045015 (2015).

[39] Tacconi, M., Gianturco, F. A. & Belyaev, A. K. *Phys. Chem. Chem. Phys.* **13**, 19156 (2011).

[40] Zhang, D. & Willitsch, S. In Dulieu, O. & Osterwalder, A. (eds.) *Cold Chemistry: Molecular Scattering and Reactivity Near Absolute Zero*, 496 (RSC Publishing, 2017).

[41] Gioumousis, G. & Stevenson, D. P. *J. Chem. Phys.* **29**, 294 (1958).

[42] Langevin, M. P. *Ann. Chim. Phys.* **5**, 245 (1905).

[43] Côté, R. & Dalgarno, A. *Phys. Rev. A* **62**, 012709 (2000).

[44] Gao, B. *Phys. Rev. A* **83**, 062712 (2011).

[45] Levine, R. D. *Molecular Reaction Dynamics* (Cambridge University Press, Cambridge, 2005).

[46] Jeziorski, B., Moszynski, R. & Szalewicz, K. *Chem. Rev.* **94**, 1887–1930 (1994).

[47] Krych, M., Skomorowski, W., Pawłowski, F., Moszynski, R. & Idziaszek, Z. *Phys. Rev. A* **83**, 032723 (2011).

[48] Sobelman, I. I. *Atomic Spectra and Radiative Transitions* (Springer, Berlin, 1979).

[49] Stone, A. *The Theory of Intermolecular Forces* (Oxford University Press, Oxford, 2013), 2. edition edn.

[50] Zare, R. N. *Angular Momentum* (John Wiley & Sons, New York, 1988).

[51] Smith, W. W., Makarov, O. P. & Lin, J. *J. Mod. Opt.* **52**, 2253 (2005).

[52] Grier, A. T., Cetina, M., Oručević, F. & Vuletić, V. *Phys. Rev. Lett.* **102**, 223201 (2009).

[53] Ravi, K., Lee, S., Sharma, A., Werth, G. & Rangwala, S. A. *Nat. Commun.* **3**, 1126 (2012).

[54] Sivarajah, I., Goodman, D. S., Wells, J. E., Narducci, F. A. & Smith, W. W. *Phys. Rev. A* **86**, 063419 (2012).

[55] Haze, S., Hata, S., Fujinaga, M. & Mukaiyama, T. *Phys. Rev. A* **87**, 052715 (2013).

[56] Deiglmayr, J., Göritz, A., Best, T., Weidemüller, M. & Wester, R. *Phys. Rev. A* **86**, 043438 (2012).

[57] Meir, Z. *et al. Phys. Rev. Lett.* **117**, 243401 (2016).

[58] Puri, P., Mills, M., West, E. P., Schneider, C. & Hudson, E. R. *RSI* **89**, 083112 (2018).

[59] Rouse, I. Ph.D. thesis, University of Basel (2018).

[60] Foot, C. F. *Atomic Physics* (Oxford University Press, Oxford, 2005).

[61] Steck, D. A. Rubidium 87 d line data revision 2.1.5. https://steck.us/alkalidata/ (2015).

[62] Shah, M. H. *et al. Phys. Rev. A* **75**, 053418 (2007).

[63] Maxwell, J. C. *Philos. Trans. R Soc. Lond.* **155**, 459–512 (1865).

[64] Shuman, E. S., Barry, J. F. & DeMille, D. *Nature* **467**, 820 (2010).

[65] Barry, J., McCarron, D., Norrgard, E., Steinecker, M. & DeMille, D. *Nature* **512**, 286–289 (2014).

[66] Hummon, M. T. *et al. Phys. Rev. Lett.* **110**, 143001 (2013).

[67] Truppe, S. *et al. Nat. Phys.* **13**, 1173–1176 (2017). 1703.00580.

[68] Anderegg, L. *et al. Nat. Phys.* **14**, 890–893 (2018). 1803.04571.

[69] Dehmelt, H. G. *Bull. Am. Phys. Soc.* **20**, 60 (1975).

[70] Haensch, T. & Schawlow, A. *Opt. Commun.* **13**, 68–69 (1975).

[71] Chu, S., Hollberg, L., Bjorkholm, J. E., Cable, A. & Ashkin, A. *Phys. Rev. Lett.* **55**, 48–51 (1985).

[72] Steane, A. & Foot, C. *EPL* **14**, 231 (1991).

[73] Anderson, M. H., Ensher, J. R., Matthews, M. R., Wieman, C. E. & Cornell, E. A. *Science* **269**, 198 (1995).

[74] Drewsen, M. & Brøner, A. *Phys. Rev. A* **62**, 045401 (2000).

[75] Friedburg, H. & Paul, W. *Naturwissenshaft* **38**, 159 (1951).

[76] Benewitz, H. & Paul, W. *Z. Physik* **139**, 489 (1954).

[77] Courant, E., Livingstone, M. & Snyder, H. *Phys. Rev.* **88**, 1190 (1952).

[78] Prestage, J. D., Dick, G. J. & Maleki, L. *J. Appl. Phys.* **66**, 1013 (1989).

[79] Paul, W., Reinhard, H. P. & von Zahn, U. *Z. Physik* **152**, 143–182 (1958).

[80] COMSOL Multiphysics version 3.5a and 4.3a, www.comsol.com.

[81] Gerlich, D. *Adv. Chem. Phys.* **82**, 1 (1992).

[82] Roth, B., Blythe, P. & Schiller, S. *Phys. Rev. A* **75**, 023402 (2007).

[83] Berkeland, D. J., Miller, J. D., Bergquist, J. C., Itano, W. M. & Wineland, D. J. *J. Appl. Phys.* **83**, 5025 (1998).

[84] Wineland, D. J., Bergquist, J. C., Itano, W. M., Bollinger, J. J. & Manney, C. H. *Phys. Rev. Lett.* **59**, 2935 (1987).

[85] Drewsen, M. *et al. AIP Conference Proceedings* **606**, 135 (2002).

[86] Drewsen, M. *et al. Int. J. Mass Spectrom.* **229**, 83 (2003).

[87] Pollock, E. L. & Hansen, J. P. *Phys. Rev. A* **8**, 3110 (1973).

[88] Schiffer, J. P. *Phys. Rev. Lett.* **88**, 205003 (2002).

[89] Drullinger, R. E., Wineland, D. J. & Bergquist, J. C. *Appl. Phys.* **22**, 365 (1980).

[90] Larson, D. J., Bergquist, J. C., Bollinger, J. J., Itano, W. M. & Wineland, D. J. *Phys. Rev. Lett.* **57**, 70–73 (1986).

[91] Hall, F. H. J. *et al. Mol. Phys.* **111**, 2020 (2013).

[92] Eberle, P. *et al. J. Phys. Conf. Ser.* **635**, 012012 (2015).

[93] Pradhan, S. & Jagatap, B. N. *Rev. Sci. Instrum.* **79**, 013101 (2008).

[94] Shah, M. H. *et al. Phys. Rev. A* **75**, 053418 (2007).

[95] Bradley, C. C., McClelland, J. J., Anderson, W. R. & Celotta, R. J. *Phys. Rev. A* **61**, 053407 (2000).

[96] Von Planta, C. Master's thesis, University of Basel (2015).

[97] Hairer, E., Lubich, C. & Wanner, G. *Geometric Numerical Integration: Structure-Preserving Algorithms for Ordinary Differential Equations; 2nd ed.* (Springer, Dordrecht, 2006).

[98] González-Martínez, M. L., Dulieu, O., Larrégaray, P. & Bonnet, L. *Phys. Rev. A* **90** (2014).

[99] López-Durán, D., Bodo, E. & Gianturco, F. A. *CPC* **179**, 821 – 838 (2008).

[100] Hauser, W. & Feshbach, H. *Phys. Rev.* **87**, 366–373 (1952).

[101] Miller, W. H. *The Journal of Chemical Physics* **52**, 543–551 (1970).

[102] Krems, R. V., Stwalley, W. C. & Friedrich, B. (eds.) *Cold Molecules: Theory, Experiment, Applications*. Boca Raton (CRC Press, 2009).

[103] Gianturco, F. A. *et al. PCCP* **21**, 8342–8351 (2019).

[104] Werner, H.-J. & Knowles, P. J. *J. Chem. Phys.* **82**, 5053 (1985).

[105] Leininger, T. *et al. Chemical Physics Letters* **255**, 274 – 280 (1996).

[106] Yurtsever, E. personal communication.

[107] Hall, W. D. & Zorn, J. C. *Phys. Rev. A* **10**, 1141–1144 (1974).

[108] González-Sánchez, L., Wester, R. & Gianturco, F. A. *Phys. Rev. A* **98**, 053423 (2018).

[109] Vera, M. H., Yurtsever, E., Wester, R. & Gianturco, F. A. *J. Chem. Phys* **148**, 184305 (2018).

[110] Hauser, D. *et al.* Rotational state-changing cold collisions of hydroxyl ions with helium. *Nat. Phys.* **11**, 467 (2015).

[111] Pirani, F., Maciel, G. S., Cappelletti, D. & Aquilanti, V. *Int. Rev. Phys. Chem.* **25**, 165 (2006).

[112] Dörfler, A. D. *et al. Nat. Commun.* **10**, 5429 (2019).

[113] Werner, H.-J. & Knowles, P. J. *J. Chem. Phys.* **89**, 5803 (1988).

[114] Thom H. Dunning, J. *J. Chem. Phys.* **90**, 1007 (1989).

[115] Lim, I. S., Schwerdtfeger, P., Metz, B. & Stoll, H. *J. Chem. Phys.* **122**, 104103 (2005).

[116] Tomza, M. *et al. Mol. Phys.* **111**, 1781 (2013).

[117] Ho, T.-S. & Rabitz, H. *J. Chem. Phys.* **104**, 2584 (1996).

[118] Unke, O. T. & Meuwly, M. *J. Chem. Inf. Model* **57**, 1923–1931 (2017).

[119] Johnson, B. R. *J. Chem. Phys.* **69**, 4678 (1978).

[120] Tomza, M., González-Férez, R., Koch, C. P. & Moszynski, R. *Phys. Rev. Lett.* **112**, 113201 (2014).

[121] Koner, D., Bemish, R. J. & Meuwly, M. *J. Chem. Phys.* **149**, 094305 (2018).

[122] Truhlar, D. G. & Muckerman, J. T. 505 (Springer US, 1979).

[123] Henriksen, N. E. & Hansen, F. Y. *Theories of Molecular Reaction Dynamics* (Oxford, 2011).

[124] Landau, L. D. *Z. Phys* **2**, 46 (1932).

[125] Zener, C. *Proc. R. Soc. London A* **137**, 696 (1932).

[126] Belyaev, A. K. & Lebedev, O. V. *Phys. Rev. A* **84**, 014701 (2011).

[127] Belyaev, A. K., Lasser, C. & Trigila, G. *J. Chem. Phys.* **140**, 224108 (2014).

[128] Stine, J. R. & Muckerman, J. T. *J. Chem. Phys.* **65**, 3975 (1976).

[129] Miller, W. H. & George, T. F. *J. Chem. Phys.* **56**, 5637 (1972).

[130] van der Kamp, A. B., Cosby, P. C. & van der Zande, W. J. *Chem. Phys.* **184**, 319 (1994).

[131] Krenn, C., Scherf, W., Khait, O., Musso, M. & Windholz, L. *Z. Physik D* **41**, 229–233 (1997).

[132] Green, S., Montgomery, J. A., Jr. & Thaddeus, P. *ApJ* **193**, L89–L91 (1974).

[133] Sastry, K., Helminger, P., Herbst, E. & Lucia, F. C. D. *Chem. Phys. Lett.* **84**, 286 – 287 (1981).

[134] van den Heuvel, F., Meerts, W. & Dymanus, A. *Chem. Phys. Lett.* **92**, 215 – 218 (1982).

[135] Gianturco, F., Kumar, S. & Schneider, F. *Chem. Phys.* **211**, 33 – 46 (1996).

[136] Gentry, W. R., Gislason, E. A., Lee, Y.-T., Mahan, B. H. & Tsao, C.-W. *Discuss. Faraday Soc.* **44**, 137–145 (1967).

[137] Tanarro, I. *et al. J. Phys. Chem. A* **111**, 9003–9012 (2007).

[138] Itano, W. M. *J. Res. Natl. Inst. Stand. Technol.* **105**, 829 (2000).

[139] Angel, J. R. P., Sandars, P. G. H. & Woodgate, G. K. *J. Chem. Phys.* **47**, 1552–1553 (1967).

[140] Eberle, P. Master's thesis, University of Basel (2012).